Petra Neubauer-Guenther

# Rovibrational Spectroscopy on Linear $C_7$ and $C_8$ in a Supersonic Jet Expansion

PHYSIK

# Rovibrational Spectroscopy on Linear $C_7$ and $C_8$ in a Supersonic Jet Expansion

Inaugural-Dissertation
zur
Erlangung des Doktorgrades
der Mathematisch-Naturwissenschaftlichen Fakultät
der Universität zu Köln

vorgelegt von

Petra Neubauer-Guenther

aus Köln

Köln 2006

Berichterstatter: Priv. Doz. Dr. T.F. Giesen
Prof. Dr. J. Jolie

Tag der mündlichen Prüfung: 09. Februar 2007

*Für Mum*

Some who have read the book, or at any rate have reviewed it,
have found it boring, absurd, or contemptible,
and I have no cause to complain,
since I have similar opinions of their works...

*J. R. R. Tolkien*

# Abstract

In the scope of this work, high resolution rovibrational measurements have been performed on the linear carbon chains $C_7$ and $C_8$. The spectra have been recorded with the Cologne Carbon Cluster Experiment, which combines a high resolution tunable IR diode laser spectrometer with a UV laser ablation source. It was a main task of this work to modify the existing experimental setup aiming for a significant increase of the signal-to-noise ratio. The accomplished rearrangements enabled the investigation of weaker absorption signals like hot band transitions.

More than 70 rovibrational transitions occuring in the spectral region from 2066.8 to 2069.0 $cm^{-1}$ have been observed and subsequently assigned to the $\nu_5$ antisymmetric stretching fundamental of linear $C_8$. From a least squares fit, a band origin close to 2067.89 $cm^{-1}$ and a rotational constant for the vibrational ground-state of approximately 0.0208 $cm^{-1}$ have been derived. The analysis of the measured triplet splitting yields evidence for an uncoupling of the spin resulting in a transition between Hund's coupling case (a) and case (b) scheme.

For $C_7$, infrared measurements of the $\nu_4$ fundamental antisymmetric stretching mode and associated hot bands have been recorded in the frequency range from 2135.0 to 2141.0 $cm^{-1}$. Spectra of the $\nu_4$ fundamental, as well as the $\nu_4 + \nu_{11} - \nu_{11}$, $\nu_4 + \nu_8 - \nu_8$, and $\nu_4 + 2\nu_{11} - 2\nu_{11}$, $\ell = 2$ bands have been analysed and are compared to hitherto existing experimental results [35, 36] and high-level *ab initio* calculations [9]. For the two energetically low-lying bending modes, $\nu_8$ and $\nu_{11}$, the obtained rotational constants differ only by 0.2 % from the ground state value, $B_0 = 0.0306259(29)$ $cm^{-1}$, in good agreement with recent calculations. From the hot band analysis, the $\ell$-type doubling constants $q$ and experimental values for the band origins of the $\nu_8$ and $\nu_{11}$ fundamentals have been derived for the first time, namely $\nu_{11} = 54(11)$ $cm^{-1}$ and $\nu_8 = 81(23)$ $cm^{-1}$. The results presented in this work give experimental evidence for the non-floppiness of $C_7$ and confirm the theoretical predictions of a rather regular chain molecule, similar to the cases of $C_4$, $C_5$, and $C_9$.

# Kurzzusammenfassung

Im Rahmen der vorliegenden Arbeit wurden hochauflösende Rotations-Vibrations-Messungen an den linearen Kohlenstoffketten $C_7$ und $C_8$ durchgeführt. Die Spektren wurden mit dem Kölner Kohlenstoffcluster-Experiment aufgenommen, das ein hochauflösendes, durchstimmbares IR-Diodenlaserspektrometer mit einer UV-Laserverdampfungsquelle zur Clustererzeugung kombiniert. Ein wesentlicher Teil dieser Arbeit bestand im Umbau des bestehenden experimentellen Aufbaus mit dem Ziel, das Signal-zu-Rausch-Verhältnis (SNR) deutlich zu verbessern. Die vorgenommenen Änderungen ermöglichten die Untersuchung von Übergängen heißer Banden mit schwachen Absorptionssignalen.

Im Spektralbereich zwischen 2066,8 und 2069,0 $cm^{-1}$ konnten mehr als 70 Rotations-Vibrations-Übergänge beobachtet werden, die im Folgenden der $\nu_5$ antisymmetrischen Streckschwingung von linearem $C_8$ zugeordnet wurden. Die Auswertung der Daten ergab einen Bandenursprung nahe 2067,89 $cm^{-1}$ sowie eine Rotationskonstante des Vibrationsgrundzustands von ungefähr 0,0208 $cm^{-1}$. Die Analyse der gemessenen Triplett-Aufspaltung gibt Grund zu der Annahme, dass es unter dem Einfluss der Rotation zum Umkoppeln des Elektronenspins kommt, was einem Übergang zwischen den beiden idealisierten Kopplungsmodellen Hund'scher Fall (a) und (b) entspricht.

Für lineares $C_7$ konnten hochauflösende Infrarotmessungen der $\nu_4$ antisymmetrischen Streckschwingung sowie zugehöriger heißer Banden im Frequenzbereich zwischen 2135,0 und 2141,0 $cm^{-1}$ aufgenommen werden. Die Spektren der $\nu_4$ Fundamentalen sowie der $\nu_4 + \nu_{11} - \nu_{11}$, $\nu_4 + \nu_8 - \nu_8$ und $\nu_4 + 2\nu_{11} - 2\nu_{11}$, $\ell = 2$ Banden wurden analysiert und mit den bisherigen Messungen [35, 36] und den *ab initio* Berechnungen [9] verglichen. Für die zwei energetisch tiefliegenden Knickschwingungen, $\nu_8$ und $\nu_{11}$, wurden in der vorliegenden Untersuchung Rotationskonstanten bestimmt, die um nur 0,2 % von $B_0 = 0{,}0306259(29)$ $cm^{-1}$, dem Wert für den Grundzustand, abweichen. Diese Werte stimmen sehr gut mit den neuesten Vorhersagen überein. Aus der Analyse der heißen Banden konnten die $\ell$-Typ Verdopplungskonstanten $q$ gewonnen und mit deren Hilfe die Bandenursprünge der fundamentalen Biegeschwingungen abgeleitet werden. Mit $\nu_{11} = 54(11)$ $cm^{-1}$ und $\nu_8 = 81(23)$ $cm^{-1}$ liegen nun erstmals experimentelle Abschätzungen für diese Werte vor. Die im Rahmen dieser Arbeit vorgestellten Ergebnisse bestätigen eindeutig die *ab initio* Rechnungen, nach denen es sich bei linearem $C_7$ um ein eher steifes Kettenmolekül mit Biegeschwingungen von kleiner Amplitude handelt. Damit zeigt $C_7$ das gleiche Verhalten wie die verwandten Kettenmoleküle $C_4$, $C_5$ und $C_9$.

# Zusammenfassung

Kohlenstoff ist nach Wasserstoff, Helium und Sauerstoff das vierthäufigste Element im Universum. Mehr als 70 % der Moleküle, die im interstellaren Medium gefunden wurden, bestehen aus mindestens einem Kohlenstoffatom. Diese Dominanz der Kohlenstoffchemie lässt sich in erster Linie durch die Strukturvielfalt in Kohlenstoffverbindungen erklären. Gerade dieser Bindungsreichtum macht kohlenstoffhaltige Moleküle so interessant für die Grundlagenforschung. Im Rahmen dieser Arbeit wurden daher reine Kohlenstoffketten mit Mitteln der hochauflösenden Laborspektroskopie untersucht.

Die Untersuchung reiner Kohlenstoffketten erfuhr nach der Entdeckung des $C_{60}$ Moleküls zu Beginn der 80er Jahre [54] besondere Aufmerksamkeit. Bis zur Klärung der käfigartigen Struktur des so genannten Buckminster-Fullerens, das wegen seiner Struktur aus Fünf- und Sechsecken zu Recht auch als “Fußballmolekül” bezeichnet wird, waren nur die stabilen Kohlenstoffkonfigurationen Graphit und Diamant bekannt. Die Frage, wie sich eine so komplexe Struktur herausbilden konnte, ist seitdem Gegenstand sowohl theoretischer als auch experimenteller Untersuchungen [91, 98]. Die linearen Kettenmoleküle konnten als wichtiger Baustein auf dem Weg zu den Fullerenstrukturen ausgemacht werden, da sich komplexere Gebilde aus ihnen entwickeln können. Allerdings ergeben sich bei den vermeintlich einfacheren Kettenmolekülen bereits eine Vielzahl von Fragen, die sich nur durch eine stetige Verbesserung von theoretischen Modellen anhand von experimentellen Untersuchungen beantworten lassen.

In der vorliegenden Arbeit wurde zwei dieser Fragen nachgegangen: der Biegsamkeit der Ketten sowie dem Einfluss eines elektronischen Spins auf die Spektren dieser Ketten.

Informationen über die Struktur und einige der Eigenschaften von Molekülen kann man aus rotationsaufgelösten Absorptionsspektren der Moleküle in der Gasphase gewinnen. Werden Moleküle elektromagnetischer Strahlung ausgesetzt, so kann die Energie der Strahlung auf das Molekül übertragen werden und es zum Schwingen anregen. Gleichzeitig können die Moleküle dabei in Rotation versetzt werden. Da die benötigten Energien molekülspezifisch sind, identifizieren die resultierenden Absorptionsspektren das verursachende Molekül.

Im Fall der Kohlenstoffketten ist man auf antisymmetrische Streckschwingungen

im Infraroten oder auf Knick- bzw. Biegeschwingungen im Ferninfrarot-Bereich angewiesen. Kombinationen aus beiden Schwingungstypen sind möglich und ebenfalls im Infraroten zu beobachten, daher können auch aus Infrarotmessungen Informationen über das Biegeverhalten der Kette abgeleitet werden. Im Verlauf dieser Arbeit wurde eine Fundamentalbande von linearem $C_8$ untersucht. Weiterhin wurden Messungen an so genannten “heißen” Banden von linearem $C_7$ durchgeführt, bei denen die $C_7$-Ketten aus einer angeregten Knickschwingung in eine zusätzliche antisymmetrische Streckschwingung angeregt werden.

Die Messungen wurden mit dem “Cologne Carbon Cluster Experiment”, dem Kölner Kohlenstoffcluster-Experiment durchgeführt. Ein Gas aus Kohlenstoffmolekülen wird dabei in einer Laserverdampfungsquelle erzeugt und anschließend durch eine adiabatische Expansion in einen kalten Molekularstrahl überführt. Rotations-Vibrations-Spektren der kalten Kohlenstoffcluster können mit Hilfe von durchstimmbaren Infrarot-Diodenlasern aufgenommen werden. Um die Nachweisempfindlichkeit zu erhöhen, wird der Infrarotstrahl mittels einer Vielfachreflexionsoptik nach dem Herriott-Prinzip mehrfach durch den Molekularstrahl geführt.

Da speziell für heiße Banden von Kohlenstoffketten schwache Signale zu erwarten sind, bestand ein wesentlicher Teil dieser Arbeit in einem Umbau des bestehenden experimentellen Aufbaus mit dem Ziel, das Signal-zu-Rausch-Verhältnis (SNR) deutlich zu verbessern. Zu den durchgeführten Maßnahmen gehörten die Gewährleistung mechanischer Stabilität und die Verbesserung der Effizienz der Verdampfungsquelle. Außerdem konnten stickstoffgekühlte Laserdioden als Strahlungsquellen implementiert werden. Insgesamt wurde eine Verbesserung des SNR um etwa eine Größenordnung gegenüber dem ursprünglichen System erzielt.

Im Spektralbereich zwischen 2066,8 und 2069,0 $cm^{-1}$ konnten mehr als 70 Rotations-Vibrations-Übergänge beobachtet werden, die der $\nu_5$ antisymmetrischen Streckschwingung von linearem $C_8$ zugeordnet werden konnten. Die Auswertung der Messungen ergab einen Bandenursprung nahe 2067,89 $cm^{-1}$, für die Rotationskonstante des Vibrationsgrundzustands ergab sich ein Wert von ungefähr 0,0208 $cm^{-1}$. Der höchste Rotations-Übergang wurde im R-Zweig mit $N = 27$ gemessen. Durch ungepaarte Elektronen an den beiden Kettenenden weist lineares $C_8$ einen resultierenden Spin auf, der sich im Absorptionsspektrum durch eine charakteristische Triplett-Aufspaltung bemerkbar macht. Die Analyse der Aufspaltung gibt Grund zu der Annahme, dass es unter dem Einfluss der Rotation zum Umkoppeln des Elektronenspins kommt, was einem Übergang zwischen den beiden idealisierten Kopplungsmodellen Hund’scher Fall (a) und (b) entspricht.

Für lineares $C_7$ konnten hochaufgelöste Infrarotspektren der $\nu_4$ antisymmetrischen Streckschwingung sowie zugehöriger heißer Banden im Frequenzbereich zwischen 2135,0 und 2141,0 $cm^{-1}$ aufgenommen werden. In diesem Bereich wurden 34 Linien der $\nu_4$ Fundamentalen nachgemessen. Zusätzlich konnten 7 neue Linien im R-Zweig mit $J = 50$ - 62 gemessen werden. Der heißen Bande $\nu_4 + \nu_{11} - \nu_{11}$ konnten 52 Linien zugeordnet werden. Weitere 57 Linien wurden als Übergänge der Bande $\nu_4 + 2\nu_{11} - 2\nu_{11}$, $\ell = 2$ identifiziert. Erstmals konnte auch die Bande $\nu_4 + \nu_8 - \nu_8$ beobachtet werden, der 49 Linien zugeordnet wur-

den. Die Ergebnisse wurden mit den neuesten *ab initio* Berechnungen [9] und mit bisherigen Messungen [35, 36] verglichen. Für die zwei energetisch tiefliegenden Knickschwingungen, $\nu_8$ und $\nu_{11}$, wurden in der vorliegenden Untersuchung Rotationskonstanten bestimmt, die um nur 0,2 % von $B_0 = 0{,}0306259(29)$ cm$^{-1}$, dem Wert für den Grundzustand, abweichen. Diese Werte stimmen sehr gut mit den berechneten Vorhersagen [9] überein. Die aus der Analyse der heißen Banden gewonnenen $\ell$-Typ Verdopplungskonstanten $q$ dienten zur Bestimmung der Bandenursprünge der fundamentalen Biegeschwingungen. Mit den ermittelten $\nu_{11} = 54(11)$ cm$^{-1}$ und $\nu_8 = 81(23)$ cm$^{-1}$ liegen nun erstmals experimentelle Abschätzungen für diese Werte vor. Die im Rahmen dieser Arbeit vorgestellten Ergebnisse bestätigen eindeutig die *ab initio* Rechnungen, nach denen es sich bei linearem $C_7$ um ein eher steifes Kettenmolekül mit Biegeschwingungen von kleiner Amplitude handelt. Damit zeigt $C_7$ das gleiche Verhalten wie die verwandten Kettenmoleküle $C_4$, $C_5$ und $C_9$.

# Contents

**Introduction** **1**

**On Carbon Clusters** **7**

2.1 Structures of Carbon Clusters . . . . . 7

2.1.1 Small Carbon Clusters . . . . . 8

2.1.2 Linear Chains . . . . . 10

2.2 Analysing Infrared Spectra of Linear Carbon Chains . . . . . 15

2.2.1 Odd-numbered Carbon Chains . . . . . 18

2.2.2 Even-numbered Carbon Chains . . . . . 20

**Experimental Setup** **29**

3.1 Cluster Sources . . . . . 29

3.1.1 The Laser Ablation Source . . . . . 30

3.2 The Cologne Carbon Cluster Experiment . . . . . 36

3.2.1 The Infrared Laser . . . . . 37

3.2.2 The Multipass Cell . . . . . 37

3.2.3 The InSb Detector . . . . . 40

3.3 Measuring Mode . . . . . 40

3.4 Calibration . . . . . 42

3.5 Sensitivity Considerations . . . . . 42

**Measurements on Linear $C_8$ – A Case of Spin Uncoupling** **45**

4.1 Infrared Spectra of linear $C_8$ . . . . . 46

4.2 Analysis . . . . . 47

4.3 Discussion . . . . . 54

4.3.1 Coupling mechanisms . . . . . 56

**Measurements on Linear $C_7$ – Floppy or not?** **61**

5.1 IR Spectra . . . . . 61

5.2 The $\nu_4$ fundamental . . . . . 62

5.3 Hot bands . . . . . 63

5.3.1 The $\nu_4 + \nu_{11} - \nu_{11}$, $\ell = 1$ hot band . . . . . 65

5.3.2 The $\nu_4 + \nu_8 - \nu_8$, $\ell = 1$ hot band . . . . . 69

5.3.3 The $\nu_4 + 2\nu_{11} - 2\nu_{11}$, $\ell = 2$ hot band . . . . . 69

5.4 Discussion . . . . . 71

5.5 Summary . . . . . 75

**Appendix A** **77**

**Bibliography** **81**

# List of Figures


2.1 Possible configurations for clusters of different sizes . . . . . 8
2.2 Calculated equilibrium structures for small carbon clusters . . . . . 9
2.3 Highest occupied molecular orbitals for $C_3$ and $C_4$ . . . . . 11
2.4 Calculated potentials for the lowest bendings of odd-numbered carbon chains [12] . . . . . 14
2.5 Energy level scheme for odd-numbered carbon chains . . . . . 18
2.6 Energy level scheme including hot band transitions . . . . . 20
2.7 Origin of the staggered line pattern for hot band transitions of odd-numbered carbon chains . . . . . 21
2.8 Coupling schemes for Hund's case (a) and (b) . . . . . 22
2.9 Energy level diagrams for Hund's cases (a) and (b) after [85] . . . . 24
2.10 Energy level scheme for even-numbered carbon chains within inverted Hund's case (a) limit . . . . . 27

3.1 Design of the laser ablation source . . . . . 31
3.2 Scheme of the laser ablation . . . . . 32
3.3 Side view of the cluster jet . . . . . 32
3.4 Top view of the cluster jet . . . . . 33
3.5 Velocity components after a slit expansion . . . . . 34
3.6 The Cologne Carbon Cluster Experiment . . . . . 36
3.7 Optical path within the vacuum chamber . . . . . 38
3.8 Pattern of reflexion spots . . . . . 39
3.9 Sensitivity of InSb detectors . . . . . 40
3.10 Timing scheme to illustrate the measuring mode . . . . . 41

3.11 Comparison between old and new system . . . . . 43

4.1 Absolute values of $\lambda$ for different carbon chain molcules against the number of $\pi$-electrons. . . . . 46
4.2 Measured spectrum of the $\nu_5$ band of $C_8$. . . . . 47
4.3 Loomis-Wood-Plot for Fit 1. . . . . 48
4.4 Loomis-Wood-Plot for Fit 2. . . . . 49
4.5 Ground state combination differences for Fit 1. . . . . 50
4.6 Upper state combination differences for Fit 1. . . . . 51
4.7 Ground state combination differences for Fit 2. . . . . 52
4.8 Upper state combination differences for Fit 2. . . . . 53
4.9 The $\nu_5$ band of $C_8$: comparison between measured and calculated spectrum. . . . . 57

5.1 Spectrum of the $\nu_4$ fundamental of $C_7$ and associated hotbands . . 62
5.2 Detail of the spectrum of $C_7$ . . . . . 66
5.3 Head of the *R*-branch of the $\nu_4 + \nu_{11} - \nu_{11}$ band . . . . . 68

# List of Tables


2.1 Infrared-active vibrational transitions of linear carbon clusters measured in isolated rare gas matrices and rotationally resolved in the gas phase. . . . . 12

2.2 Measured infrared hot bands of linear carbon chains . . . . . 13

3.1 Production conditions for $C_7$ and $C_8$ . . . . . 35

3.2 Comparison of production conditions with different types of vaporisation lasers. . . . . 35

3.3 Parameters for the Herriott cell . . . . . 39

3.4 Parameters to derive the minimum number of $C_7$ and $C_8$ cluster molecules necessary for detection . . . . . 44

4.1 Molecular constants for the $\nu_5$ antisymmetric stretching fundamental of $C_8$. . . . . 55

4.2 Reference values for the spin-spin coupling constant $\lambda$ for $C_n$, $C_nO$, and $SiC_n$. . . . . 58

4.3 Observed line positions of $C_8$ in the *P*-branch of the $\nu_5$ band in $cm^{-1}$ assigned according to Fit 1. Residuals refering to the fit without centrifugal distortion constants. . . . . 59

4.4 Observed line positions of $C_8$ in the *R*-branch of the $\nu_5$ band in $cm^{-1}$ assigned according to Fit 1. Residuals refering to the fit without centrifugal distortion constants. . . . . 60

5.1 Observed frequencies for the $\nu_4$ antisymmetric stretching fundamental of $C_7$ . . . . . 64

5.2 Molecular constants for the $\nu_4$ antisymmetric stretching fundamental of $C_7$ . . . . . 65

5.3 Observed frequencies for the $\nu_4 + \nu_{11} - \nu_{11}$ hot band of $C_7$ . . . . . 67

5.4 Molecular constants for the $\nu_4 + \nu_{11} - \nu_{11}$ hot band of $C_7$ . . . . . 68
5.5 Observed frequencies for the $\nu_4 + \nu_8 - \nu_8$ hot band of $C_7$ . . . . . 70
5.6 Molecular constants for the $\nu_4 + \nu_8 - \nu_8$ hot band of $C_7$ . . . . . 71
5.7 Observed frequencies for the $\nu_4 + 2\nu_{11} - 2\nu_{11}$ hot band of $C_7$ . . . 72
5.8 Molecular parameters for the $\nu_4 + 2\nu_{11} - 2\nu_{11}$, $\ell = 2$ hot band of $C_7$ 73
5.9 Observed band shifts for hot bands with two quanta in the bend. . 73

# 1

# Introduction

All that is currently known about matter in space, the origin and evolution of stars, or the dynamics of galaxies, has been derived from astronomical observations of absorption or emission of electromagnetic radiation. From these observations, we know that matter is not distributed homogeneously across the sky but occurs rather concentrated in distinct areas. Astronomers distinguish between extended, cloud-like and smaller, point-like structures. So-called molecular clouds belong to the first category. The more point-like structures are directly linked to stars, like hot cores, circumstellar envelopes or planetary nebulae.

Molecular clouds are characterised by typical temperatures in the range of 10 to 120 K and densities between $10^1$ and $10^4$ $cm^{-3}$. Within these scales, clouds with low densities but rather high temperatures are denoted ‘diffuse clouds‘, while the ‘dense clouds‘ are quite cold. The temperatures found in hot cores or circumstellar shells are significantly higher and of the order of hundreds of K [50].

The question arises how such detailed information, especially on physical parameters, can be gained by means of remote sensing with telescopes. Matter in space, primarily gaseous molecules, interact with electromagnetic radiation via rotational or vibrational motions or electronic transitions within the molecules. In general, radiation of low energy is sufficient to excite rotations of molecules, while vibrations and electronic transitions require higher energies. Roughly spoken, rotational transitions correspond to the microwave range of the electromagnetic spectrum ($\sim$ 0.3 - 300 GHz), vibrations to the infrared domain ($\sim$ 10 - 13000 $cm^{-1}$), and electronic transitions to the optical regime ($\sim$ 380 - 780 nm). In most cases, theses interactions occur in combination: if the absorbed energy is high enough to excite a vibrational mode of a molecule, the energy is by far sufficient to put it into rotation simultaneously. The absorbed or emitted frequencies are typical for a specific molecule, representing a kind of fingerprint, since all processes of interaction are quantised. Knowing the transition frequencies of molecules, astronomers are able to gain information on the composition of interstellar clouds or circumstellar shells. Furthermore, temperatures or densities can be derived from observations, because different transitions require different environmental conditions in astronomical sources.

Molecular spectroscopy has an important influence on the field of astronomy and astrophysics, because the knowledge of a molecule's accurate transition frequencies is crucial for its detection in interstellar or stellar sources. Thus, investigations on molecules in the laboratory support astronomers to detect these species in space. Models describing the astrophysics (the formation of stars and the cycle of matter) and the astrochemistry (the reaction pathways of molecules) are evolved with respect to the observations. To improve such models, a close cooperation between astronomers and spectroscopists is indispensable. In the laboratory, much effort is spent on the synthesis of new molecules with prospect of a possible interstellar detection. Further, more transitions of molecules already detected in the interstellar medium may also contribute to perfecting the model. Rotational transitions in different vibrational modes for example can be used to study excitation temperatures in miscellaneous sources.

After hydrogen, helium, and oxygen, carbon was found to be the fourth most abundant element in space, but a look at the list of interstellar detected molecules reveals that more than 70 % of all species identified in space so far are carbon-bearing molecules [15]. The reason might be the extreme versatility of the carbon bond allowing for the building of chains, rings, and even cage-like structures. Thus, carbon-containing molecules are commonly believed to play a dominant role in interstellar chemistry.

Even some pure carbon molecules have been identified in space. The sources are quite diverse ranging from comets and stellar objects to diffuse interstellar clouds. Up to now, only linear species have been found. Since bare carbon chains are non-polar and thereby showing no permanent electronic dipole moment, they display no pure rotational spectrum. Room for their detection in space is therefore restrained to rovibrational (mid- to far-infrared) or rovibronic (optical) transitions.

The first evidence for $C_3$ in stars was found in 1953, when P. Swings *et al.* noticed a band similar to the well-known $\lambda$ 4050 band in the spectra of three stars [84]. In 1975 both $C_2$ and $C_3$ have been detected in the circumstellar shell of post-carbon star CRL 2688 via their optical spectra [16]. More than ten years later, the first infrared detection of pure carbon chains was achieved in the circumstellar envelope of another carbon star, IRC+10216. P.F. Bernath *et al.* identified the two clusters $C_3$ and $C_5$ through two of their antisymmetric stretching modes in 1988 and 1989 [4, 42]. $C_3$ was also found in the optical spectrum of diffuse interstellar clouds [58]. The interstellar abundance of $C_3$ was confirmed by the optical detection in translucent clouds [81] and towards '$\zeta$ type' reddened stars [23]. The interstellar abundance of $C_3$ is quite important since carbon clusters are possible carriers of the 'diffuse interstellar bands' (DIBs) [17]. For the sake of completeness, the tentative astrophysical detections of $C_4$ and $C_6$ in ISO spectra are to be mentioned here [14, 28], although they are still not confirmed and appear to be arguable.

The above mentioned sources exhibit rather high temperatures, otherwise the detection of carbon chains by means of their infrared and optical spectra would have been impossible. Nevertheless, some models predict pure carbon chains to occur in significant amounts also in colder regions (e.g. [7]). To probe cold

sources, astronomers rely on the bending vibrational modes of the pure carbon chains occuring in the far-infrared (FIR) or THz-domain. $C_3$ was found through its bending vibration in the FIR towards Sgr B2 and IRC+10216 [13, 27]. So far, no other detection of a bare carbon chain in the FIR has been reported.

Apart from the mere astrophysical interest, carbon chains have drawn the attention of many spectroscopists regarding their part in the formation of larger carbon molecules. With the advent of new production methods in the early 80's, mass spectroscopic studies of vaporised carbon skyrocketed, particularly after significant amounts of molecules in the size range of 40 up to 120 atoms have been revealed (e.g. [80]). The molecule consisting of 60 carbon atoms soon turned out to be exceptional. Two stable modifications of carbon, graphite and diamond, were known, when in 1985, H.W. Kroto, R.F. Curl, R.E. Smalley *et al.* suggested a kind of spheroidal geometry for the $C_{60}$ molecule to explain its remarkable stability [54]. Due to its unusual structure resembling a football, the molecule was thus termed 'Buckminster fullerene'[1]. This discovery triggered many experimental and theoretical investigations on the so-called carbon clusters. The enormous variety of cluster structures as well as the possible formation mechanisms disclosed a whole new field of research. Calculated structures range from linear chains to cyclic and three dimensional configurations depending on the number of carbon atoms (e.g. [75, 79]). Besides the theoretical approach, efforts have been and are still made to determine the structure and properties of carbon clusters by means of spectroscopy [91, 98]. Information on the actual structure can be derived from the following experiments:

- anion photoelectron spectroscopy (e.g. [2, 33, 99, 102])
- electron-spin-resonance (ESR) studies (e.g. [31, 92])
- ion mobility measurements (e.g. [30, 94])
- Coulomb explosion imaging (CEI) method (e.g. [38, 86])
- spectroscopy of cold rare gas matrices (e.g. [19, 87, 95, 96])
- rotationally resolved gas phase spectroscopy of infrared active vibrational modes (e.g. [25, 60, 64])

The first two techniques aim for the electronic properties of the different isomers resulting in indirect evidence for linear or cyclic structures. All methods are described briefly in the following.

In anion photodetachment experiments, the kinetic energies of detached electrons are measured for mass selected anions permitting conclusions on internal energies and electron affinities. The lower the kinetic energy of an electron, the higher is the internal energy of the corresponding electronic state of the neutral.

[1] Named after the engineer Richard Buckminster Fuller, whose Geodesic Domes bear a high resemblance to the fullerene structure.

Sharp peaks in the photoelectron spectra are associated with linear isomers while broad features are interpreted as tracks of cyclic structures [2].

Electron-spin-resonance is based on the Zeeman effect. Exposed to a magnetic field the degeneracy of states is lifted within a molecule with a magnetic moment. The energy difference between the splitted levels depends on the strength of the magnetic field and corresponds to radiation in the microwave region. Upon irradiation with suited frequencies, resonant absorptions between the levels occur. However, this technique is applicable only for clusters with a resulting spin, like small even-numbered carbon clusters appearing as linear chains in a triplet electronic ground state (e.g. [93]).

In ion mobility measurements, cluster ions are led through a cell filled with helium before mass selected by a quadrupole mass filter. It is easily accepted that the transit time of each ion through the drift cell depends on its mobility and thus on the average cross section. Thus, ions of the same mass have different transit times if they do not possess the same structure. Thereby, both the relative amount of the different isomers and their mobilities can be derived from the arrival time distribution after the mass selection [94].

Coulomb explosions emerge, when fast clusters impinge on a thin foil thereby stripping off the electrons. The remaining positively charged bodies are disrupted due to Coulomb repulsion. The exploding carbon ions can be detected depending on their arrival time and their position. The derived two-dimensional, macroscopic pattern of the ions mirrors the microscopic distribution of the original carbon atoms in the cluster [86], provided that the cluster structure is conserved during the electron stripping in the foil.

For studying clusters in matrices, carbon cluster gas diluted in pure rare gases like Ne or Ar is freezed out on a very cold substrate (10 - 20 K). In contrast to the gas phase methods introduced previously, the cluster molecules are trapped in a solid ‘grid‘ formed by the rare gas atoms. The clusters are further investigated by means of infrared, optical or UV spectroscopy since the matrix structure does not prohibit vibrational or electronical transitions. Careful annealing of the probe allows for the growth of larger clusters as well as the identificaton of correlated absorption peaks. The identification of species is mainly based on the comparison between calculated and measured spectra. Adding significant impurities of $^{13}C$ to the orignal carbon (mostly $^{12}C$) results in an increased number of absorption peaks due to the number of new molecules consisting of both carbon species (so-called isotopomers). The resulting isotopomeric shifts in vibrational spectra provide qualitative information on the cluster structure since a specific number of isotopomeric peaks is expected for a given geometry (e.g. [87]). It is further possible to combine matrix techniques with mass spectroscopy to record mass selected spectra which simplifies the cluster identification [19].

Infrared absorption spectroscopy has proven to be the most powerful tool for structure determination. In principle, measurements are performed by probing carbon cluster gas with an infrared laser and detecting the transmitted radiation. The transmitted signal shows absorption features at frequencies which excite rovibrational transitions of the molecule. The resulting spectrum provides a fingerprint

of the investigated molecule. Since the rotational energy of a molecule depends directly on the moment of inertia, the rotationally resolved spectra carry not only qualitative but also quantitative information on a molecule's geometry. It is neither necessary to ionise nor to destroy the clusters in order to determine their structure.

Up to date, only the linear isomers have been detected via their rovibrational spectra. The odd-numbered carbon clusters are fairly better known than the even-numbered ones, in the series of $C_n$ with odd n up to 13 only $C_{11}$ has not yet been detected [91]. The linear chains $C_4$ and $C_6$ were already known for several years [34, 46] when $C_{10}$ was identified through the detection of the rotationally resolved $\nu_6$ asymmetrical stretching mode in 2001 [26]. One year later, linear $C_8$ was detected for the first time in the gas phase [67]. Unfortunately, the signal-to-noise ratio appeared to be not sufficient to allow more than a tentative assignment of the transitions. Thus, further measurements of this transition were strongly recommended, particularly regarding the effects caused by the resulting spin.

As indicated before, the electronic ground state of carbon chains with an even number of atoms is a triplet state. As a result, all transitions in infrared spectra occur as triplets, that is every single absorption feature is splitted into three lines. The analysis of such spectra poses a challenge. In fact, from what is currently known, $C_8$ appears to be a kind of transition molecule, since the kin molecules, $C_4$ and $C_6$ on the one hand and $C_{10}$ on the other hand, have to be described in two different models.

The astrophysical relevance of the bending vibrations of carbon chains was already adressed. *Ab initio* calculations on various levels predict the lowest bendings for the $C_n$ chains with n = 3–10 to occur between 0.5 and 4 THz (e.g. [79, 91]). So far, $C_3$ is the only bare carbon chain for which direct measurements on a bending mode were performed in the laboratory [82]. However, information on the pure bending motions can be derived from infrared measurements of so-called 'hot bands'. This was done for $C_3$ [51], $C_4$ [63], $C_5$ [62], $C_7$ [36], and $C_9$ [88], providing the first estimations of their lowest bending frequency based on experimental work rather than calculations.

For $C_3$, it is evidenced by both experimental and theoretical investigations that the chain executes a large amplitude bending motion (e.g. [48, 60, 68]), thus, $C_3$ is termed a 'floppy' molecule. This conclusion led to some investigations concerning the floppiness of longer carbon chains. However, there is little doubt about the chains $C_4$, $C_5$, and $C_9$ to be quite rigid (e.g. [91]). But a controversal debate concerns the nature of the $C_7$ chain. Unlike the interpretation of existing experimental results (e.g. [36]), recent high-level *ab initio* calculations point at a fairly rigid chain [9]. To settle this question, further measurements on transitions involving the lowest bending mode were needed.

It comes clear, that even for the seemingly simple linear chains important aspects are still not well understood.

The main task of this thesis was to enlarge the currently available data set on the linear carbon chains with respect to two challenging aspects: the bending

dynamics of carbon chains and the spin-spin interaction in triplet states. Details concerning carbon clusters and the interpretation of their infrared absorption spectra are given in Chapter 2. In particular, properties of the bending modes as well as consequences of the triplet ground state of even-numbered chains are explained.

The measurements carried out in the course of this work were performed with the Cologne Carbon Cluster experiment. Given the experiences with the original setup of this infrared absorption spectrometer, it was a major part of this work to redesign the experiment with a significant increase of the signal-to-noise ratio in mind, especially with regard to rather weak hot band transitions. The revised setup is described in Chapter 3. Both the production of clusters and their detection are illustrated with emphasis on the necessary rearrangements.

In Chapter 4, new measurements and their subsequent analysis of the $\nu_5$ antisymmetric stretching mode of $C_8$ are described. Finally, the spectra of the $\nu_4$ fundamental and associated hot bands of $C_7$ are presented in Chapter 5. The results are discussed in context of the dispute concerning the floppiness.

# 2

# On Carbon Clusters

Most of the early investigations concerning carbon clusters have been triggered by astrophysical interest or the interest in the composition of carbon vapour (e.g. [31, 75]). With the discovery of the $C_{60}$ fullerene [54], the interest has conspicuously intensified.

Excellent reviews on carbon clusters have been given by W. Weltner Jr. and R.J. Van Zee [98] and by A. Van Orden and R.J. Saykally [91] summarising both theoretical and experimental work on carbon clusters up to 1989 and 1998, respectively. Additionally to the results outlined in the review articles, the gas phase detections of the two even-numbered linear chains $C_{10}$ and $C_8$ have to be mentioned here [6, 26, 67].

The following chapter is divided into two parts. In the first section, a brief overview is given on the most likely structures of small carbon clusters as derived by *ab initio* calculations and various experimental studies. Due to the orientation of this work, the section mainly focusses on linear carbon chains and their properties with emphasis on bending dynamics. The second part provides tools necessary to analyse infrared spectra of linear carbon chains.

## 2.1 Structures of Carbon Clusters

The versatility of the carbon bond leads to an enormous variety of cluster structures. The more atoms included in the clusters, the more structures are imaginable. For a cluster as large as $C_{20}$ not only linear or planar structures are conceivable but also bowls of different shapes and even a variety of cage-like, that is fullerene, structures have been predicted (e.g. [49]). Apart from the mere structure determination against the number of carbon atoms, the growth process of the fullerenes is object of many speculations. Time-of-flight (TOF) mass spectrometry of supersonic carbon cluster beams revealed a bimodal mass distribution [80] providing evidence for different production mechanisms for small and large clusters, respectively.

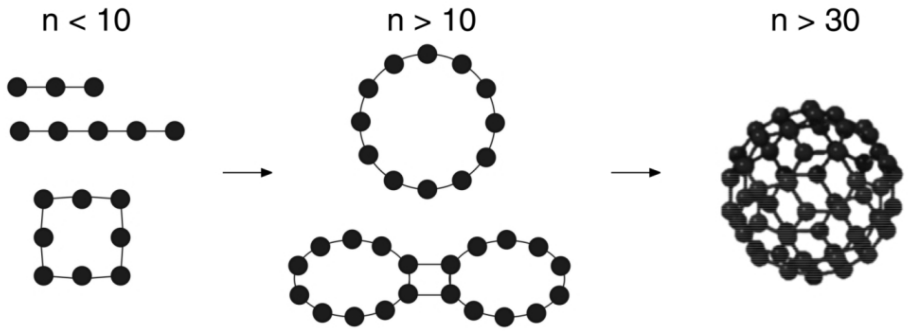


Figure 2.1: Possible configurations for carbon clusters of different sizes after [59]. With increasing size the structures become more complex leading to geometries like the displayed Buckminster fullerene $C_{60}$.

However, the study of the smaller members of the cluster family is a necessary step on the road of understanding the formation and properties of larger clusters.

Accurate *ab initio* calculations are beyond doubt a high-performance support to study the possible geometries of pure carbon molecules. Though differing in detail, all calculations agree upon different equilibrium geometries depending on the cluster size. Small clusters are predicted to exist rather as linear chains or potentially as cyclic structures in case of the even-numbered clusters. With increasing chain length the energy of the linear structure becomes larger than the energy of the corresponding cyclic geometry [44, 49]. For larger clusters, three-dimensional cage-like structures become energetically favourable. Figure 2.1 gives an impression of the possible geometries.

A number of ten atoms appears to be the magical quantity for the transition between linear and cyclic geometries in theoretical studies [56, 79]. This assumption is supported by photodetachment studies where a fourfold periodicity is found for more than ten atoms pointing at ring structures for this size range [102].

In the following, more details are given on possible structures for small clusters $C_n$ with $n < 10$.

### 2.1.1 Small Carbon Clusters

In principle, there is not much doubt about the linear character for odd-numbered clusters with few atoms. There have been only minor deviations between calculated values for bond lengths, and, in case of $C_3$, discussions about a possible small bond angle. The structures of small even-numbered clusters have been found to be more tricky. Depending on the level of calculation, either a linear or a planar cyclic geometry have been predicted to be of lower energy.

Figure 2.2 shows the calculated equilibrium geometries for clusters up to ten atoms. In all cases, those structures were considered which were derived from the highest level of calculation. For the even-numbered ones, both chain and

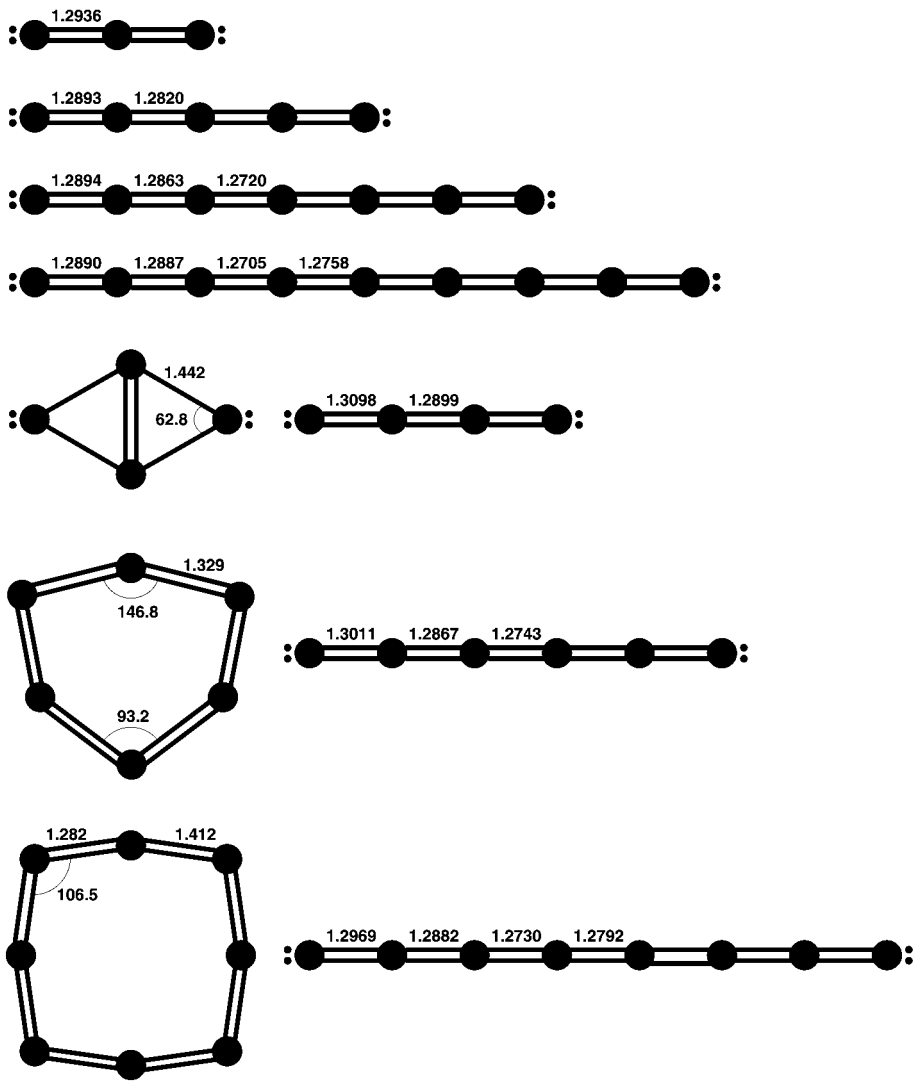


Figure 2.2: Calculated equilibrium structures for small carbon clusters $C_n$ ($n<10$). For odd-numbered clusters the linear singlet geometries are predicted to be lowest in energy while for even-numbered clusters two distinct low-lying states are favoured depending on the level of calculation: a linear triplet state and a cyclic singlet one. Bond lengths are given in Å and angles in degrees. Values for odd-numbered clusters have been calculated by P. Botschwina by means of coupled cluster methods [8]. The geometries for the even-numbered clusters are taken from various sources. P. Botschwina has calculated the bond lengths for the linear chains [10]. The values for rhombic $C_4$ are taken from coupled cluster calculations by Watts *et al.* [97]. Values given for cyclic $C_6$ have been derived by Hutter *et al.* [45]. Martin *et al.* have calculated the geometry given for $C_8$ [59].

ring isomers are displayed. Concerning $C_4$, the cumulenic linear chain and a bicyclic rhombic structure are predicted to be nearly isoenergetic [97]. An experimental evidence for the rhombic structure has been provided by Coulomb explosion images [1, 86]. For $C_6$, a distorted hexagon of $D_{3h}$ symmetry and its linear counterpart are each favoured by one or another of the available theoretical methods ([45, 76, 79] and [72], respectively). The same holds for $C_8$, where the energy of the linear isomer is compared to that of an acetylenic ring with $C_{4h}$ symmetry [59]. Experimental indications for cyclic isomers of both $C_6$ and $C_8$ can be obtained from infrared matrix spectra [77, 95, 96]. However, according to ESR measurements, the $C_4$, $C_6$, and $C_8$ molecules are linear [31, 93].

### 2.1.2 Linear Chains

*Ab initio* results indicate a significant difference between odd- and even-numbered carbon chains $C_n$ ($n < 10$) concerning their electronic ground state. The same strong even-odd alternation is evidenced in photodetachment studies [2].

To enlighten this alternation, molecular orbital (MO) theory has to be considered according to the work of K.S. Pitzer and E. Clementi [75]. The bonding character inside a linear chain $C_n$ is cumulenic. Of the 4 n valence electrons, four electrons exist as unpaired electrons at the chain's ends. Half of the remaining electrons occupy $\sigma$-orbitals, the other half are $\pi$-electrons. That leaves (2 n - 2) electrons in $\pi$-orbitals. Every $\pi$-orbital can be occupied by four electrons. As a consequence, for an odd-numbered chain, the highest occupied molecular orbital (HOMO) is filled completely (see Figure 2.3), resulting in a singlet electronic ground state ($^1\Sigma_g^+$). The electronic ground state for an even-numbered chain is a triplet state ($^3\Sigma_g^-$), since the HOMO is only half-filled and both spins are parallel according to Hund's rule.

#### Infrared detections of linear carbon chains

High resolution spectroscopy is by far the most accurate experimental method to determine the structures of carbon clusters. The resulting pattern in an absorption spectrum is directly correlated to a molecule's moment of inertia, if the molecule is allowed to rotate (see section 2.2). Due to the lack of a permanent dipole moment, rotations of linear carbon chains can only be excited by electromagnetic radiation in combination with vibrations. Bendings or antisymmetric stretchings of a chain lead to a so-called vibrational dipole moment, since the centers of mass and charge get separated through the motion. This dipole moment is oriented along the molecular axis for the antisymmetric stretchings but perpendicular to the axis for the bending modes.

Starting from the predicted geometries, the possible vibrational modes can be calculated on various levels of theory. The *ab initio* predictions for the vibrational frequencies usually vary concerning the exact values but agree about the approximate frequency range. The antisymmetric stretching modes occur in the

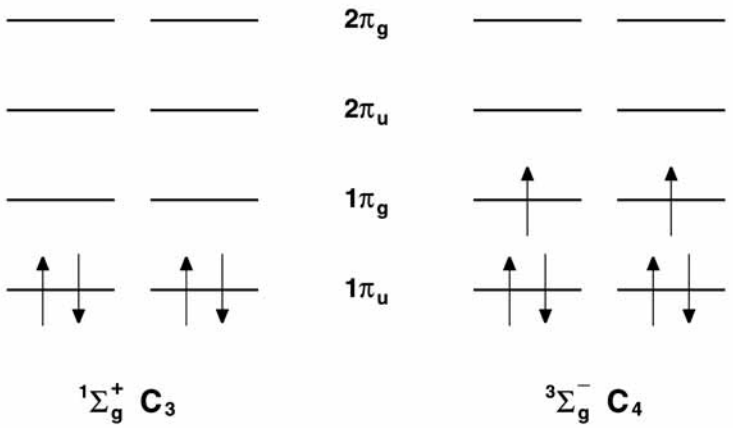


Figure 2.3: Highest occupied molecular orbitals (HOMOs) for linear $C_3$ and $C_4$: carbon chains $C_n$ possess $4n$ valence electrons whereof $(2n-2)$ are $\pi$-electrons. Thus, clusters with an odd number of carbon atoms have a completely filled HOMO resulting in a singlet electronic ground state. The HOMOs of even-numbered chains are just half-filled leading to a triplet ground state.

infrared region while the bending modes are related to the THz- or far-infrared domain (e.g. [44, 59, 79]).

Currently, spectroscopy in the THz domain is still a very challenging task. Thus, most of the previous spectroscopic studies of carbon clusters have been devoted to the infrared-active stretching modes [91]. The only appropriate radiation sources in the infrared region are so-called tunable diode lasers (see section 3.2.1). Unfortunately, they are not well suited for scans over wide frequency regions. Given the uncertainty of predicted frequencies, spectroscopists heavily rely on infrared vibrational spectra of cold matrix isolated clusters and their assignment to antisymmetric stretching modes by *ab initio* calculations.

So far, only linear carbon clusters have been detected by means of rovibrational spectroscopy. Table 2.1 summarises all these measurements along with values for the band origins derived from matrix spectra. Regarding the predicted equilibrium geometry, the detection of a linear isomer of $C_{13}$ is at least astonishing and started many discussions after publication. However, it was not necessarily the molecule's energetically lowest structure that has been detected by Giesen *et al.* [25].

The detection of the $\nu_2$ bending mode of $C_3$ by Schmuttenmaer *et al.* [82] constitutes the only direct observation of a bending vibration up to date. Still, the evaluation of hot band measurements in the infrared (see section 2.2.1) provides information on the pure bendings. By this means, results concerning the bending potentials of $C_4$, $C_5$, $C_7$, and $C_9$ could be derived (see Table 2.2), which are presented in the following section.

Table 2.1: Infrared-active vibrational transitions of linear carbon clusters measured in isolated rare gas matrices and rotationally resolved in the gas phase. All values are given in $cm^{-1}$. In cases where more than one analysis was performed, the result from the latest fit rather than from the first detection is given for the gas phase value of the band origin. The band origin for $C_8$ was derived from tentative assignment. Matrix values are taken from [19, 65] and references therein. For $C_{13}$, a matrix reference value of 1816 $cm^{-1}$ can be taken from measurements in oxygen matrices at 25 K [83].

| | Mode | Ar matrix | Ne matrix | Gas phase |
|---|---|---|---|---|
| $C_3$ | $\nu_2$ | 83.0 | 75.0 | 63.416549(40) [82] |
| | $\nu_3$ | 2038.9 | 2036.4 | 2040.0198(8) [60] |
| $C_4$ | $\nu_3$ | 1543.4 | 1547.2 | 1548.6128(4) [63] |
| | $\nu_5$ | 172.4 | | |
| $C_5$ | $\nu_3$ | 2164.3 | 2166.4 | 2169.4410(2) [62] |
| | $\nu_4$ | 1446.6 | 1444.3 | |
| $C_6$ | $\nu_4$ | 1952.5 | 1958.7 | 1959.85852(18) [46] |
| | $\nu_5$ | 1197.3 | 1199.3 | |
| $C_7$ | $\nu_4$ | 2127.8 | 2134.6 | 2138.3152(5) [36] |
| | $\nu_5$ | 1894.3 | 1897.5 | 1898.3758(8) [37] |
| $C_8$ | $\nu_5$ | 2063.9 | 2067.8 | 2067.9779 [67] |
| | $\nu_6$ | 1705.6 | 1707.4 | |
| $C_9$ | $\nu_5$ | 2077.9 | 2081.1 | 2079.67358(17) [89] |
| | $\nu_6$ | 1998.0 | 2010.0 | 2014.277964(67) [88] |
| | $\nu_7$ | 1601.0 | | |
| $C_{10}$ | $\nu_6$ | | 2074.5 | 2074.4109(2) [26] |
| | $\nu_7$ | | 1897.5 | |
| $C_{11}$ | $\nu_7$ | | 1938.6 | |
| | $\nu_8$ | | 1897.5 | |
| $C_{12}$ | $\nu_8$ | | 2003.9 | |
| $C_{13}$ | $\nu_9$ | | | 1808.96399(7) [25] |

Table 2.2: Measured infrared hot bands of linear carbon chains. Band origins are given without uncertainties in cases where $e$ and $f$ components have been analysed separately (see section 2.2.1). All values are given in $cm^{-1}$.

| | Transition | Band Origin |
|---|---|---|
| $C_3$ | $\nu_2 + \nu_3 - \nu_2$ | 2015.08 [51] |
| | $2\nu_2 + \nu_3 - 2\nu_2$ | 1994.3461(10) ($\ell = 0$) [51] |
| $C_4$ | $\nu_3 + \nu_5 - \nu_5$ | 1547.9749(3) [63] |
| | $\nu_3 + 2\nu_5 - 2\nu_5$ | 1546.3164(5) ($\ell = 0,2$) [22] |
| | $\nu_3 + \nu_4 - \nu_4$ | 1548.0101(3) [64] |
| $C_5$ | $\nu_3 + \nu_7 - \nu_7$ | 2167.8497(9) [62] |
| | $\nu_3 + 2\nu_7 - 2\nu_7$ | 2166.2331(3) ($\ell = 0,2$) [22] |
| | $\nu_3 + \nu_5 - \nu_5$ | 2165.9474(4) [62] |
| $C_7$ | $\nu_4 + \nu_{11} - \nu_{11}$ | 2136.0687(9) [36] |
| | $\nu_4 + 2\nu_{11} - 2\nu_{11}$ | 2133.8020(29) ($\ell = 0$) [36] |
| $C_9$ | $\nu_6 + \nu_{15} - \nu_{15}$ | 2014.18 [89] |
| | $\nu_6 + 2\nu_{15} - 2\nu_{15}$ | 2014.0192(14) ($\ell = 0$) [89] |

### Bending Potentials

For $C_3$, accurate theoretical studies of the bending potential by Northrup *et al.* [68] as well as Jensen *et al.* [48] yielded an increased rigidity of the chain upon exciting the symmetric stretching mode. On the contrary, a barrier to linearity occurs upon exciting the antisymmetric stretching mode. This behaviour is known as ‘quasi linearity‘. As a result, $C_3$ performs a large amplitude bending motion which was evidenced by high resolution spectroscopic studies [51, 82].

The extraordinary shallow bending potential of the $C_3$ chain prompted investigations on a possible ‘floppiness‘ of longer carbon chains. The chain molecules $C_4$, $C_5$, and $C_9$ appear to be quite rigid, a finding which is confirmed by quantum mechanical calculations [91]. But from their analysis of hot bands of the $C_7$ chain, Saykally *et al.* [36] concluded $C_7$ to be another floppy chain.

Following the argumentation of Fan and Pfeiffer [18], this circumstance was explained by Saykally and his co-workers [91] with the nature of the highest occupied molecular orbital (HOMO). For the $C_3$, $C_6$, $C_7$, and $C_{10}$ chains the HOMO is of $\pi_u$ symmetry. Hence, upon bending about their center of symmetry, these chains should exhibit a constructive overlap of the valence orbitals, whereas destructive overlap occurs for the $C_4$, $C_5$, $C_8$, and $C_9$ chains due to the $\pi_g$ symmetry of their HOMO. The constructive overlap may lead to an enhancment of the bending vibrational motion resulting in large amplitudes.

One has to keep in mind, that this theory of alternating rigidity in carbon chains was based mainly upon the analysis of the $C_7$ chain since neither for $C_6$ nor for $C_{10}$ hot band measurements were available at that time[2]. However, the evidence

[2]There are still no such measurements to date.

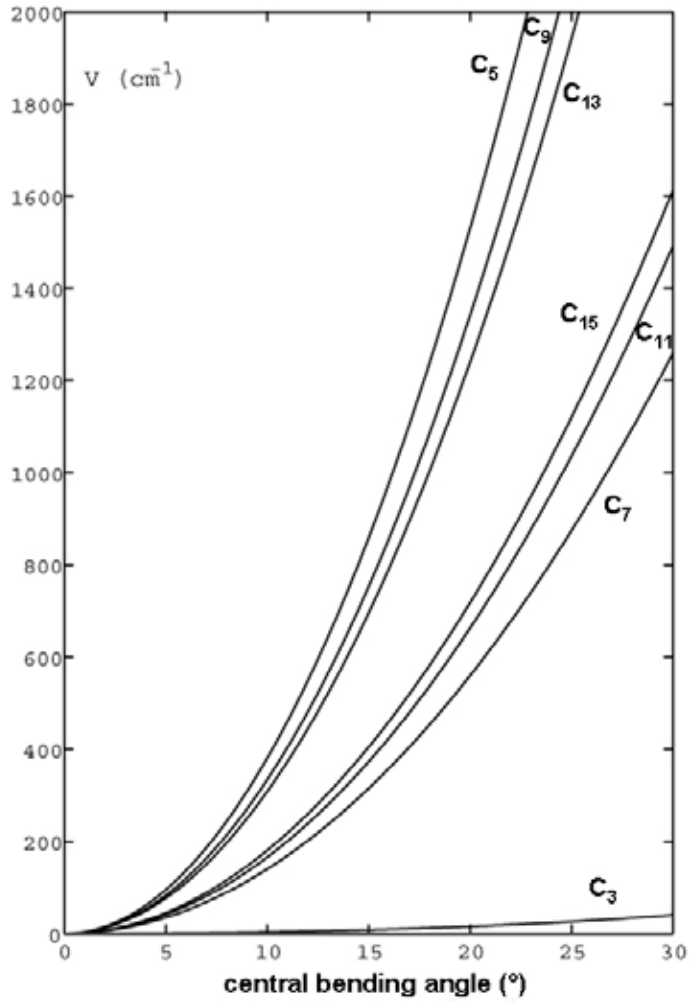


Figure 2.4: Calculated potentials for the lowest bendings of odd-numbered carbon chains [12].

for this theory falls somewhat short of a proof.

Still, the floppiness of $C_7$ was more or less commonly accepted until P. Botschwina published high-level coupled cluster calculations on $C_7$ in 2002 [9]. These *ab initio* calculations showed no evidence of floppiness for the $C_7$ chain. Figure 2.4 shows the calculated potentials of the lowest bendings for the odd-numbered carbon chains up to $C_{15}$. Comparing these potentials, one can distinguish between three groups of molecules. The shapes of the potentials of the $C_5$, $C_9$, and $C_{13}$ chains as well as those of the $C_7$, $C_{11}$, and $C_{15}$ chains look quite similar, which may correspond to the classification concerning the nature of the HOMO mentioned above. However, all of them can be regarded as harmonic potentials. On the contrary, $C_3$ appears to be an exceptional molecule with unusual bending properties.

The discrepancy between the interpretation of existing measurements and high-level calculations was the main reason for the reinvestigation of $C_7$. Results of this work are presented in chapter 5.

## 2.2 Analysing Infrared Spectra of Linear Carbon Chains

The following section provides necessary information to understand the later presented results on the spectra of $C_7$ and $C_8$. A more detailed insight into the quantum mechanical approach to describe absorption spectroscopy is given in the textbooks by P.F. Bernath [5], W. Gordy & R.L. Cook [29], and G. Herzberg [40].

If treated by means of quantum mechanics, a molecule is described by its Hamilton operator $\mathbf{H}$ (hereafter Hamiltonian) representing its energy. Solving the stationary Schrödinger equation (2.1) leads to energy eigenvalues $E$ corresponding to discrete energy levels. Transitions between these levels occur upon absorption or emission of energy in the form of electromagnetic radiation.

$$\mathbf{H}\Psi = E\Psi \tag{2.1}$$

Assuming that electrons move faster than the nuclei, the wavefunction $\Psi$ of a molecule can approximately be written as product of eigenfunctions (Born-Oppenheimer-Approximation):

$$\Psi = \Psi_{el}\,\Psi_{vib}\,\Psi_{rot}\,\Psi_{ns} \tag{2.2}$$

Here, the function $\Psi_{el}$ considers motions of electrons, $\Psi_{vib}$ and $\Psi_{rot}$ represent vibration and rotation of the molecule, while $\Psi_{ns}$ accounts for nuclear spin effects.

The same principle can be applied for the Hamiltonian, which leads to

$$\mathbf{H} = \mathbf{H}_{el} + \mathbf{H}_{vib} + \mathbf{H}_{rot} + \mathbf{H}_{ns}. \tag{2.3}$$

As a first step, the linear molecule is assumed to be a rigid rotor performing solely rotational transitions. According to the classical treatment, the pure rotational Hamiltonian is given by

$$\mathbf{H}_{rot} = \frac{\mathbf{J}^2}{2I} \tag{2.4}$$

where $\mathbf{J}$ is the operator of the total angular momentum, and $I$ denotes the moment of inertia. The corresponding energy eigenvalues are derived to

$$F(J) = B\,J(J+1). \tag{2.5}$$

where the quantum number $J$ represents the eigenvalue of $\mathbf{J}$. In wavenumbers, the rotational constant $B$ is defined as

$$B = \frac{h}{8\,\pi^2\,I} \cdot 10^{-2}\ \left[\mathrm{cm}^{-1}\right]. \tag{2.6}$$

Transitions between different rotational levels are subject to so-called selection rules due to the preservation of the angular momentum. For a pure rotational transition, one derives the condition

$$\Delta J = \pm 1. \tag{2.7}$$

Therewith, the transition frequencies for a rigid rotor are calculated to

$$\nu_{J+1 \leftarrow J} = 2\, B_v\, (J+1), \tag{2.8}$$

resulting in a pattern of equidistant lines in the spectrum, where the lines are separated by $2\,B$. As can be taken from equation (2.6), the determination of the rotational $B$ constant yields information on the moment of inertia $I$, and thereby on the molecule's structure. Effective bond distances and angles may be derived.

If the molecule is allowed to vibrate and rotate simulateneously, as is the case for the $C_n$ chains, the rotational constant changes with the vibrational state due to the change in geometry. To get the overall rotational constant, one has to sum over all possible modes using

$$B_v = B_e - \sum_i \alpha_i \left( v_i + \frac{d_i}{2} \right) \tag{2.9}$$

where $B_e$ is the equilibrium rotational constant, $v_i$ means the vibrational quantum number of the $i$-th excited state, and $d_i$ is degree of degeneracy of that state. The coupling of rotational and vibrational motion is represented by the constants $\alpha_i$.

For bending modes of linear molecules, the energy levels characterised by $v$ show a $v+1$ degeneracy. In case of $v = 1$, this can be understood in a classical picture: if the linear chain is oriented along the $z$-axis, then the bending can occur in the $xz$- as well as the $yz$-plane both being indistinguishable. The superposition of both bendings can be treated as circular motion. Thus, the twofold degeneracy can be interpreted in terms of clockwise or counterclockwise rotation.

In general, the resulting 'vibrational' angular momentum occurs quantised in units of $\pm\ell\hbar$. Possible values for $|\ell|$ are $v, v-2, \ldots 0$ or 1. The associated states are labelled in the same way as states with orbital angular momentum $L$: $\ell = 0, 1, 2, \ldots$ correspond to $\Sigma, \Pi, \Delta, \ldots$ states.

As a consequence, the energy of a rovibrational level can be written as

$$F(J, v) = \nu_v + B_v \left[ J(J+1) - \ell^2 \right] \pm \frac{1}{2}\, q_v\, J(J+1). \tag{2.10}$$

Here, $q_v$ denotes the '$\ell$-type doubling constant' accounting for the energy difference between positive and negative value of $\ell$. The rotational quantum number $J$ is limited to the values $|\ell|, |\ell|+1, |\ell|+2, \ldots$. For antisymmetric stretching modes, $\ell$ equals zero.

Up to now, the linear chains have been treated in a rigid rotor approximation. Actually, the bondings between the nuclei may change upon rotation, whether it be to lengthen or to shorten. Therefore, centrifugal distortion effects have to be taken into account leading to the model of the non-rigid rotator:

$$\begin{aligned} F(J,v) &= \nu_v + B_v\,[J(J+1)-\ell^2] - D_v\,[J(J+1)-\ell^2]^2 + H_v\,[J(J+1)-\ell^2]^3 + \ldots \\ &\quad \pm \frac{1}{2}\,q_v\,J(J+1) \pm \frac{1}{2}\,q_v^J\,[J(J+1)]^2 \pm \frac{1}{2}\,q_v^{JJ}\,[J(J+1)]^3 \end{aligned} \tag{2.11}$$

$D_v$ and $H_v$ are called quartic and sextic centrifugal distortion constants. Since both values depend on the vibrational state, they can be expressed in a way similar to equation (2.9). The constants $q_v^J$ and $q_v^{JJ}$ are corrections considering distortion effects on the $\ell$-type splitting. Centrifugal terms of higher order in $J$ are neglected in (2.11).

### Selection Rules

Transitions between two energy levels[3], $E''$ and $E'$, are only possible when the so-called transition moment $M$ is different from zero, since the intensity of a transition depends on $|M|^2$. For electronic dipole transitions with dipole moment $\boldsymbol{\mu}$ the transition moment is determined according to

$$M = \int \Psi'\,\boldsymbol{\mu}\,\Psi'' d\tau. \tag{2.12}$$

Due to the integration, a totally symmetric function $\Psi'\,\boldsymbol{\mu}\,\Psi''$ is necessary to have a non-vanishing result for $M$. Thus, symmetry considerations are a useful tool to check whether certain transitions are allowed or forbidden.

The derived selection rules for parallel bands ($\Delta\ell = 0$) are $\Delta J = \pm 1$ if $\ell = 0$ in both upper and lower state, and $\Delta J = 0, \pm 1$ if $\ell \neq 0$. For perpendicular bands ($\Delta\ell = \pm 1$), one derives $\Delta J = 0, \pm 1$. To account for all possible rovibrational transitions, the following criteria must be fulfilled for a non-vanishing transition probability:

$$\Sigma^- \nleftrightarrow \Sigma^+\,;\; \Delta v = 1\,;\; g \nleftrightarrow g\,;\; u \nleftrightarrow u\,,$$

where the labels $g$ and $u$ refer to a state's gerade and ungerade symmetry with respect to the inversion operation.

As a result, rovibrational spectra show a clear pattern. The spectra consist of a '*P*-branch' composed of transitions with $\Delta J = -1$ in the lower frequency range and a higher frequency '*R*-branch' with $\Delta J = +1$ transitions. For perpendicular bands, a *Q*-branch ($\Delta J = 0$) occurs between *P*- and *R*-branch.

[3] It is common practice to designate the lower energy level with $E''$, the upper one with $E'$. The same labels are used for the corresponding wavefunctions.

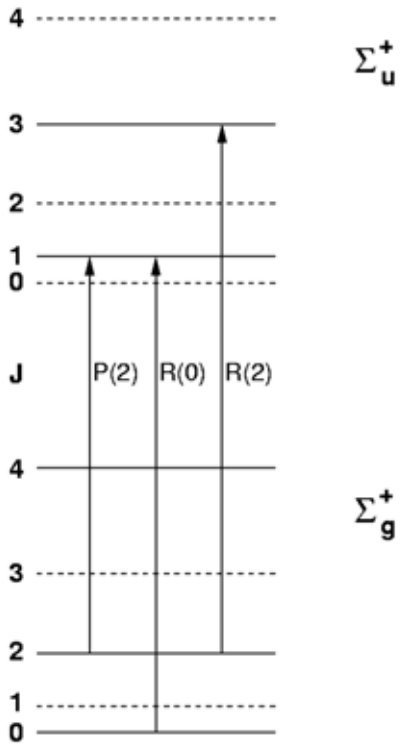


Figure 2.5: Energy level scheme for odd-numbered carbon chains: lower stack represents rotational levels of vibrational ground state having $\Sigma_g^+$ symmetry, upper stack illustrates rotational levels of vibrationally excited state with $v = 1$, $\ell = 0$ and $\Sigma_u^+$. In both states every second rotational level is missing due to spin statistics (indicated by broken lines). But due to the change in $g/u$ symmetry, levels with odd valuess of $J$ are missing in the lower state while levels with even $J$-values are forbidden in the upper state. Some possible rovibrational transitions are marked with arrows.

In order to analyse the spectra of pure carbon chains, one effect has not been considered so far. The overall wavefunction of a $C_n$ chain is ruled by Bose-Einstein statistics due to the nuclear spin $I = 0$ for the main isotope $^{12}C$. To account for the indistinguishability of the carbon atoms within the chain, the wavefunction $\Psi$ has to be totally symmetric. According to equation (2.2), the product $\Psi_{el}\,\Psi_{vib}\,\Psi_{rot}$ has thus to be symmetric, since $\Psi_{ns}$ is certainly symmetric. The electronic ground state is different for odd- and even-numbered clusters leading to different spin statistical weights for the rotational levels.

### 2.2.1 Odd-numbered Carbon Chains

For carbon chains with an odd number of atoms, the electronic ground state is totally symmetric as is the vibrational ground state[4]. Thus, the rotational states

[4]The vibrational ground state is totally symmetric in any case.

have to be of the very same symmetry. The symmetry of rotational levels depends on the corresponding quantum number $J$. As a consequence, only levels with even $J$ are allowed in the vibrational ground state. Since the symmetry of the excited vibrational level is different, there are only levels with odd $J$ in the upper state. The situation is depicted in Figure 2.5. Rotational levels forbidden by spin statistics are denoted with broken lines. The lowest possible rovibrational transitions are indicated by arrows.

Antisymmetric stretching modes of odd-numbered linear chains can be described by a simplification of the energy expression given in equation 2.11:

$$E = \left(v + \frac{1}{2}\right)\nu + B_v[J(J+1)] - D_v[J(J+1)]^2 \ldots \tag{2.13}$$

The resulting spectra display clear *P*- and *R*-branch patterns with 4 $B$ spacing between the lines. The band origin can be easily identified due to a 6 $B$ gap.

### Hot Bands

In spectroscopy, any vibrational transition not involving the ground state is designated as hot band transition. Bands of type $v_{bend} + v_{stretch} \leftarrow v_{bend}$ occur in the same frequency region than the fundamental stretching mode involved. Their evaluation yields rotational constants for both states involved thereby providing information on the bending level. Furthermore, the derived values for the $\ell$-type doubling constant $q$ allow for estimation of the band origins of the pure bendings by using the approximation

$$\nu \approx \frac{f_q B_0^2}{q}, \tag{2.14}$$

where $f_q$ takes into account a possible coupling of modes due to Coriolis interaction. A more detailed description on this subject is given in the textbook by D. Papoušek & M.R. Aliev [71].

As an example, some energy levels and hot band transitions for $C_7$ are shown in Figure 2.6. Every $v = 1$ state ($\Pi$ symmetry) splits into two levels labeled with $e$ and $f$, due to the vibrational angular momentum. The same holds for the corresponding upper state. Due to selection rules, transitions with $\Delta\ell = 0$ are only allowed between levels of the same symmetry, that is $e \nleftrightarrow f$. The corresponding rovibrational energy expressions for $e$- and $f$-subbands neglecting higher centrifugal distortion terms are given by:

$$F(J,v)_{e/f} = \nu_v + B_v\left[J(J+1) - \ell^2\right] - D_v\left[J(J+1) - \ell^2\right]^2 \mp \frac{1}{2}\, q_v\, J(J+1) \tag{2.15}$$

For the odd-numbered carbon chains, the spectrum of a hot band with one quantum in the bending mode displays a staggering of adjacent rotational lines. This staggering of lines originates in nuclear spin statistics. Every second level of the usually allowed $\ell$-type doublets is missing depending on the overall symmetry.

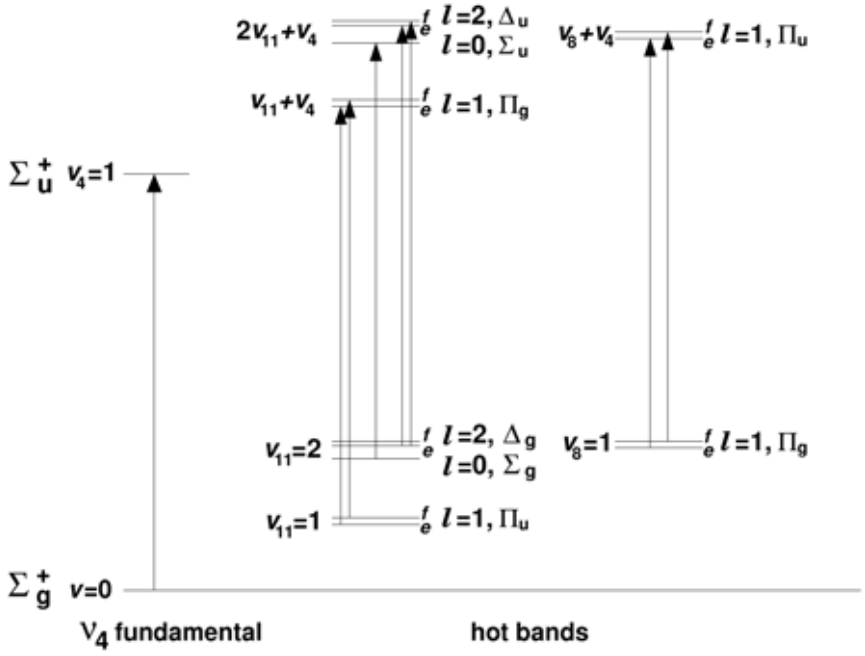


Figure 2.6: Energy level scheme including hot band transitions for odd-numbered chains: the two energy levels involved in the fundamental transition are shown left. Hot bands may arise from low-lying bending levels, in case of $C_7$ the $\nu_{11}$ and $\nu_8$ modes have to be considered. Allowed transitions are depicted with arrows. Note, that the energy axis is not to scale.

Since the symmetry depends on $J$ even or odd, alternately the upper or the lower level of the doublet is missing. As a result, the distance between successive lines is in turn slightly larger or smaller than $2\,B$. Figure 2.7 illustrates the alternating distances.

States with two quanta in the bend consist of three levels due to the possible values $\ell = 0$ or $\ell = 2$ for the vibrational angular momentum. As for $(v = 1, \ell = 1)$, the $\ell = 2$ level consists of an $e$- and an $f$-sublevel. Usually, the energy of the $\ell = 0$ level is lower than that of the corresponding $\ell = 2$ level. Since there is no splitting for the $\ell = 0$ levels, a $\Sigma - \Sigma$ hot band spectrum resembles that of the fundamental showing a $4\,B$ spacing. For $\Delta - \Delta$ hot bands, the lines occur in a $2\,B$ spacing with a staggering of successive lines observable for high $J$ values only.

### 2.2.2 Even-numbered Carbon Chains

For even-numbered carbon chains, the triplet character of the electronic ground state becomes apparent in the rovibrational spectrum due to spin-orbit coupling. In addition to the pure rotational angular momentum $\mathbf{N}$, a spin operator $\mathbf{S}$ has to be considered. The Hamiltonian includes the coupling of these two angluar momenta[5].

[5]Note, that $\mathbf{J}$ was defined as operator of the total angular momentum.

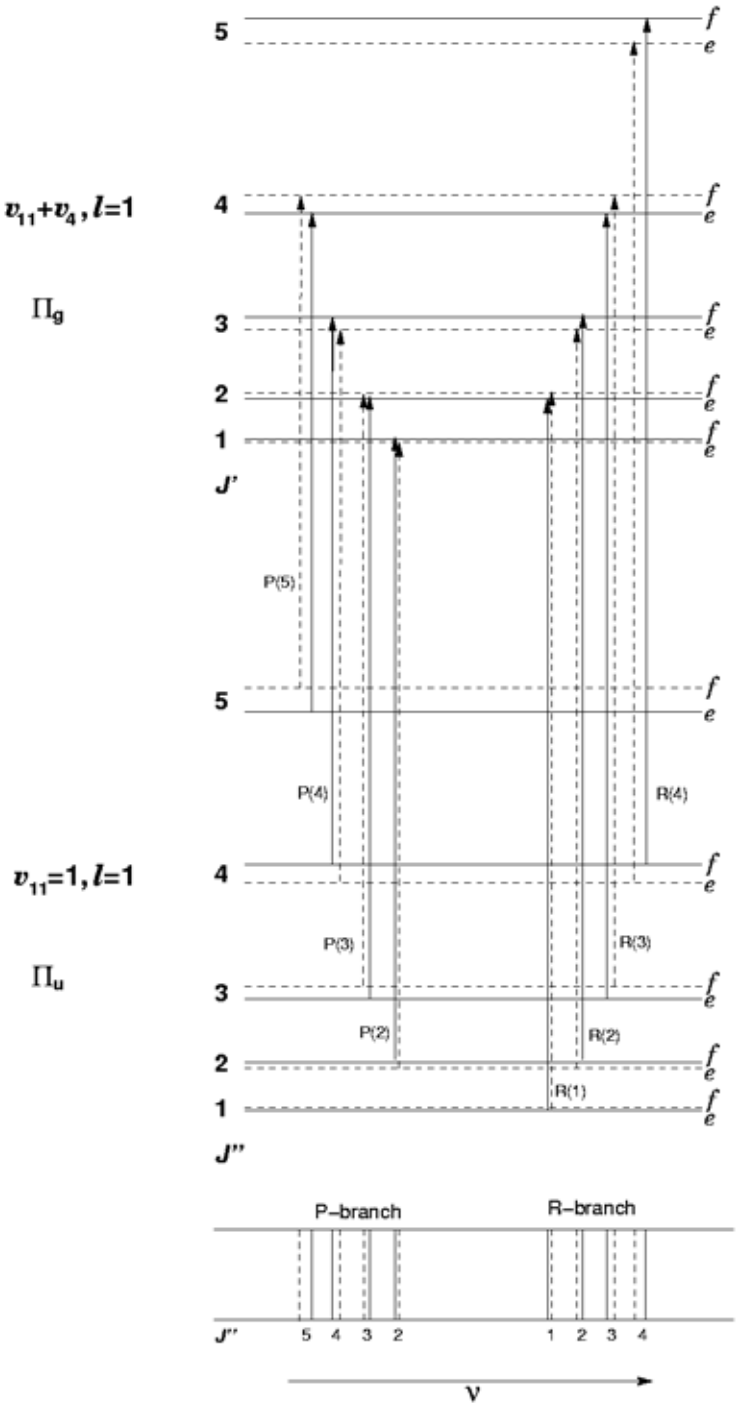


Figure 2.7: Origin of the staggered line pattern for hot band transitions of odd-numbered carbon chains. Due to spin statistics, alternately the $e$ or $f$ levels in both vibrational states are missing (depicted with broken lines). The resulting line pattern shows varying distances. The energy levels are again labelled with respect to $C_7$.

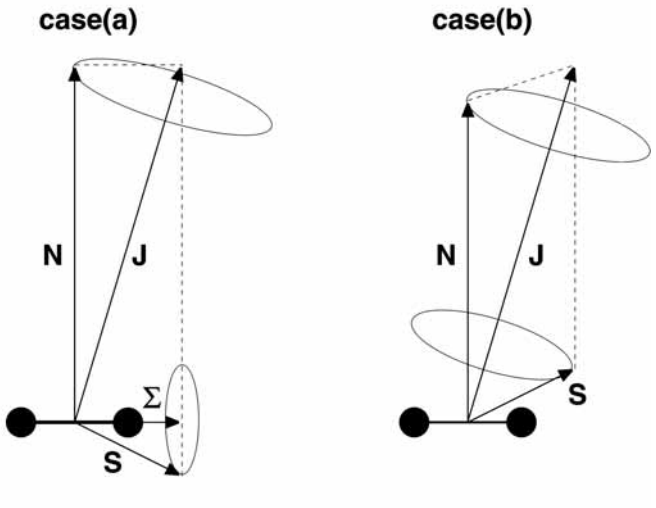


Figure 2.8: Coupling schemes for Hund's case (a) and (b) for $\Sigma$ states neglecting orbital angular momentum: in case (a) limit, the spin $\mathbf{S}$ couples completely to the molecular axis. Both molecular axis and $\mathbf{N}$ precess about the direction of $\mathbf{J}$. In case (b) limit, $\mathbf{S}$ is coupled to $\mathbf{N}$ to form a resultant $\mathbf{J}$. Both cases are idealised. Drawn after [29].

The following illustration is confined to $^3\Sigma$ electronical states, thus, it is not necessary to consider an additional orbital angular momentum. Furthermore, hot band transitions are not regarded here.

More details on the spin coupling for $^3\Sigma$ state molecules are given by J.B. Tatum & J.K.G. Watson [85] and in the text book by W. Gordy & R.L. Cook [29] as well as references therein.

### Spin-Spin Interaction

The spins of the two unpaired electrons of the $^3\Sigma$ state give rise to a magnetic term in the Hamiltonian. The spin-spin interaction is proportional to $(3\cos^2\theta - 1)$ where $\theta$ is the averaged value of the angle between molecular and $\mathbf{S}$ axis. This interaction is of dipole-dipole type. Moreover, an interaction between the electronical ground state and an excited state with a non-zero orbital angular momentum may occur, resulting in an additional contribution to the magnetic term. The latter interaction increases with decreasing energy gap of the involved electronic states. Since both types of interactions have the same angular dependence, one constant is associated to both interactions, the spin-spin coupling constant $\lambda$.

Due the interaction of the electronic states, the spins may be aligned along the molecular axis, which corresponds to a coupling of momenta in Hund's case (a) limit. Figure 2.8 illustrates an idealised coupling according to Hund's case (a) in comparison to that of case (b).

The effective spin-rotational Hamiltonian $\mathbf{H}_{SR}$ for a $^3\Sigma$ electronic state is given by

$$\mathbf{H}_{SR} = B_v\,\mathbf{N}^2 - D_v\,\mathbf{N}^4 + \frac{2}{3}\,\lambda_v\,(3\mathbf{S}_z^2 - \mathbf{S}^2) + \gamma_v \mathbf{NS} \tag{2.16}$$

where the first two terms represent the rovibrational energy, the third term considers spin-spin interaction with the interaction constant $\lambda_v$, and the last term accounts for spin-rotation interaction with the corresponding constant $\gamma_v$. The index $v$ designates the vibrational dependency of the involved constants again.

To obtain the energy eigenvalues for this Hamiltonian, the appropriate procedure is diagonalising the corresponding energy matrix

$$\begin{array}{l} N = J-1 \\ N = J \\ N = J+1 \end{array} \begin{pmatrix} a & 0 & d \\ 0 & b & 0 \\ d & 0 & c \end{pmatrix}, \tag{2.17}$$

where $N$ is the rotational quantum number, and $a$, $b$, $c$, and $d$ are given by equations (2.18)-(2.21). In the present case, $J = N + S$ gives $N = J - 1$, $N = J$, and $N = J + 1$, respectively.

$$a = B\,J(J-1) - D\,[J(J-1)]^2 + \gamma\,(J-1) + \left(\frac{2}{3} - \frac{2J}{2J+1}\right)\,\lambda \tag{2.18}$$

$$b = B\,J(J+1) - D\,[J(J+1)]^2 - \gamma + \frac{2}{3}\lambda \tag{2.19}$$

$$c = B\,(J+1)(J+2) - D\,[(J+1)(J+2)]^2 + \gamma(J+2) + \left(\frac{2}{3} - \frac{2(J+1)}{2J+1}\right)\lambda \tag{2.20}$$

$$d = 2\,\frac{\sqrt{J(J+1)}}{2J+1}\,\lambda \tag{2.21}$$

The $J = 0$ state is exceptional, since it consists only of $N = 1$, that is $N = J + 1$. According to (2.17), its energy can derived from the expression $c$ with $J = 0$.

With $a$, $b$, $c$, and $d$ as defined above, the energy eigenvalues can be derived to

$$E(F_2) = b \tag{2.22}$$

$$E(F_{1,3}) = \frac{1}{2}\,(a+c) \pm \frac{1}{2}\,\left[(a-c)^2 + 4\,d^2\right]^{\frac{1}{2}}. \tag{2.23}$$

The three values are commonly signified as $F_1$ for $N = J - 1$, $F_2$ for $N = J$, and $F_3$ for $N = J + 1$. A mixing between $F_1$ and $F_3$ components may occur depending on the value of $\lambda$ due to the off-diagonal element $d$ in (2.17).

If $|\lambda| << 4BJ$, the energy eigenvalues are well expressed by Hund's case (b) limit. The energy levels of the triplets are narrowly spaced and the $F_1$ and $F_3$ levels are

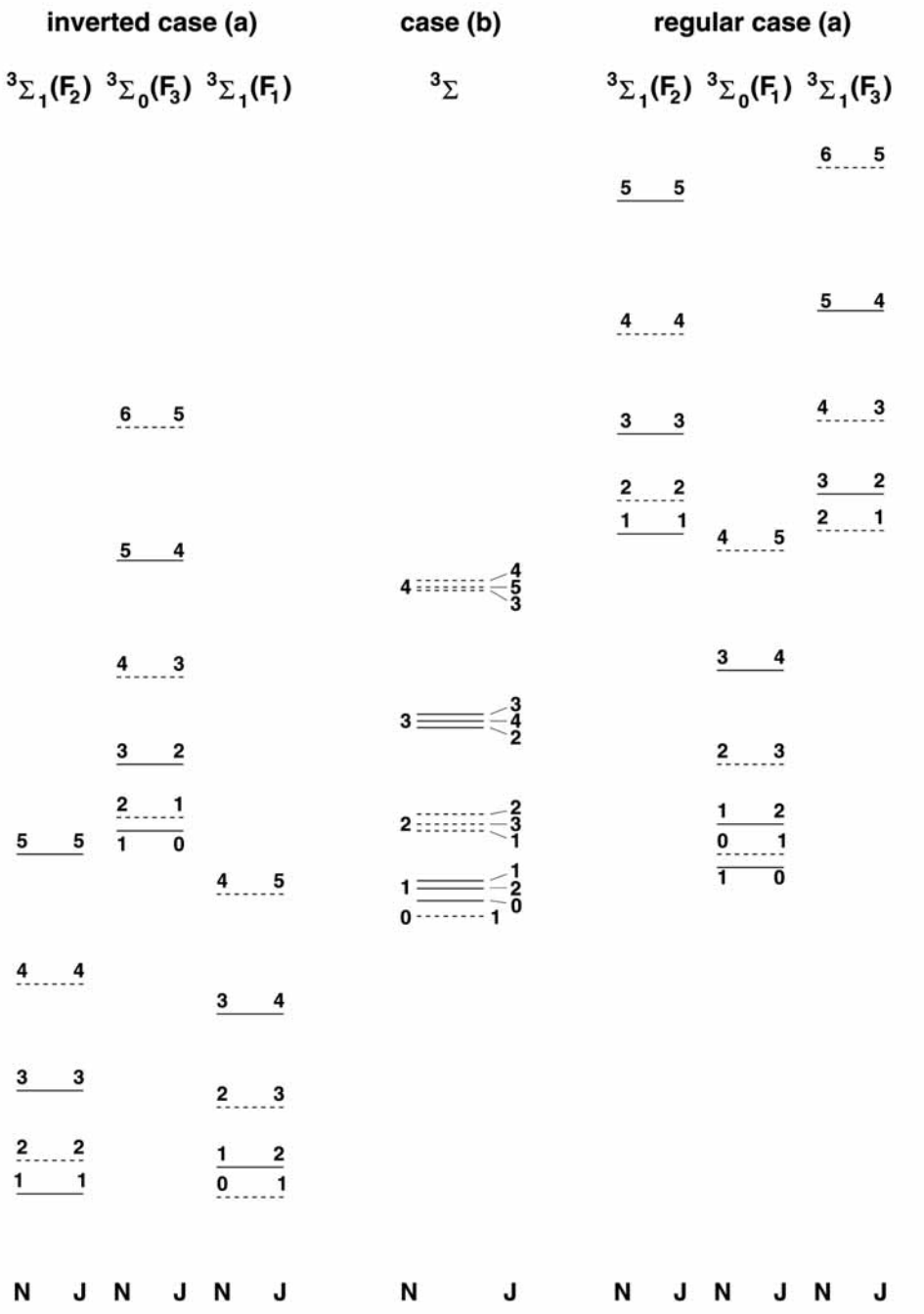


Figure 2.9: Energy level diagrams for different coupling schemes after [85]. Levels for both regular and inverted Hund's case (a) as well as case (b) are shown. In the inverted case (a) limit (left), the $F_1$ and $F_2$ components form the doubly degenerate $^3\Sigma_1$ state while the $F_3$ component together with the $J = 0$ are of the nondegenerate $^3\Sigma_0$ state. On the contrary, in regular case (a) limit (right), the $F_3$ component is degenerated with $F_2$ and the $^3\Sigma_0$ state is formed by the $F_1$ component. Note, that in this case the $J = 0$ level belongs to the $^3\Sigma_0$, too. For completeness reason, levels forbidden by nuclear spin statistics for the even-numbered clusters are indicated by broken lines.

slightly mixed. In this case, the same $N$ values indicate levels composing a triplet. The resulting energy levels are displayed amongst others in Figure 2.9.

For $|\lambda| >> 4BJ$, the mixing between the wavefunctions of the $F_1$ and $F_3$ levels is significantly stronger. The associated energies are best represented in Hund's case (a) limit. Because $N$ is not a good quantum number anymore within this limit, usage of the case (a) quantum numbers $J$ and $\Omega$ is more suitable[6]. The eigenvalues are thus commonly referenced as ${}^3\Sigma_0$ and ${}^3\Sigma_1$ in the case (a) notation ${}^{2S+1}\Lambda_{|\Omega|}$.

Neglecting all terms except for those depending on $\lambda$, the eigenvalues can be approximated to

$$\epsilon(F_2) = \frac{2}{3}\lambda \tag{2.24}$$

and

$$\epsilon(F_{1,3}) = -\frac{1}{3}\lambda \pm |\lambda|. \tag{2.25}$$

For positive values of $\lambda$, the eigenvalues in 2.25 can be written as

$$\epsilon(F_3) = \frac{2}{3}\lambda \tag{2.26}$$

and

$$\epsilon(F_1) = -\frac{4}{3}\lambda, \tag{2.27}$$

respectively.

Thus, the energy levels $F_2$ and $F_3$ are degenerated. These components form the doubly degenerate ${}^3\Sigma_1$ state, while the $F_1$ level belongs to the nondegenerate ${}^3\Sigma_0$ state, as does the $J = 0$ level. The energy of the ${}^3\Sigma_0$ state is lower than that of ${}^3\Sigma_1$; it is common to call the splitting regular, then.

On the contrary, if $\lambda$ is negative, the eigenvalues can be derived to

$$\epsilon(F_3) = -\frac{4}{3}\lambda \tag{2.28}$$

$$\epsilon(F_1) = \frac{2}{3}\lambda. \tag{2.29}$$

[6] In general, $\Omega$ denotes the sum of the projections of the angular momentum $\mathbf{L}$ and the spin $\mathbf{S}$, that is $\Omega = \Lambda + \Sigma$. In the present case, without an angular momentum, $\Omega$ corresponds to the projection of the spin on the molecular axis.

Here, the energy level of $F_1$ is degenerate with that of $F_2$, both representing the $^3\Sigma_1$ state. Correspondingly, the $^3\Sigma_0$ consists of $F_3$ together with the $J = 0$ level. Since the energy of the $^3\Sigma_0$ level is higher than that of $^3\Sigma_1$, the splitting is called inverted.

The energy levels for inverted as well as regular Hund's case (a) are also included in Figure 2.9.

### Resulting spectra

Due to the different order of energy levels, the value of $\lambda$ has a crucial impact on the appearance of absorption spectra. For an energy level sequence according to case (b) limit, each absorption feature will be splitted into three lines. With increasing value of $\lambda$ the triplet splitting approaches the dimension of the rotational splitting. As a consequence, absorption lines originating from the same triplet, that is same $N$, may be significantly separated. To be precise, one spin component will be shifted versus the others either to lower or higher frequencies depending on whether the energies are represented according to regular or inverted case (a) (see Figure 2.9).

Additionally, in the vibrational ground state even $J$ values are forbidden due to spin statistics following the argumentation in section 2.2.1. In the upper level, the situation is reversed, of course. Figure 2.10 shows the involved energy levels for a fundamental antisymmetric stretching mode in consideration of spin statistics in the inverted case (a) limit. Only the first *P*- and *R*-branch transitions, $\Delta N = \pm 1$, are depicted, although, in principle, *Q*-branch transitions are possible, albeit with significantly weaker intensity. The corresponding transition moments have been calculated by Tatum & Watson [85].

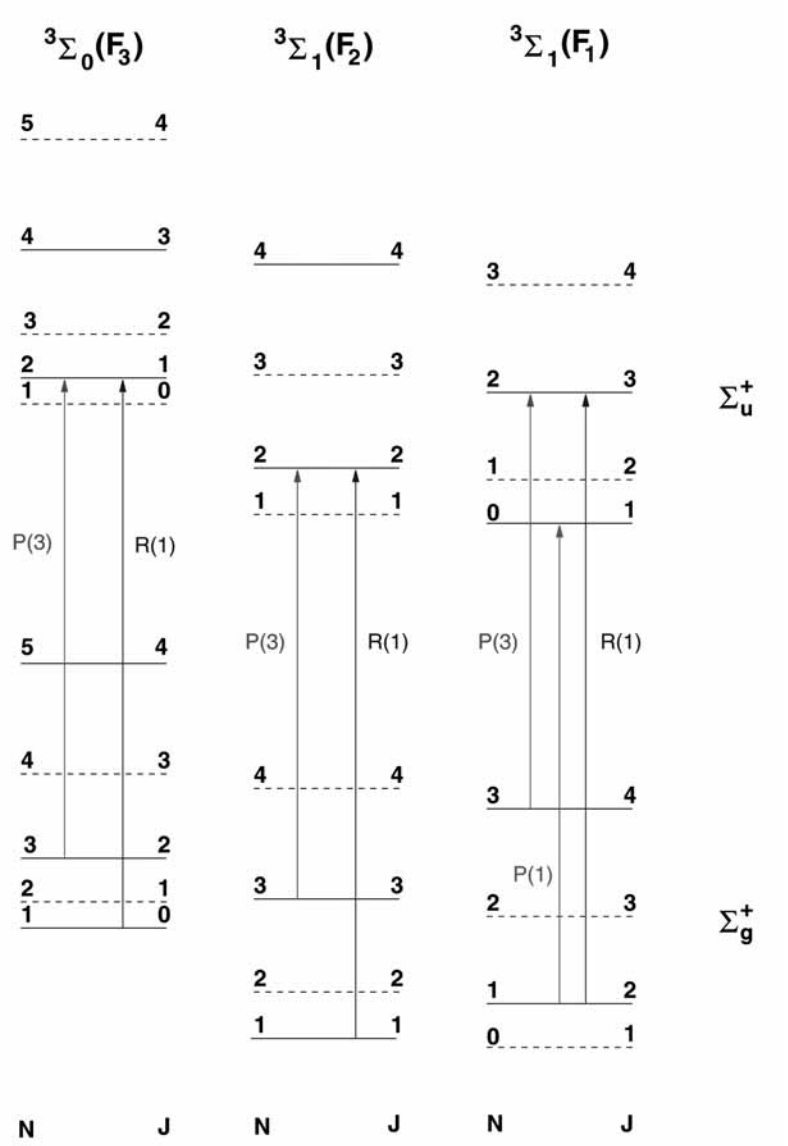


Figure 2.10: Energy level scheme for even-numbered carbon chains within inverted Hund's case (a) limit: levels missing due to spin statistics are indicated with broken lines. The three components belonging to the *R(1)* and the *P(3)* transition, respectively, are denoted with arrows. Note, that only the $F_1$ component contributes to the *P(1)* transition.

# 3

# Experimental Setup

The experimental difficulties in probing carbon clusters are usually the efficient production of the transient species as well as their sensitive detection. The measurements carried out in the course of this thesis have been performed with the Cologne carbon cluster experiment (CCCE), which combines a laser ablation source with a high resolution tunable infrared diode laser spectrometer. Both units as well as the measuring mode will be described in detail in the following chapter.

The original setup, described in [6], had to be modified due to a insufficient signal-to-noise ratio with respect to weak absorption signals like hot band transitions. Thus, several mechanical and optical devices have been replaced. These rearrangements are emphasised in each section. The last section is dedicated to the result of these improvements.

## 3.1 Cluster Sources

In order to produce sufficient amounts of such reactive species as carbon clusters, two major principles have been proven to be of high efficiency. The first one is the ablation of material, e.g. graphite, by a high power laser, the second one is the discharge of an appropriate precursor gas. Both production methods can be combined with an adiabatic expansion into a vacuum chamber leading to a supersonic jet. Thus, the produced molecules are available at rather low rotational temperatures.

Discharge sources are widely known for their effective production of hydrocarbons or cyanides as well as their spectroscopic versatility. The work of Linnartz and co-workers has shown that pure carbon chains can also be generated within discharge sources and detected by their optical spectrum in the resulting supersonic jet [57, 66]. Appropriate precursor gases to produce pure carbon clusters

are acetylene ($C_2H_2$), ethylene ($C_2H_4$), allene ($C_3H_4$) or mixtures of these gases[7].

It is easily accepted, that this type of source is not optimal for the spectroscopic investigation of bare carbon clusters. The many possible byproducts are likely to have a negative impact on measurements of pure clusters by causing either blending of absorption lines or reduction of the production rate. Thus, a laser ablation source was employed in the CCCE.

The most famous examples for the production of pure carbon clusters via laser vaporisation of graphite are the experiments on the $C_{60}$ fullerene specified by Kroto, Curl, Smalley *et al.* [54]. The operational mode of the ablation source described in the following section corresponds to that of the classic Smalley source, even though important improvements have been made over many years to adapt this technique to laser spectroscopical needs leading to a highly effective production of these molecules [46, 88].

### 3.1.1 The Laser Ablation Source

At room temperature and normal pressure, graphite is in its solid phase and temperatures of 4000 K are needed to evaporate it [53, 74]. Such temperatures can be reached by high energy laser pulses. The threshold laser energy to vaporise rather than liquefy the graphite is roughly $10^8$ W$/$cm$^2$ [41]. Beyond this threshold value, a plasma develops on the graphite surface.

Figure 3.1 shows the design of the ablation source used in the Cologne carbon cluster experiment.

Usually, graphite rods, consisting of more than 99.5 percent of the isotope $^{12}$C, are used in this cluster source. A density of 2.25 g$/$cm$^3$ is granted by the distributor Goodfellow/Cambridge. The best ablation conditions are achieved by rotating the rod slowly but constantly, otherwise, the laser pulses burn holes into the graphite.

The high energy laser pulses are delivered by an excimer laser (LPX 200, Lambda Physics) operating at a wavelength of 248 nm due to the filling with KrF. This laser only works in a pulsed mode with a maximum repetition rate of 50 Hz. Pulse energies of up to 500 mJ with a pulse length of roughly 25 ns are possible. However, the laser is run with lower energies during the measurements, since, according to experience, energies higher than 100 to 150 mJ per pulse do not yield a significantly higher amount of large clusters.

The laser beam is focused via a $MgF_2$ lens onto the carbon rod. In the focus, the spot size is about $3 \times 0.5$ mm$^2$ reproducing the laser's square beam profile leading to energy densities in the order of $10^8$ W$/$cm$^2$ on the surface of the rod, thus meeting the threshold limit for evaporating the graphite.

Considering the evaporation heat of graphite ($\lambda = 716.9$ kJ$/$mol [74]), the maximum number of ablated particles can be estimated to $1.2 \times 10^{17}$ per pulse, if the

[7] Discharges of these gases have been successfully used to produce small carbon clusters like linear $C_5$ in experiments without the subsequent expansion in the 1980's (e.g. [62]).

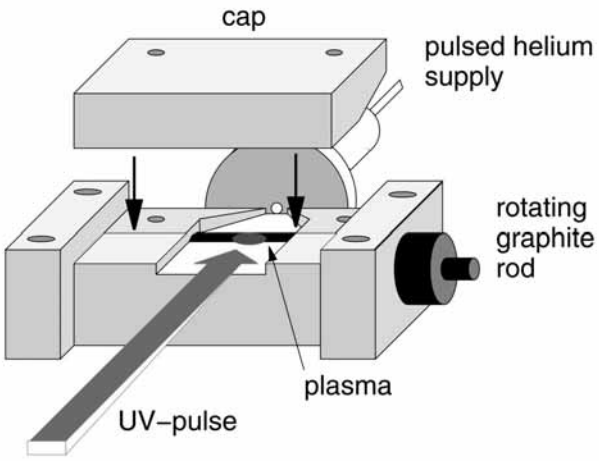


Figure 3.1: Design of the laser ablation source [20]. Both the body and the removable cap are made of stainless steel. A nozzle is attached to the back side allowing for pulsed buffer gas supply. The graphite rod is driven by the rotation of a DC geared motor, which is not shown in the scheme. To simplify matters, the second geared motor permitting additional axial translation of the rod is also not shown.

laser power is totally absorbed during the evaporation. Investigations in the field of materials science show a value of 30 to 50 ng carbon for the total amount of material ablated per pulse in this type of ablation source [3]. This corresponds to a number of roughly $1.5 \times 10^{15}$ carbon atoms.

The actual source has already been described in detail elsewhere [20, 90]. It consists of stainless steel and the dimensions are about 47 mm $\times$ 22 mm $\times$ 33 mm. As can be seen in figure 3.1, the cap can be removed to clean the source from soot which is produced during the operation. The gas inlet at the rear side measures $2 \times 2$ mm$^2$. A nozzle (General Valve, Pulsed 9 Series) is attached to this side, making a pulsed inflow of buffer gas possible. The source's outlet is a small slit with a cross section of 12 mm $\times$ 0.9 mm. The length of this reaction channel is about 8 mm. The excimer laser enters the source through this slit.

Figure 3.2 illustrates the laser ablation by giving a side view of the source. Carbon atoms ablated during the excimer pulse are carried out by the buffer gas pulse, in this case helium at a pressure of up to 20 bar. The formation of the different clusters takes place in the reaction channel where the carbon atoms from the hot and dense plasma build chains and perhaps even rings due to collisions. After traversing the channel the cluster gas expands adiabatically into a vacuum chamber where the background pressure is kept around 0.1 mbar.

Figures 3.3 and 3.4 show the resulting supersonic jet. As the clusters are electronically excited, the jet is gleaming, visualising a narrow disc perpendicular to the slit. Figure 3.5 shows the velocity components of an expanding gas through a slit and a circular orifice to illustrate the occurrence of the observed disc. After a slit expansion, the velocity components have only minor portions perpendicular to

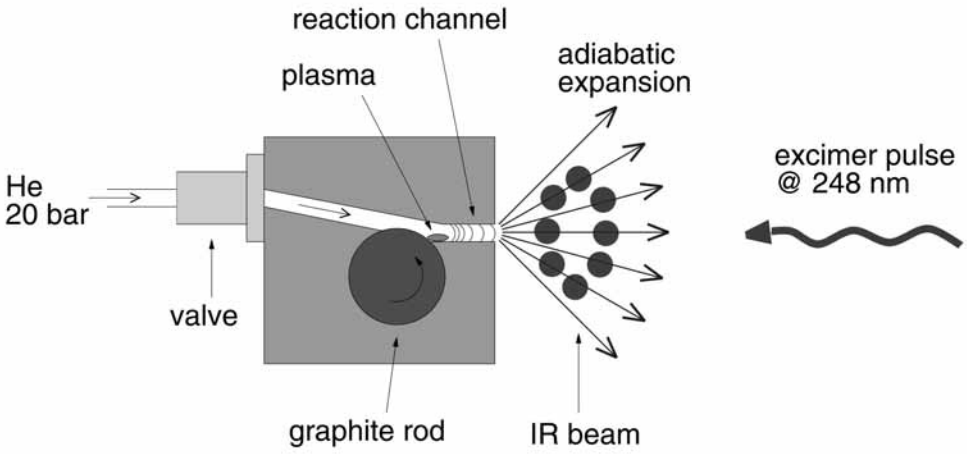


Figure 3.2: Schematical view of the laser ablation process [20]. A pulsed excimer laser beam is focused onto the rotating graphite rod. As a result, single carbon atoms are ablated, generating a dense plasma. They are flushed out by pulses of He gas. On their way through the reaction channel, the atoms form clusters due to collisions. Subsequently, the cluster gas expands adiabatically into a vacuum chamber, where the clusters are probed by the IR beam, which is indicated by the elliptical beam pattern.

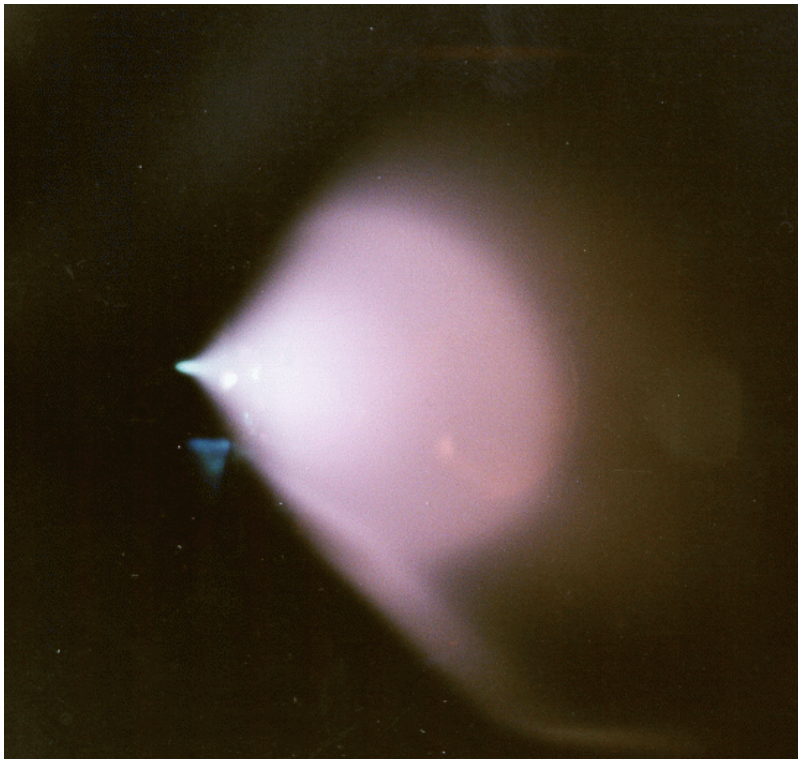

Figure 3.3: Side view of the carbon cluster jet [6]: the dimensions are about 17 cm $\times$ 17 cm.

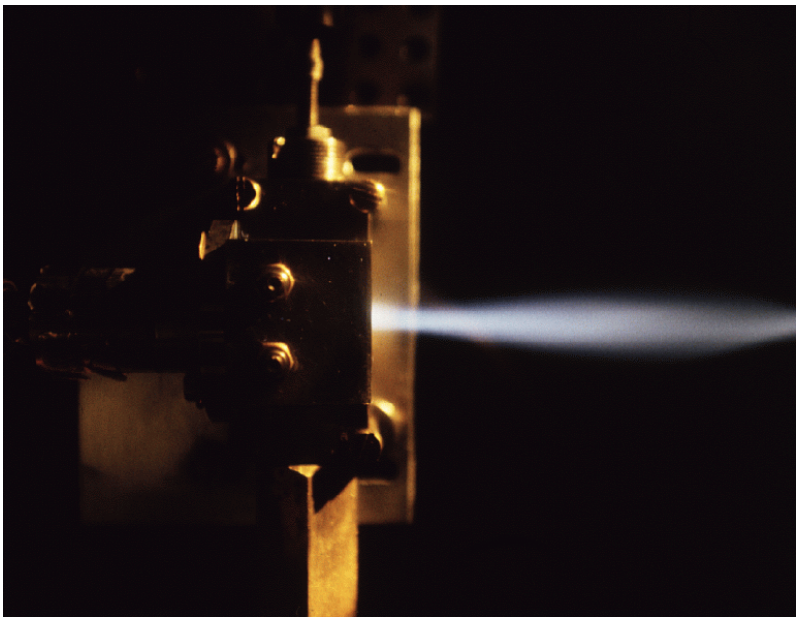

Figure 3.4: Top view of the cluster jet [6]: the maximum width of the jet is roughly 2 cm.

the direction of propagation. As a result, observed absorption lines exhibit almost no Doppler broadening if a slit expansion is employed.

Within the bright area of this disc all molecules have the same supersonic velocity. Thus, this area is called the zone of silence as the number of collisions is strongly reduced. It is clear, that this is the relevant area for probing the molecules by means of high resolution spectroscopy.

The geometry of the reaction channel has proven to be crucial for an effective cluster formation (e.g. [46, 88]). Apparently the length of the slit influences the carbon cluster production due to higher collision probabilities in a longer channel. Unfortunately, if the channel is chosen too long, the jet will collapse. For the spectroscopic investigation of the clusters it is necessary to probe as many molecules as possible requiring a rather expanded molecular jet more than a collimated molecular beam (see figure 3.2). Besides, as has been derived from figure 3.5, employing a slit nozzle rather than a circular orifice reduces Doppler broadening of lines. The reaction channel used in this setup constitutes a kind of compromise partially fulfilling all requirements.

The rotational temperatures inside the jet can be estimated to about 10 to 20 K (see section 4.2), while the plasma has an estimated temperature of several thousand K. The time scale of the cooling process is only a few $\mu$s. Thus, the timing between the gas inflow and the excimer trigger is a critical parameter in the cluster production. Both the UV laser and the valve are triggered by the same pulse generator. The trigger for the excimer is delayed to that of the valve by 760 to 780 $\mu$s depending on the experimental conditions.

Measurements carried out to characterise this type of ablation source revealed a total number of clusters in each laser pulse of $10^{13}$ to $10^{14}$ particles [20]. In principle, clusters of all sizes are produced at the same time but the measure-

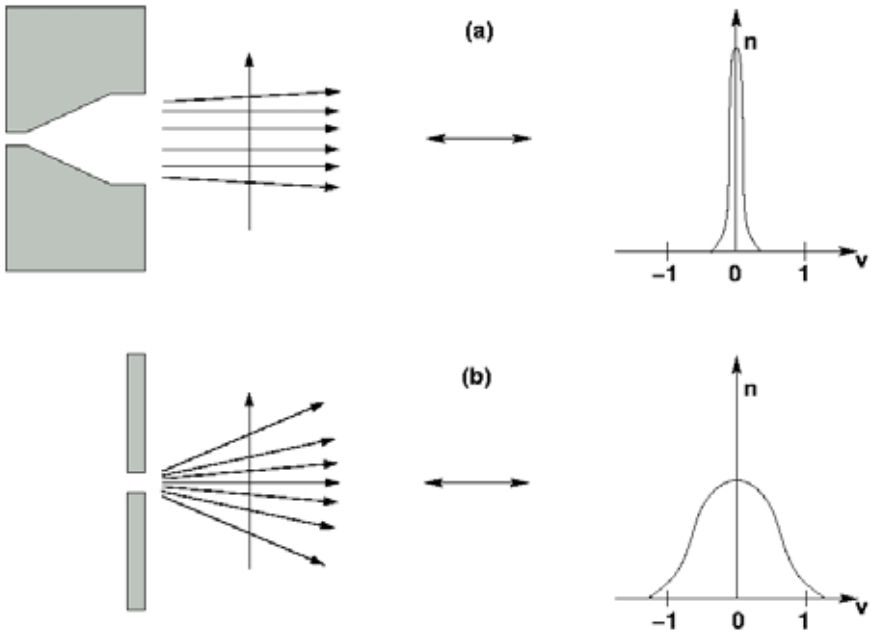


Figure 3.5: The velocity components of gas expanding through a slit nozzle are strongly oriented along the axis of propagation (a). They show only minor portions perpendicular to this axis. On the contrary, if the gas is expanded through a short circular orifice (b), the velocity distribution is substantially broader.

ments mentioned above indicate a ratio of 230:55:1 for the pure carbon clusters $C_3$:$C_9$:$C_{13}$. The actual ratio depends heavily on the experimental conditions, but small clusters are more likely to be formed than larger ones. $C_{13}$ is so far the longest carbon cluster for which rotationally resolved measurements have been successfully accomplished [25]. For the two clusters investigated in the course of this work, $C_7$ and $C_8$, it appeared that $C_7$ was produced in much higher abundances although their production conditions were quite comparable (Table 3.1)[8]. However, producing a sufficient amount of $C_8$ molecules turned out to be more difficult.

Clusters of different sizes leave the source at different times. Since all clusters have the same speed when leaving the reaction channel, this time difference is likely to result from the building mechanisms inside. In general, the higher the background pressure the earlier a specific cluster is observable. For $C_8$, time differences of up to 5 $\mu$s emerged from slight differences in the pressure gradient between background and vacuum chamber. Regarding the time in which a certain species is observable, a significant difference was perceivable for $C_7$ and $C_8$. The first molecule ocurred in a time frame of roughly 10 to 15 $\mu$s while the latter showed only 5 $\mu$s of interaction time with the probing infrared beam. For this reason, a time resolved measuring mode was required which is described later in section 3.3.

For the new setup, an improved source mounting was designed and built by the

[8]Further parameters like the exact position of the $MgF_2$ lense or the angle between the UV laser and the graphite rod could not be quantified but may be important, too.

Table 3.1: Optimised production conditions for $C_7$ and $C_8$. The timing for the first boxcar is given with reference to the excimer trigger (see section 3.3). Values varied depending on e.g. the freshness of the KrF filling or the actual duration of a measurement.

| | $C_7$ | $C_8$ |
|---|---|---|
| Energy per pulse [mJ] | 100 - 150 | 100 - 130 |
| Backing pressure [bar] | 17-20 | 17-20 |
| Chamber pressure [$10^{-1}$ mbar] | 0.98 – 1.2 | 0.88 – 1.1 |
| First boxcar [$\mu$s] | 16-20 | 18-20 |

Table 3.2: Comparison of production conditions with different types of vaporisation lasers. Values for the energy densities are derived by taking the energy per pulse divided by pulse duration and size of the laser spot in the focus.

| | Excimer | Nd:YAG |
|---|---|---|
| Wavelength [nm] | 248 | 266 |
| Energy per pulse [mJ] | 100 - 150 | 20 - 30 |
| Pulse length [ns] | 25 | 7 |
| Repetition rate [Hz] | 50 | 11 |
| Spot size in focus [mm$^2$] | 1.5 | 0.785 |
| Energy density $\left[10^8 \frac{\mathrm{W}}{\mathrm{cm}^2}\right]$ | 2.7 - 4 | 3.64 - 5.46 |

mechanics workshop. After applying a second motor and an eccentric tappet to this new mount both rotation and translation of the carbon rod are possible. The old stepping motor was replaced by DC geared motors. Generally, the translation movement is not carried out during measurements, due to a considerable formation of dust. Nevertheless, the translation enables to always expose a ‘fresh‘ part of the surface to the excimer laser light during operation. The combination of all items have resulted in a very steadily running jet.

During the work on $C_7$, the opportunity arose to test a Nd:YAG laser system as vaporisation laser. The used laser was an Inlite system provided by Continuum operating at 266 nm. This laser had a maximum repetition rate of 20 Hz but was operated at 10 to 11 Hz in the tests. Both lasers are compared in Table 3.2. It appears, that, due to a smaller pulse duration and a smaller beam section in the focus, pulse energies of 20 to 30 mJ delivered by the YAG are sufficient to yield the same results as gained with the excimer. This impression was certified by measurements of the same absorption line of $C_7$ for both ablation processes.

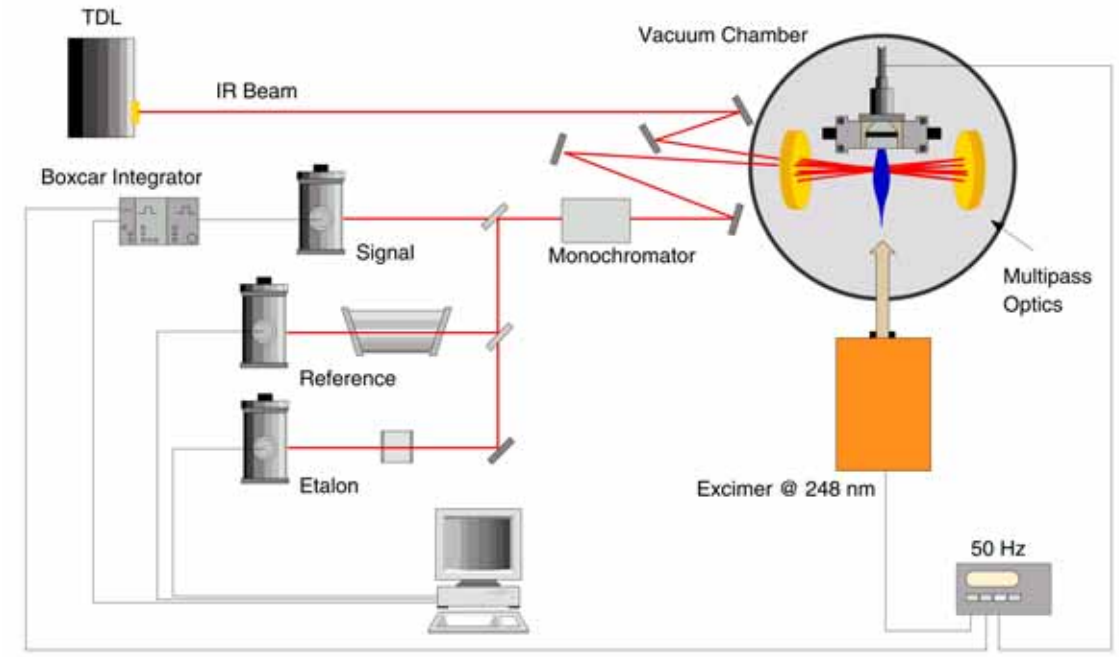


Figure 3.6: Schematical overview of the Cologne carbon cluster experiment (after [21]): An IR laser beam probes the carbon cluster supersonic jet roughly 10 mm downstream from the nozzle. An increase of the sensivity is achieved by employing multipass optics. A monochromator is applied to the optical path whenever necessary. About 10 percent of the infrared beam is split off for frequency calibration. Signal, reference, and etalon beams are focused on InSb detectors.

## 3.2 The Cologne Carbon Cluster Experiment

Figure 3.6 shows the experimental setup. The infrared beam of a tunable diode laser is guided through a vacuum chamber probing the cluster gas produced by the source described above. A multipass Herriott cell is used to increase the sensitivity by enhancing the absorption path length in the chamber. The outcoming signal is focused on an InSb detector. Part of the beam is used for frequency calibration by simultaneously recording the spectrum of a reference gas as well as an etalon. The visible beam of a HeNe laser can be applied to the optical path to prealign the optics.

To guarantee an optimal optical path, almost every mirror mount of the old setup was replaced. The new mirror mounts[9] are more stable with respect to mechanical vibrations. Furthermore, they are smaller and more convenient to handle.

[9] purchased from Radiant Dyes

### 3.2.1 The Infrared Laser

Tunable lead salt diode lasers cooled by liquid nitrogen serve as radiation sources for the experiment. These lasers are available in the range of 3.1 to 10 $\mu$m which corresponds to a frequency range from 1000 to 3250 cm$^{-1}$ [55]. During operation, each diode can be tuned in frequency by changing temperature and laser current. The overall tunability of a single diode is typically between 5 and 12 cm$^{-1}$, as the temperature range for each diode is limited to just a few K. Depending on further specifications, single mode performance with mode lengths of 3 cm$^{-1}$ and more can be provided by the distributor Laser Components. Each diode has a guaranteed radiation power of 0.1 mW, but higher power values like 0.5 mW and more can be delivered on demand. The line width is typically specified with 20 MHz (0.00067 cm$^{-1}$). For at least one of the diodes used in the course of this work the line width could be estimated to be in the order of 100 MHz (0.0033 cm$^{-1}$) and therewith significantly larger.

All laser diodes used were nearly single mode. But despite the good quality of the diodes, a monochromator was applied to the optical path (see figure 3.6), since the supersonic jet emits not only in the visible but also in the infrared region. Whenever possible, the monochromator was not included in the setup to avoid problems with astigmatism.

The types of diodes used formerly were tunable over 50 to 100 cm$^{-1}$ all in all. But they had to be cooled in a closed helium cycle, and inside the mandatory cryogenic cold heads the laser diodes were exposed to massive vibrations during operation. Those vibrations had significant influence on the overall signal-to-noise ratio of any measured spectrum. Thus, it was necessary to pass on the wide tunability for the benefit of an improved signal-to-noise ratio.

### 3.2.2 The Multipass Cell

A Herriott type multipass cell [39] is used to extend the absorption path length. Figure 3.7 shows the scheme of the Herriott cell applied to the jet. The infrared beam enters the first mirror off-axis through a hole. After several reflexions the beam returns to its entrance point having exactly the same Gaussian' and geometric parameters it had when entering the mirror system. During the whole path the beam lies on the surface of a hyperboloid leading to an elliptical pattern of reflexion spots on the mirrors.

To calculate the resulting pattern, one can use matrix methods from geometrical optics leading to the following equation [24]:

$$n\,\Phi = 2\,\pi\,k \qquad \text{with} \quad k = 1, 2, \cdots, n. \tag{3.1}$$

Here, $\Phi$ means the angle between any two consecutive reflexes on one mirror. The beam leaves the system after $n$ reflexions per mirror (means $2n$ passes).

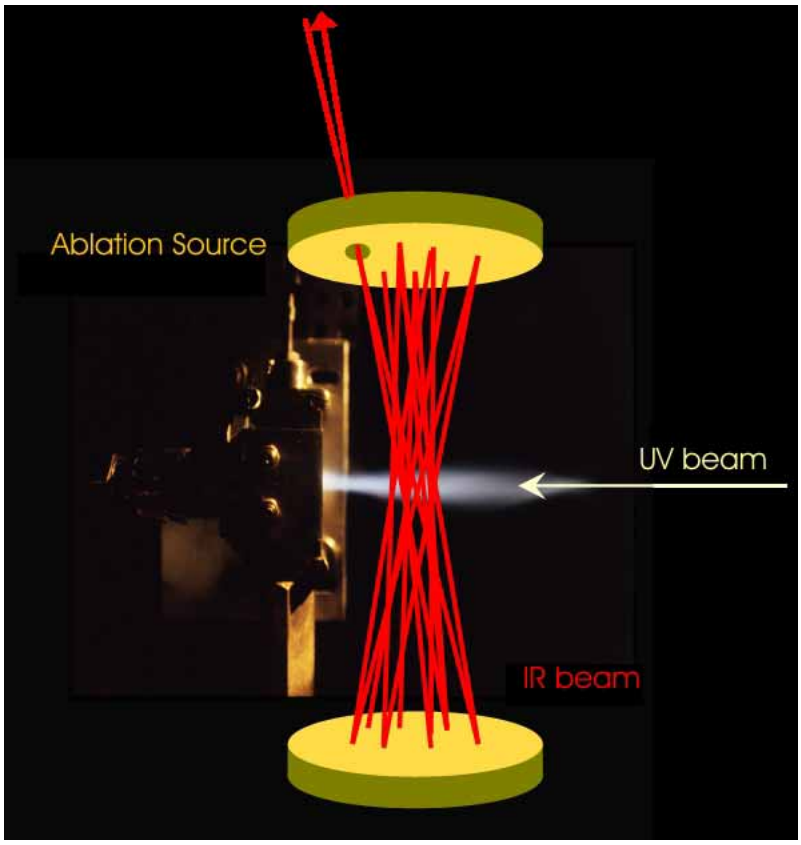


Figure 3.7: Scheme of the optical path within the vacuum chamber: the infrared beam is reflected several times at the two mirrors forming the Herriott cell. All beams are drawn with a constant diameter neglecting the Gaussian' parameters. The smallest part of the resulting pattern lies midway between the two mirrors where the IR beam intersects the jet.

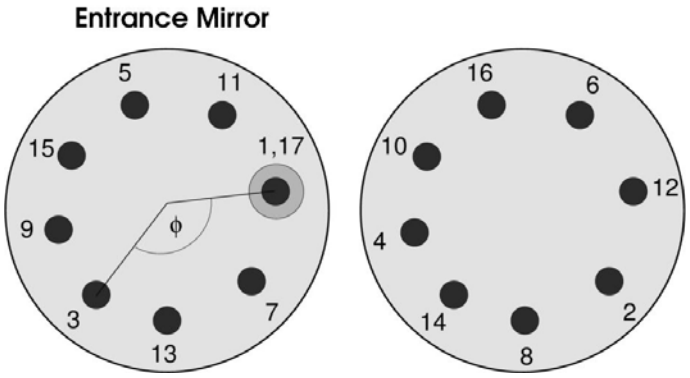


Figure 3.8: Schematical distribution of the reflexion spots in a Herriott cell for 8 reflexions (16 passes) and $\Phi \simeq 135°$. The counting of the reflexes starts when the beam enters through the hole. The special case of a cyclic pattern is shown.

Equation 3.1 gives a value of $n$ = 8 for an angle $\Phi \simeq 135°$. The resulting pattern is shown schematically in figure 3.8.

The number of reflexions per mirror depends only on the distance $d$ and the focal length $f$ of the mirrors[10]:

$$\frac{d}{f} = 2\left[1 - \cos\left(\frac{\Phi}{2}\right)\right] \tag{3.2}$$

In the Cologne carbon cluster experiment, two spherical mirrors with a diameter of 5 cm and a focal length of 6.5 cm form the multipass cell. The hole in the entrance mirror is 3.5 mm in diameter and placed 5 mm away from the center. Both mirrors are coated with gold and a second special coating made of yttrium oxide ($Y_2O_3$) allowing for cleaning the mirrors from soot.

Due to the dimensions of the ablation source, the relation $\frac{d}{f}$ has to be in the order of 3. Usually the cell is aligned to have 21, 24 or 27 reflexes per mirror meaning 42, 48 or 54 passes through the jet. Table 3.3 gives the values for $\Phi$ and $\frac{d}{f}$ obtained with equations 3.1 and 3.2. The actual number of passes was adapted to the experimental conditions like output power of the IR laser diode or abundances of the investigated molecules.

Table 3.3: Parameters for the Herriott cell

| $n$ | $k$ | $\Phi$ [°] | $\frac{d}{f}$ | $d$ [cm] |
|---|---|---|---|---|
| 21 | 15 | 257.14 | 3.25 | 21.13 |
| 24 | 17 | 255.00 | 3.22 | 20.93 |
| 27 | 19 | 253.33 | 3.19 | 20.74 |

[10]Assuming both mirrors have the same focal length $f$.

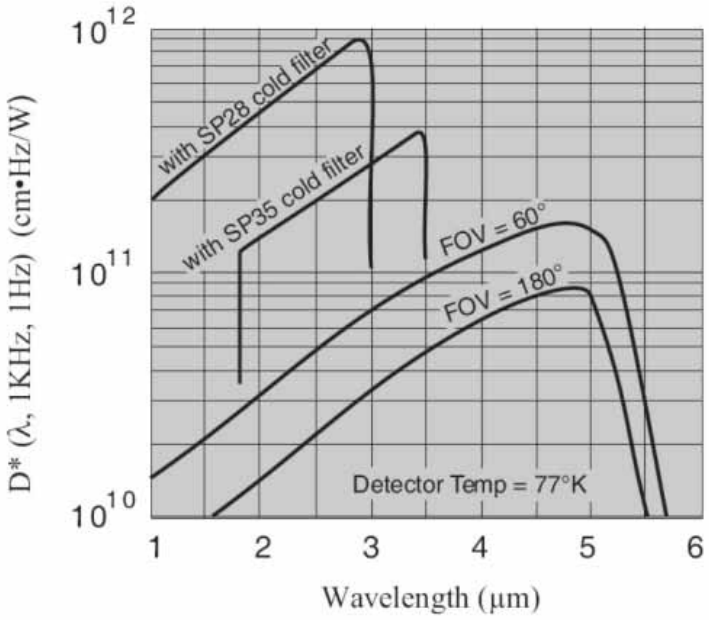


Figure 3.9: Detectivity versus wavelength for J10D series InSb detectors [47]: best results are achieved between 4.5 and 5 $\mu$m. Only detectors with a field of view (FOV) of 60° have been used in the setup.

### 3.2.3 The InSb Detector

To detect the signals, two types of detectors are available, indium antimonide (InSb) and mercury cadmium telluride (HgCdTe). However, in the frequency range from 1 to 5.5 $\mu$m, InSb detectors are prefered due to their higher sensitivity [47]. They are photovoltaic and generate a current proportional to the infrared radiation power. Figure 3.9 shows the so-called detectivity $D^*$, which is a measure for the detector's quality, depending on the wavelength. As can be taken from figure 3.9, the best performance is achieved in the 4.5 to 5 $\mu$m region (2222 to 2000 cm$^{-1}$), which was the region of interest within the scope of this work.

Due to the transient nature of the investigated molecules, the bandwidth of the preamplifiers, at least for the signal detector, was chosen to be as high as possible. The preamplifier for the signal detector exhibits a bandwidth of up to 900 kHz (ac-coupled) which is sufficient for a time-resolved detection of signals occuring on a 10 to 20 $\mu$s scale.

## 3.3 Measuring Mode

Due to the pulsed character of the jet, the carbon clusters produced are only observable within a small time frame, which corresponds to the time in which the produced clusters intersect the probing infrared beam. This time frame is

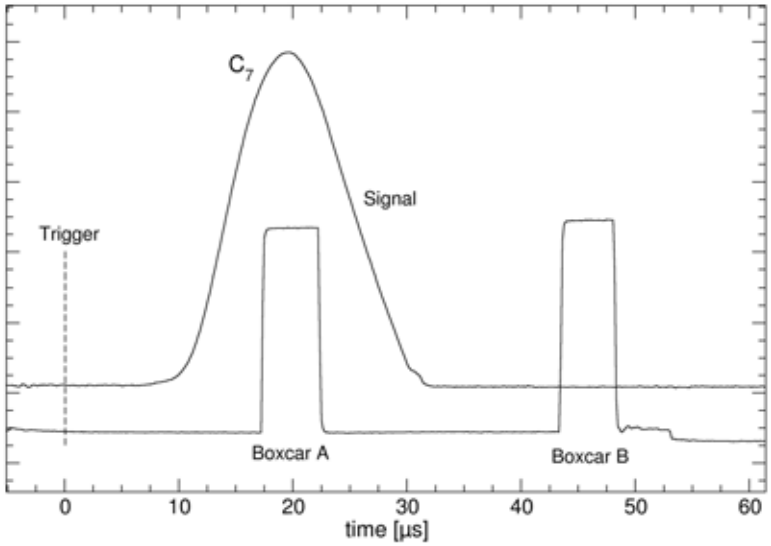


Figure 3.10: Timing scheme to illustrate the measuring mode: roughly 15 to 25 $\mu$s after the excimer pulse was fired (Trigger) the clusters are probed by the IR beam. The first boxcar (A) is set to the absorption, the second one (B) some 10 $\mu$s later. Subtraction of both integrated signals result in a reduced base line influence. The displayed strong absorption feature belongs to the *P*-branch of the $\nu_4$ fundamental of $C_7$ around 2137 cm$^{-1}$.

measured to be on the order of 10 $\mu$s. A pair of gated boxcar integrators, also triggered at 50 Hz by the pulse generator, is applied allowing for a time resolved detection. They are used to set a starting point for the signal integration within a selected time interval. The first boxcar is set to the cluster absorption signal, the second one to a time some 10 $\mu$s later. Both signals are averaged 30 to 100 times and subsequently subtracted to minimise base line effects originating from the diode laser. The resulting signals are fed into a computer via an ADC card.

The actual values of the boxcar timing (delay and width) are usually optimised by simultaneously displaying the output from the detector and the boxcar gates on an oscilloscope. By holding the laser frequency at the absorption maximum of a strong transition, the gates can be positioned easily. Figure 3.10 shows a screen shot of the oscilloscope. Since the oscilloscope gets the same trigger as the excimer laser, it can be taken from Figure 3.10 that the cluster absorption occurs 15-25 $\mu$s after the excimer pulse.

As already mentioned in section 3.1.1, clusters of different sizes leave the ablation source at different times. Thus, absorption signals arising from small clusters occur slightly earlier (5-10 $\mu$s) than those caused by larger ones. By properly adjusting the first integrator with respect to the flight times, different clusters should be measurable separately even if some of their absorption frequencies happen to coincide. However, for the measurements performed in the course of this work, some absorption lines of $C_3$ could not be eliminated from the spectrum by setting

the first boxcar to the later occuring absorption of $C_7$ or $C_8$, respectively . This is probably caused by the highly effective production of $C_3$ with the new source setup.

To perform a scan, the tunable diode laser is tuned slowly by ramping the laser current in small steps. The tuning rate for each diode laser is different, but a value of 0.026 $cm^{-1}$/mA was determined for the diode used in the $C_7$ measurements. The velocity of the ramping process is usually set to 0.02-0.03 mA/s to allow scanning 1 $cm^{-1}$ in approximately 30 min.

The software recording the data was written by G. Fuchs within the scope of his PhD thesis [21]. It is based on the in-house programme *dada* as programming language and converts the data into ascii format.

## 3.4 Calibration

Absolute and relative frequency calibrations are performed by splitting off part of the diode laser beam (roughly 10 percent) and simultaneously recording both the absorption spectrum of a reference gas and the fringe spectrum of a germanium etalon. To record the spectra, both the reference and the etalon beam are periodically chopped at about 3 kHz and the detected signals are processed with two lock-in amplifiers before being stored in the computer. $N_2O$ and OCS served as reference gases depending on the wavelength region. The etalon used has a free spectral range (FSR) of approximately 0.0157 $cm^{-1}$ ($\approx$ 500 MHz).

The data obtained during one frequency scan are calibrated with the software *calib* introduced in [21], which is also based on the programme code *dada*. The calibration accuracy is usually better than 0.002 $cm^{-1}$.

## 3.5 Sensitivity Considerations

The new experimental setup was tested with measurements on the antisymmetric stretching mode $\nu_5$ of the $C_8$ molecule at around 2068 $cm^{-1}$. This project was chosen as test candidate mainly for two reasons. First, every single parameter necessary for a successful detection of carbon clusters had changed in the new system. With all production and detection parameters changed, at least the frequency region of a possible cluster absorption should be known. The second reason is a more spectroscopic one. The aforementioned rovibrational band was one of the last measured with the old setup [6]. Since these measurements exhibited a rather poor signal-to-noise ratio (SNR) the analysis of this band was severely hampered. A remeasurement of this band was necessary for a reliable analysis, hence.

Figure 3.11 shows a part of the *R*-branch of the $C_8$ rovibrational spectrum measured with the old (lower) and the new system (upper). Both spectra are scaled

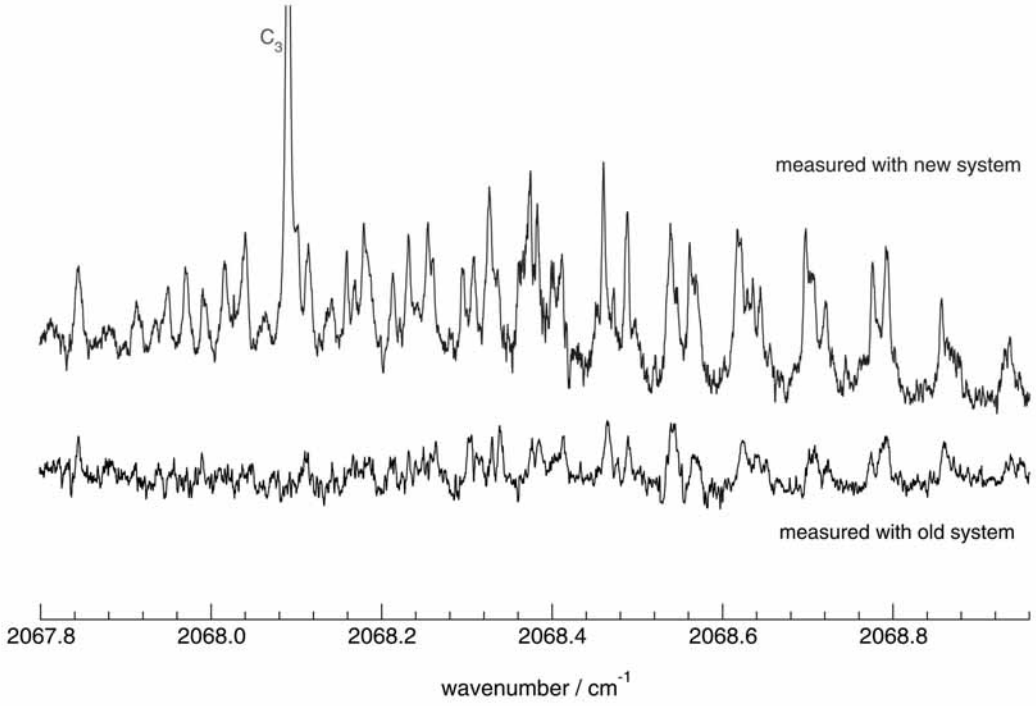


Figure 3.11: Comparison between the *R*-branch of the $\nu_5$ of $C_8$ measured with the old as well as the new system. Both spectra are scaled to the same noise level making the significantly improved signal-to-noise ratio evident. Due to a highly increased production rate, the $C_3$ peak could not be eliminated by using the boxcars.

to the same noise level. Even if one takes into account possible differences in the mode profile of the two lasers used, this picture demonstrates the significant increase in the SNR very impressively. As a result, the measurements on $C_8$ performed with the new setup allow for a more reliable analysis, which will be discussed in the following chapter. In contrast to the old system, the peak originating from $C_3$ could not be eliminated by using the boxcars, most likely due to a highly increased production rate of $C_3$.

It is difficult to decide, which of the described experimental improvements contributes in what amount to the increased SNR. But it may be taken for granted that replacing the laser diodes had a decisive effect on the overall SNR.

The spectrometer's sensitivity can be derived from a simple estimation. According to experience, the maximum detectable intensity $I_0$ on the detector can be estimated to 6 V. The minimum detectable intensity is of the order of roughly 50 $\mu$V. Division of minimum and maximum intensity yields a detection sensitivity of $8.3 \times 10^{-6}$, which is a typical value for multi pass absorption spectrometers (e.g. [70]).

In order to determine the minimum number $n_{min}$ of cluster molecules necessary for detection, the Beer-Lambert law has to be taken into account. The exact

Table 3.4: Parameters for two *P*-branch transitions of the $\nu_5$ fundamental of $C_8$ ($N = J$, see chapter 4) as well as a weak transition of the $\nu_4 + \nu_{11} - \nu_{11}$ hot band of $C_7$ (see chapter 5) to estimate the minimum number of cluster molecules necessary for detection. The absorption path length $l$ was determined for $n_p$ = 48 passes through the jet with a diameter of 1 cm.

| transition | $\nu_0$ [cm$^{-1}$] | $\frac{I(\nu_0)}{I_0}$ | $\Delta\nu_D$ [cm$^{-1}$] | S $\left[\frac{\text{cm}^{-1}}{\text{molecule/cm}^2}\right]$ | l [cm] | $n_{min}$ |
|---|---|---|---|---|---|---|
| $C_8$, *P(11)* | 2067.4548 | $8.3 \times 10^{-6}$ | $2.39 \times 10^{-4}$ | $3.993 \times 10^{-18}$ | 48 | $6.470 \times 10^{11}$ |
| *P(27)* | 2066.7658 | $8.3 \times 10^{-6}$ | $2.39 \times 10^{-4}$ | $1.541 \times 10^{-18}$ | 48 | $1.677 \times 10^{12}$ |
| $C_7$, *P(40)* | 2135.1065 | $8.3 \times 10^{-6}$ | $2.64 \times 10^{-4}$ | $0.734 \times 10^{-18}$ | 48 | $3.888 \times 10^{12}$ |

formula is derived in appendix A. The result is given by:

$$n_{min} = -\frac{\ln\left(\frac{I(\nu_0)}{I_0}\right) \cdot \Delta\nu_D}{S \cdot \sqrt{\frac{\ln 2}{\pi}} \cdot l \cdot n_p}. \tag{3.3}$$

For a weak transition occuring at the frequency $\nu_0$, the ratio $\frac{I(\nu_0)}{I_0}$ corresponds roughly to the spectrometer's sensitivity. Thus, the number of the investigated molecules can be estimated if the line strength $S$ for this transition is known. $\Delta\nu_D$ marks the Doppler width (HWHM), which is given by equation (5) in appendix A. The absorption path length is denoted with $l$, and $n_p$ designates the number of passes.

Table 3.4 gives the necessary parameters to estimate $n_{min}$ for a strong and a weaker transition of $C_8$. Using H. Pickett's fitting routine [73], values for the line strength $S$ result from the prediction procedure during the fit. For this calculation the programme needs the temperature and the vibrational dipole moment as input parameters. In the present case, the temperature was estimated to 10 to 15 K and the dipole moments for $C_7$ and $C_8$ were determined to 0.7 and 0.51 Debye, respectively[11]. With equation (3.3) one derives $n_{min} \approx 6.5 \times 10^{11}$ for the rather strong transition and $n_{min} \approx 1.7 \times 10^{12}$ for the weaker one.

The same estimation was done for a weak transition of the $\nu_4 + \nu_{11} - \nu_{11}$ hot band of $C_7$. A value of nearly $3.9 \times 10^{12}$ molecules was derived.

[11] Dipole moments were derived from intensities for the corresponding vibrational modes calculated by Hutter *et al.* [44].

# 4

# Measurements on Linear $C_8$ – A Case of Spin Uncoupling

Linear $C_8$ has a $^3\Sigma_g^-$ electronic ground state, thus, effects of the molecule's resulting spin are expected to influence its infrared spectra. The analysis of the related chain molecules $C_4$, $C_6$, and $C_{10}$ revealed a remarkable fact: the absolute value of the spin-spin coupling constant $\lambda$ increases with increasing number of atoms in the chain [31, 46, 26]. This behaviour was also observed for the isoelectronic carbon chains $C_nO$ [69] and $SiC_n$ [61]. Figure 4.1 displays the abolute values for $\lambda$ depending on the number of $\pi$-electrons for even-numbered pure carbon chains $C_n$ as well as for even-numbered $C_nO$ and odd-numbered $SiC_n$ chains.

However, the increasing impact of spin-spin coupling with growing chain length and, therewith, growing distance of the uncoupled electron pairs, appears unreasonable[12]. The described observation is more likely to arise from an interaction with an excited electronic state. As was explained in section 2.2.2, $\lambda$ is associated to both types of interaction, single contributions to the constant cannot be separated quantitatively, thus. For $C_8$, an excited $^3\Pi_g$ state was found roughly 1 eV ($\approx$8000 cm$^{-1}$) above the electronic ground state by means of photoelectron spectroscopy [99], which is close enough for an interaction.

Furthermore, apart from the absolute value, the sign of $\lambda$ changes between $C_6$ and $C_{10}$. As a consequence, for $C_4$ and $C_6$, energy levels are well represented within Hund's case (b) limit, while $C_{10}$ appears to be well described according to inverted Hund's case (a). In an investigation of $C_8$, therefore, the amount and sign of the spin-spin constant can be regarded as crucial parameters.

The first detection of linear $C_8$ in the gas phase was performed by U. Berndt in the course of her PhD thesis [6] with the former setup of the Cologne carbon cluster experiment and published in a recent paper on linear carbon clusters (Neubauer-Guenther *et al.* 2003 [67]). The $C_8$ chain molecule was identified via its $\nu_5$ antisymmetric stretching mode at about 2068 cm$^{-1}$. Transitions near the band center

[12] Even if one considers the electrons in the chain molecules to be delocalised, there is no physical explanation for the increased impact of spins.

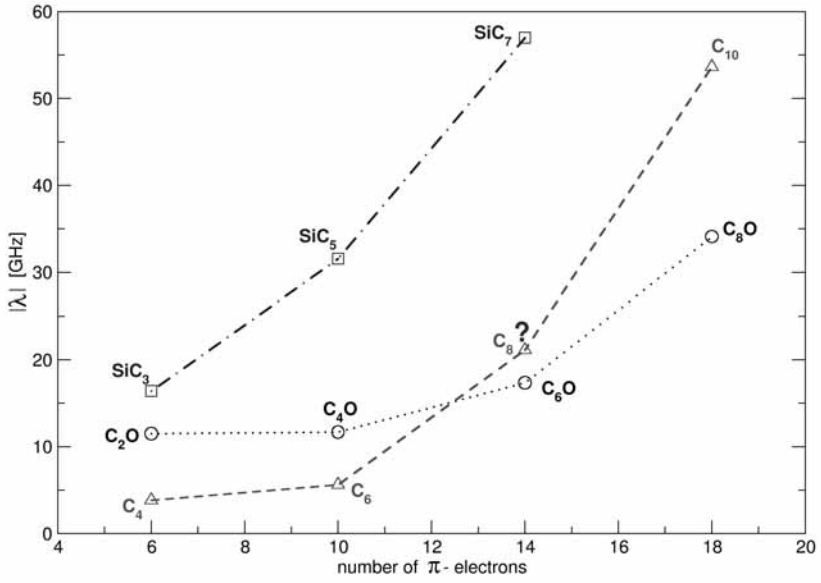


Figure 4.1: Absolute values of $\lambda$ in GHz for different carbon chain molecules against the number of $\pi$-electrons taken from references [26, 31, 46, 61, 69] (see also Table 4.2). For $C_8$, the tentative value of reference [67] is shown (denoted with question mark). The dashed lines are shown to clarify the trend. They do not represent algebraic functions or fit results.

stemming from low rotational quantum numbers were too weak to be taken into account in the subsequent analysis (see Figure 3.11). As a consequence, the band center remained uncertain by four times the rotational quantum number $N$ or 0.17 $cm^{-1}$ [67]. The derived value for $\lambda$ was classified as tentative, hence.

As implied in chapter 3, the performance of the new experimental setup was tested by detecting rovibrational transitions of the $C_8$ molecule for two reasons. First, it was essential to remeasure the $\nu_5$ band to enable a reliable analysis. In addition, production and detection parameters of the new assembly could be optimised, since the frequency region was already known.

After increasing the spectrometer's sensitivity, it was possible to obtain new spectra of the $\nu_5$ band with an SNR improved by at least a factor of ten. The final results on $C_8$ derived from the remeasured spectra are presented in the following chapter.

## 4.1 Infrared Spectra of linear $C_8$

Scanning the frequency range between 2066 and 2069 $cm^{-1}$ a number of absorption lines becomes visible. They were identified to arise from the $\nu_5$ antisymmetric stretching mode of linear $C_8$ by comparison with available matrix data (2063.9 and 2067.8 $cm^{-1}$, see Table 2.1) and *ab initio* calculations (e.g. 2109 $cm^{-1}$ [44]). Figure 4.2 shows the measured spectrum, which clearly indicates a linear molecule

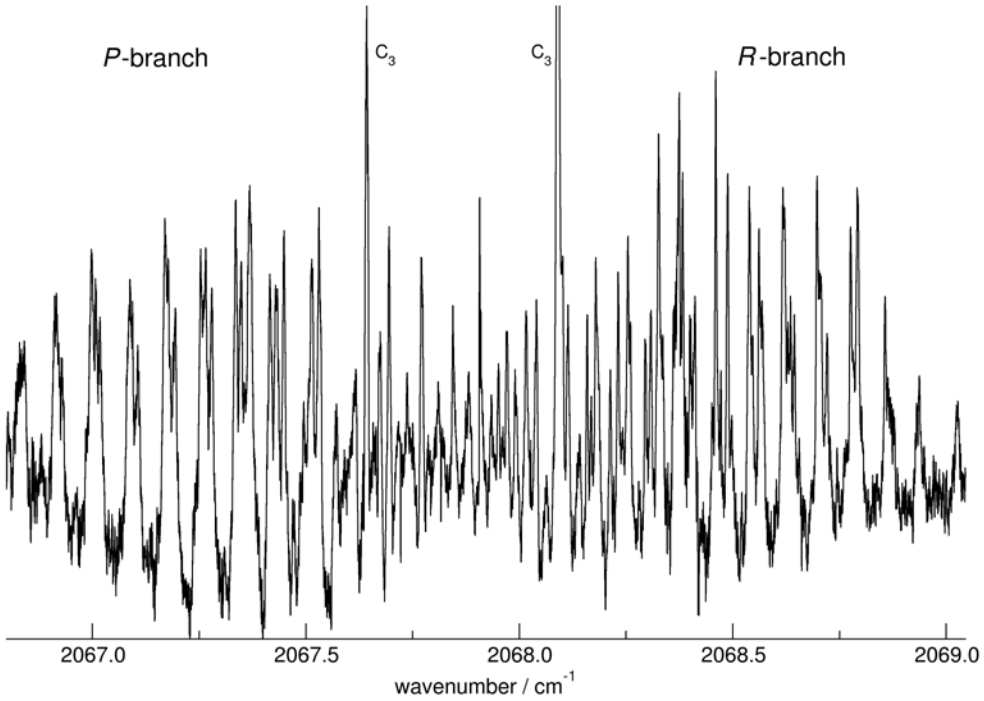


Figure 4.2: Measured spectrum of the $\nu_5$ band of $C_8$. Two strong features of $C_3$ occur in the same frequency region.

in a $^3\Sigma$ electronic ground state. The triplet splitting is less distinct at the end of both the *P*- and the *R*-branch. Closer to the band center, the splitting appears to increase leading to a more blurred structure. There, the triplet splitting seems to be of the same order as the rotational splitting.

The appearance of the spectrum as well as measured line positions are in agreement with the earlier investigations [67]. Nevertheless, the improved signal-to-noise ratio results in an increased number of transitions to be assigned to this band. In the following analysis, 76 lines have been included.

However, not all of the features observable in the spectra have to be transitions of the $C_8$ molecule. As was mentioned in the previous chapter, especially transitions of $C_3$ proved to have an unrequested influence on the spectrum. Thus, it cannot be ruled out that some of the lines belong to transitions of $C_3$ or that $C_8$ features are even superimposed or blended by $C_3$ lines in some cases. Two strong features definitely arising from $C_3$ transitions are marked in Figure 4.2.

## 4.2 Analysis

As can be taken from the overall spectrum in Fig. 4.2, one can clearly recognise the *P*- and the *R*-branch but the determination of the band origin is somewhat hampered by several features which may originate from $C_8$ but could also arise

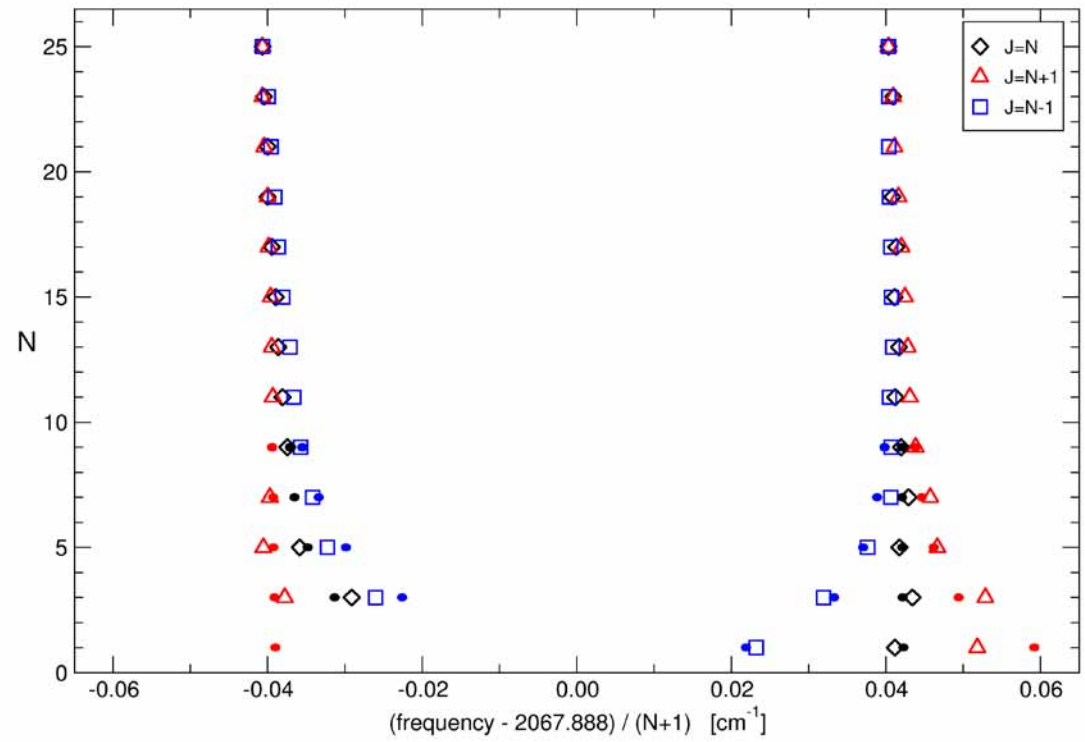


Figure 4.3: Loomis-Wood-Plot for Fit 1 including predicted values for low $N$ transitions (depicted as small dots). Note, that the frequency axis was scaled with respect to the band origin. In this description, *P*-branch lines occur shifted to lower frequencies.

from $C_3$. To assign the lines, one has to overcome two problems: the identification of the spin components and the determination of the absolute numbering concerning the rotational quantum number $N$. In the course of this thesis, several assignments were tested, including crossings and shifts between spin components which are observable in the case of $C_{10}$ [26].

None of the tested assignments gave fully satisfying results. In fact, fitting transitions with high $N$ quantum numbers, pertaining to high total angular momenta $J$, was possible in terms of both reasonable molecular constants and maintainable fit quality. Difficulties arose whenever lines near the band center were included.

The plethora of possible assignments can be reduced to two yielding the most reasonable fits. Both alternatives are similar concerning the assignment of the spin components but absolutely shifted by $2N$. Hereafter, these assignments are refered to as Fit 1 and Fit 2. They are presented as Loomis-Wood plots in Figures 4.3 and 4.4, where the rotational quantum number $N$ is plotted against the frequency devided by $(N + 1)$. As can be clearly seen, the classification of the observed lines into the three spin components appears to be reasonable, since the influence of the triplet splitting is shown to increase with decreasing $N$. Furthermore, the components do not mix for low $N$ values, as expected. For comparison, calculated values derived from the fits are also shown in the Loomis-

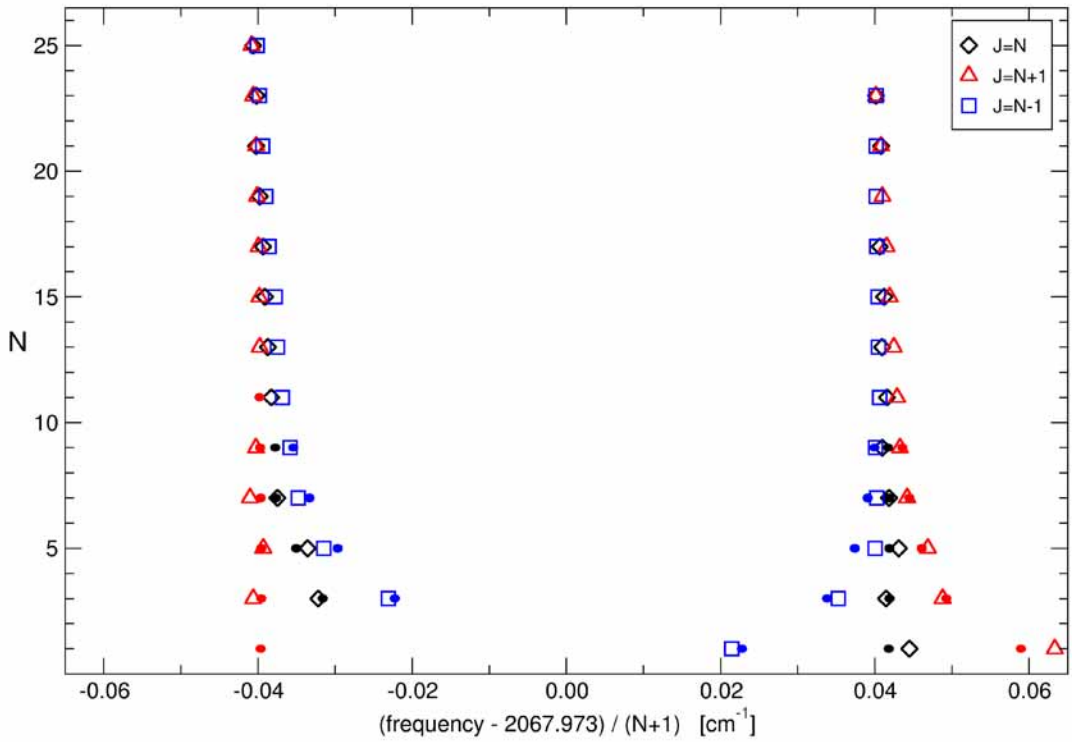


Figure 4.4: Loomis-Wood-Plot for Fit 2 including predicted values for low $N$ transitions (depicted as small dots). The frequency axis was scaled with respect to the band origin. *P*-branch lines occur shifted to lower frequencies.

Wood plots for transitions up to $N = 9$.

Apart from generating Loomis-Wood plots, calculating combination differences has proven to be a helpful tool to check for reasonable assignments. Comparing frequencies for *P*- and *R*-branch transitions sharing a common upper or lower level yields information on the energy differences in the ground or excited state, respectively. In a first approximation, the ground state rotational constant can be derived from $R(N) - P(N+2) = 2B_0(2N+3)$. In case of $C_8$, the triplet splitting and, eventually, centrifugal distortion effects cause deviations from this simple estimation. Combination differences for the vibrational ground and excited states plotted against the rotational quantum number $N$ are shown in Figures 4.5 to 4.8 including the corresponding fit results. These plots clearly show the expected triplet splitting. Furthermore, they point at a significant deviation from the applied fit model.

Fits to the Hamiltonian (2.16) in a Hund's case (b) basis set were performed in a least squares analysis using the Pickett programme [73]. Table 4.1 gives the resulting molecular constants along with the RMS (root-mean-square) values for both assignments and two sets of parameters. To account for centrifugal distortion effects, $\lambda_D$ was included in one set along with $D$. The spin-rotational coupling constant $\gamma$ turned out to be not significant and was thus omitted. The RMS value may be regarded as a measure for the discrepancy between standard deviation of

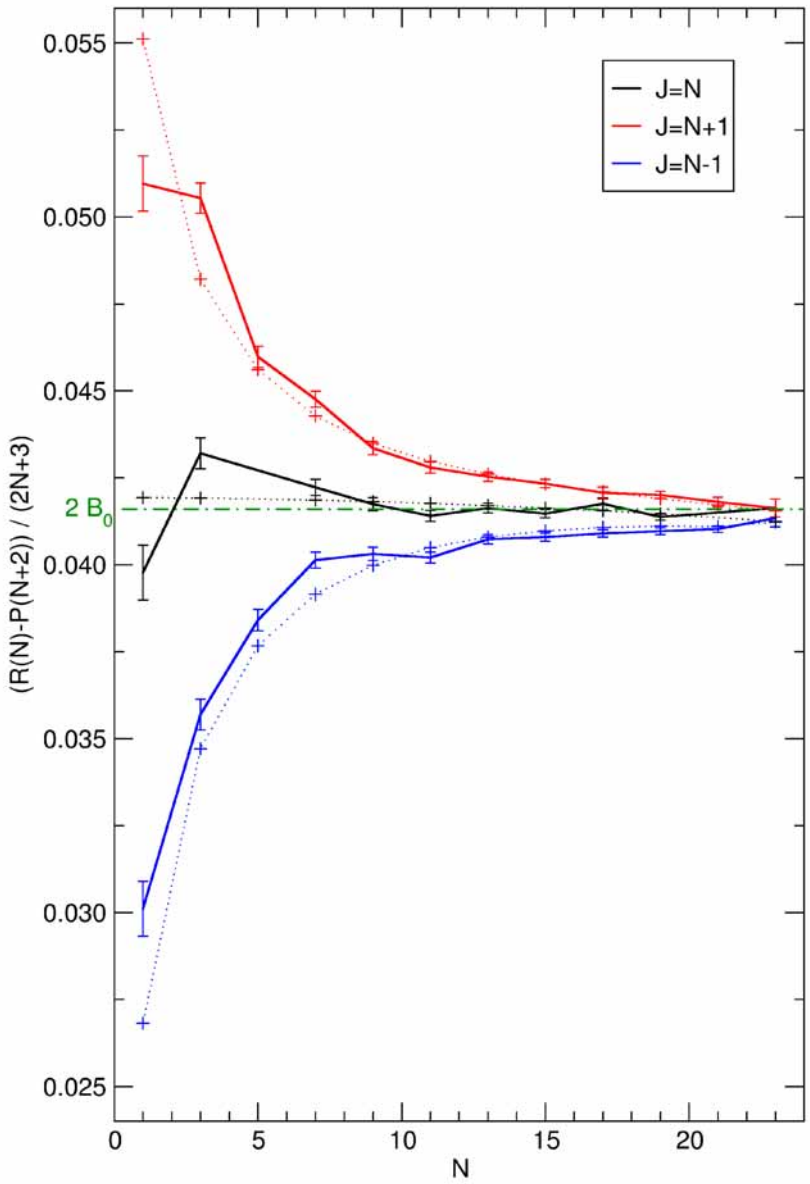


Figure 4.5: Ground state combination differences for the assignment according to Fit 1. The spin components are colour-coded. The calculated values are connected with a dotted line. A line at $2\,B_0$ is plotted for reference. Note, that $B_0$ was taken from the fit without centrifugal distortion constants.

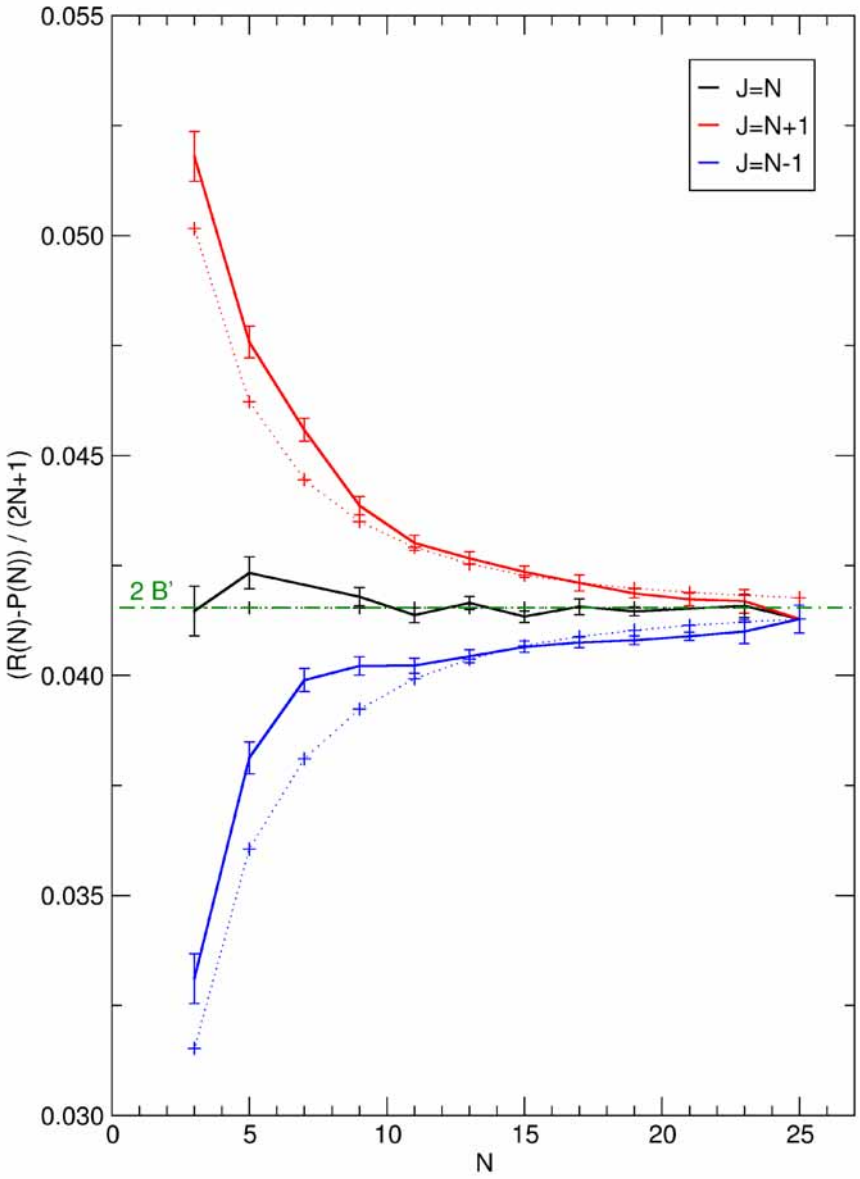


Figure 4.6: Combination differences for the excited vibrational state for Fit 1. The spin components are colour-coded. Dotted lines indicate the calculations. The reference value for $B'$ was taken from the fit without centrifugal constants.

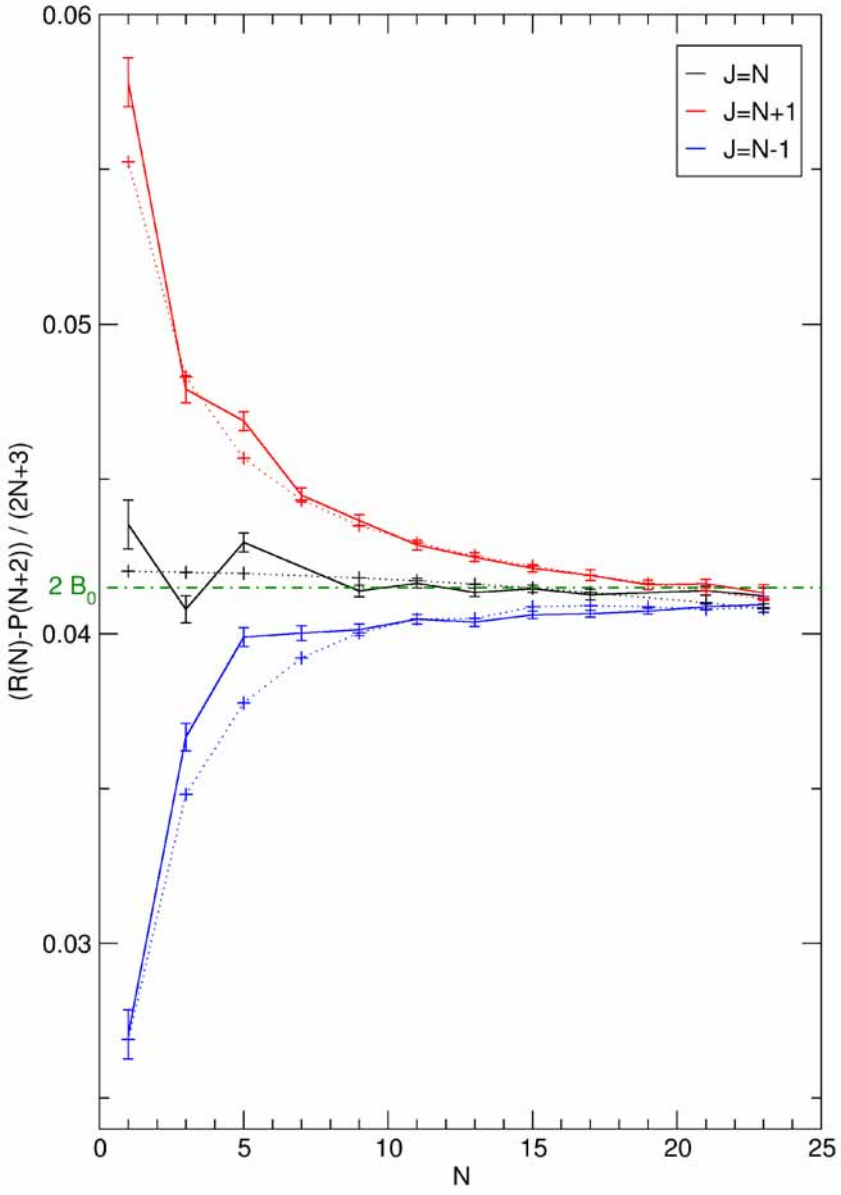


Figure 4.7: Ground state combination differences for the assignment according to Fit 2. The spin components are colour-coded. The calculated values are connected with a dotted line. A line at $2\,B_0$ is plotted for reference. Note, that $B_0$ was taken from the fit without centrifugal distortion constants.

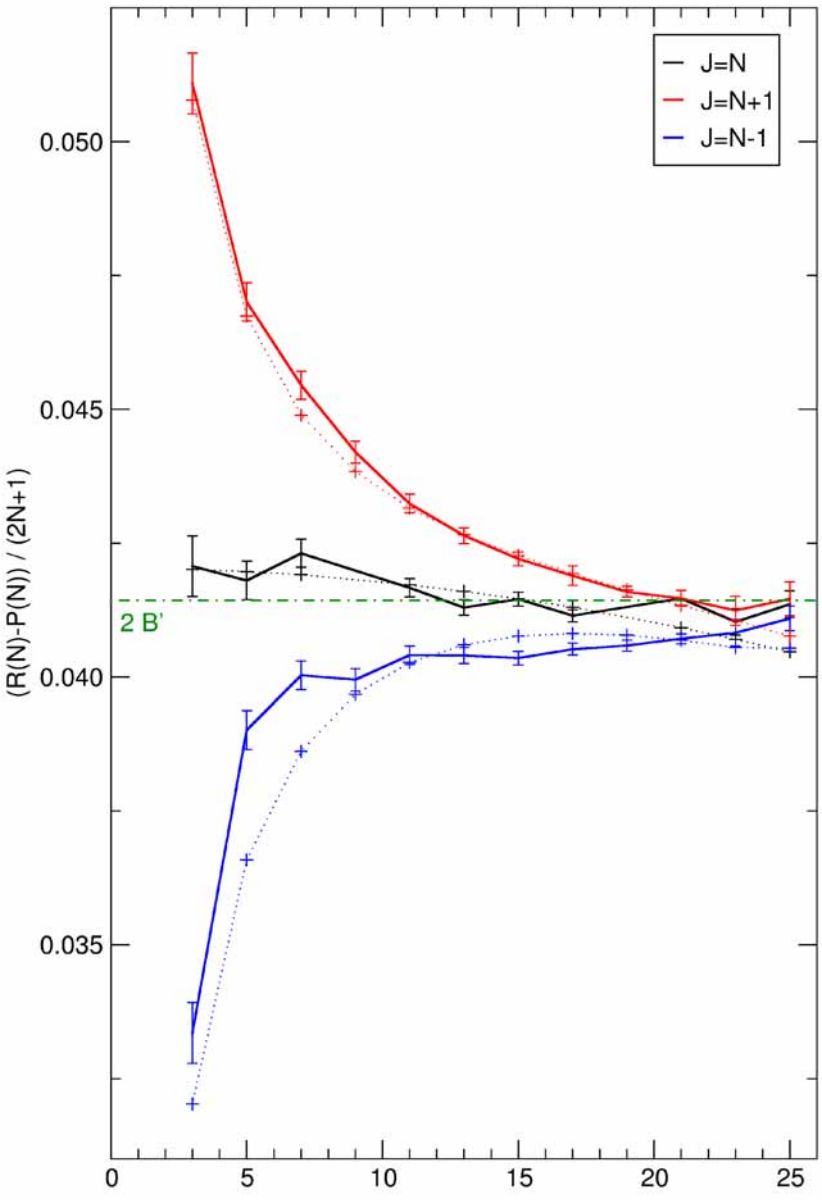


Figure 4.8: Combination differences for the excited vibrational state for Fit 2. The spin components are colour-coded. Dotted lines indicate the calculations. The reference value for $B'$ was taken from the fit without centrifugal constants.

a fit and experimental uncertainties. If the RMS equals one, the accuracy of the fit corresponds to the accuracy of the measurements. Here, experimental uncertainties for single features in the spectrum were set to 0.002 $cm^{-1}$. In cases where the triplet splitting could not be resolved, the uncertainty was larger, i.e. 0.004 or 0.008 $cm^{-1}$, respectively. Intensities of calculated lines agree best, when excitation temperatures of 10 to 15 K were assumed, which is in good agreement with rotational temperatures of molecules in a supersonic jet. For comparison, calculated values by P. Botschwina are also included in Table 4.1.

The obtained RMS values indicate that both Fit 1 and Fit 2 slightly differ from the standard model of Hund's case coupling. Including centrifugal distortion constants does improve the RMS results but the obtained values appear too large compared to other carbon chain molecules.

All 76 classified line positions of Fit 1 are listed in Tables 4.3 and 4.4 along with their residuals. The corresponding assignment is indicated in Figure 4.9, which shows a close-up of the spectrum compared to a prediction generated with the parameters given in Table 4.1.

The analysis is summarised in the following list:

- The $B_0$ values for Fit 1 and Fit 2 are comparable within both parameter sets, but differ from the recommended *ab initio* value, which is supposed to be accurate within at least 1 % . If $D$ is included, the rotational constants deviate by roughly 3 % . Without centrifugal distortion, the deviation still amounts for 1.5 % (Fit 2) and 1.8 % (Fit 1)
- If $D$ is included, $\Delta B = B' - B_0$ for Fit 2 is a factor of 2 smaller than for Fit 1, 0.05 % compared to 0.12 %. However, this effect is not present when $D$ is discluded from the fit.
- In all cases, the values for $\lambda$ are comparable and have the same sign. The constants barely change upon excitation of the stretching mode.
- The $D''$ values differ by a factor of 2, but both values can be regarded as too large, since $D$ is not supposed to exceed the value for the longer chain $C_{10}$, which was determined to be in the order of $10^{-9}$ [26].
- Both $\lambda_D$ values are of the same order of magnitude with $\Delta\lambda_D$ larger for Fit 1.
- Within both parameter frames, Fit 2 has the lower RMS values indicating that this assignment can be reproduced slightly more accurate within experimental errors.

## 4.3 Discussion

The presented results on the molecular constants for the linear $C_8$ chain are the best available, since no other experiment has proven to be able to yield comparable measurements, yet. Nevertheless, the quality of the fits strongly advises

Table 4.1: Molecular constants in units of $cm^{-1}$ are given for the two most reasonable assignments for 76 lines of the $\nu_5$ antisymmetric stretching fundamental of $C_8$. Both fits were also performed without centrifugal distortion constants (see lower part of the Table).

| Parameter | Fit 1 | Fit 2 | *ab initio* |
|---|---|---|---|
| $\nu$ | 2067.88819(51) | 2067.97290(50) | 2109 [44] |
| $B'' = B_0$ | 0.0209971(224) | 0.0210521(223) | 0.02043 [10] |
| $D''$ [$\times 10^{-7}$] | 2.88(32) | 5.07(32) | |
| $\lambda''$ | -0.651(23) | -0.658(23) | |
| $\lambda''_D$ [$\times 10^{-5}$] | -3.73(205) | -5.45(205) | |
| $B'$ | 0.0210214(220) | 0.0210616(234) | |
| $D'$ [$\times 10^{-7}$] | 3.93(31) | 6.05(37) | |
| $\lambda'$ | -0.649(23) | -0.659(23) | |
| $\lambda'_D$ [$\times 10^{-5}$] | -4.48(228) | -5.98(210) | |
| RMS | 2.73 | 2.48 | |
| $\nu$ | 2067.89164(51) | 2067.97494(39) | 2109 |
| $B'' = B_0$ | 0.0207979(93) | 0.0207443(94) | 0.02043 |
| $\lambda''$ | -0.636(15) | -0.639(15) | |
| $B'$ | 0.0207701(92) | 0.0207154(98) | |
| $\lambda'$ | -0.635(15) | -0.640(15) | |
| RMS | 3.37 | 3.19 | |

a careful discussion. Apart from the RMS value, both types of diagrams clearly reveal distinct discrepancies between measurements and fitted model near the band center. An investigation on possible reasons for this effect will be given at the end of this section.

The deviations between fitted and predicted rotational constants are exceptionally large given the usual quality of calculations performed by P. Botschwina (see e.g. the following chapter). Thus, the derived rotational constants are examined more closely, in particular with respect to the centrifugal distortion constants.

Fitting only higher $N$ rovibrational transitions of the spectrum including distortion constants, results in $B_0$ values of approximately 0.02075 $cm^{-1}$ for both assignments. Any effort to restrict the fit to lines close to the band origin yields $B_0$ values in the range of 0.02100 $cm^{-1}$. The same trend becomes obvious in the plots of the combination differences. In each of the Figures 4.5 to 4.8 a reference line is plotted at the corresponding 2 $B$ value to illustrate the fact, that for high $N$, both the measurements and the calculations are well described by the rotational constants derived when neglecting distortion effects. If $D$ values are included, the fitting routine tends to balance the contributions of the three components for low $N$ transitions leading to higher $B$ values. As a result, low $N$ transitions gain a large impact on the $D$ constants. Since this effect is not only unusual but also physically not meaningful including centrifugal distortion effects cannot be regarded as

reliable method.

Given the significant deviations between observations and calculations, the whole data set as well as the setup have been thoroughly checked for systematical errors. Inaccurate calibration can be excluded for two reasons. First, the results on $C_7$ were obtained with the same system except for the diode laser. The corresponding analysis (see chapter 5) gave no reason to doubt the calibration accuracy. However, problems with a single diode laser may occur, but the $C_8$ band was remeasured in the scope of this work. This leads to the second reason. The measurements carried out by U. Berndt on the same subject revealed a similar strange behaviour [6], although they have been measured with the old setup including a different IR laser. Figure 3.11 may be used to receive an impression of this similarity. Consequently, neither of the experimental parameters could be hold responsible for the particular results on $C_8$.

Deviations between observed and calculated line positions are by far not unusual. Still, in most cases, reasonable explanations are at hand. Resonances may occur between energy levels of the same symmetry resulting into energy shifts. For the $C_8$, an excited $^3\Pi_g$ state only 1 eV above the ground state [99] would be suitable for this. If any resonance arises from higher states, it is more likely to occur in the vibrational excited rather than the ground state. As a consequence, one should be able to identify pairs of lines sharing the same upper level with the same trend in the shifts. Such a behaviour could not be confirmed for neither of the states.

### 4.3.1 Coupling mechanisms

In Table 4.2 the available values for the spin-spin coupling constants, are compiled for the isoelectronic carbon chains $C_n$, $C_nO$, and $SiC_n$. The $SiC_n$ chains measured by McCarthy *et al.* by means of pure rotational spectroscopy (FTMW) [61] have a $^3\Sigma$ electronic groundstate for odd values of n. Hence, the reported negative signs is stringent, since observations of pure rotational transitions between the different spin components ascertain the sequence of the energy levels. The same holds true for the $C_nO$ chains. Again, the $\lambda$ values result from FTMW spectra [69], the information on the positive sign is reliable, therefore.

It was already pointed out, that in the series of the pure carbon chains a change of sign for the spin-spin coupling constant can be observed. For the present analysis of $C_8$, both fits showed the same trend, namely that the sign in the fit is settled when lines assigned as *R(1)* or *R(3)* are included in the fits. Nevertheless, since no *Q*-branch transition inbetween the energy stacks could be assigned, and given the large deviations between observed and predicted line positions near the band origin, the sign should be regarded as tentative, still.

Concerning the absolute value of $\lambda$, the derived constant fits well into the trend. With the criterion for the coupling scheme introduced in section 2.2.2, for $C_4$ and $C_6$, the values for $\lambda$ combined with the corresponding rotational constants indicate that both molecules are well represented within case (b) limit as mentioned

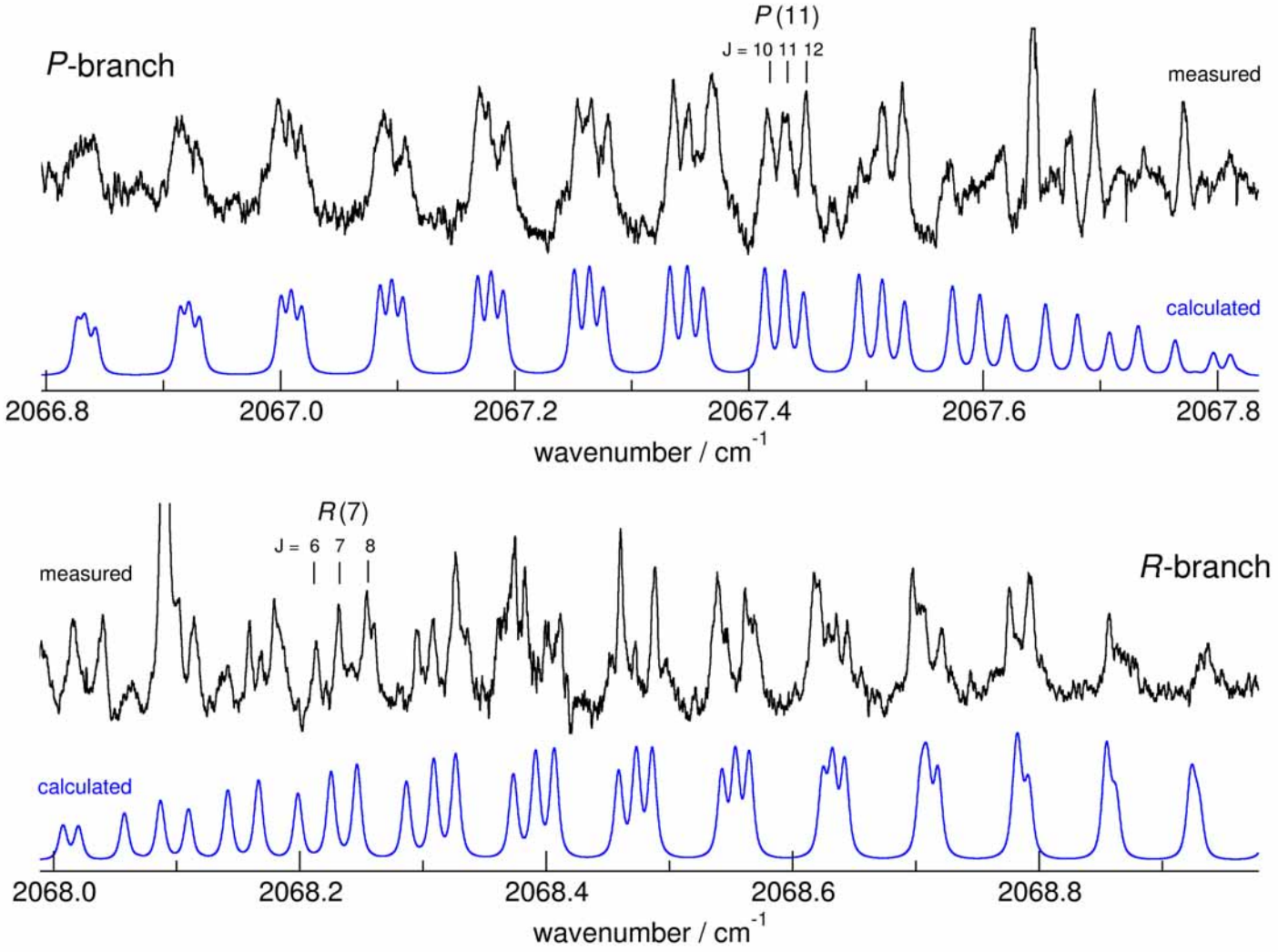


Figure 4.9: The $\nu_5$ band of $C_8$: comparison between measured and calculated spectrum. *P*- and *R*-branch are displayed separately for convenience reason. The assignment is pursuant to Fit 1. In both branches, the $N$ as well as the $J$ labelling is indicated. As expected, the accordance between observation and prediction becomes worse closer to the band origin. Note the more doublet-like appearance in parts of the *R*-branch.

before. On the contrary, $C_{10}$ appears to be well described according to inverted Hund's case (a).

$C_8$ can be interpreted as transient molecule from the coupling scheme (a) to (b). With $B_0 = 0.0207979$ cm$^{-1}$and $|\lambda| = 0.636$, one derives values for the total angular momentum $J$ of around 10 for which a spin uncoupling occurs. In a classical picture, upon exciting the molecule's rotation the spin is forced to uncouple from the molecular to the rotational axis. This effect is indeed observable in the IR spectrum, since the amounts of the rotational and the triplet splitting become comparable at $N = 7$. Thus, $C_8$ can be described within the limits of Hund's cases (a) and (b) only for very low and very high rotational quantum numbers.

According to the theory described in section 2.2.2 Mathematically, a Hund's case (a) basis set can be converted into a case (b) one and vice versa. The fact, that $C_8$

Table 4.2: Reference values for the spin-spin coupling constant $\lambda$ for $C_n$ $C_nO$, and $SiC_n$ in units of cm$^{-1}$. For $C_nO$ and $SiC_n$ the given values have been derived from FTMW spectra. Note that in both cases the accuracies reported by the authors are significantly better than indicated in the table below. For $C_4$, the $\lambda$ value results from ESR measurements [31]. For the other pure carbon chains gas phase values were available ($C_6$ [46], $C_8$ this work, $C_{10}$ [26]).

| number of $\pi$-electrons | $C_n$ | | $C_nO$ [69] | | $SiC_n$[61] | |
|---|---|---|---|---|---|---|
| | n | $\lambda$ | n | $\lambda$ | n | $\lambda$ |
| 6 | 4 | 0.128 | 2 | 0.3835 | 3 | -0.5472 |
| 10 | 6 | 0.1875 | 4 | 0.3896 | 5 | -1.0527 |
| 14 | 8 | -0.636(15) | 6 | 0.5788 | 7 | -1.9245 |
| 18 | 10 | -1.79 | 8 | 1.1373 | | |

Table 4.3: Observed line positions of $C_8$ in the *P*-branch of the $\nu_5$ band in $cm^{-1}$ assigned according to Fit 1. Residuals refering to the fit without centrifugal distortion constants.

| $N'$ | $J'$ | $N''$ | $J''$ | $\nu_{obs}$ | $\nu_{obs} - \nu_{calc}$ |
|---|---|---|---|---|---|
| 24 | 25 | 25 | 26 | 2066.83100 | 0.00194 |
| 24 | 24 | 25 | 25 | 2066.83100 | -0.00483 |
| 24 | 23 | 25 | 24 | 2066.83100 | -0.01012 |
| 22 | 23 | 23 | 24 | 2066.91147 | -0.00261 |
| 22 | 22 | 23 | 23 | 2066.91640 | -0.00523 |
| 22 | 21 | 23 | 22 | 2066.92995 | 0.00210 |
| 20 | 21 | 21 | 22 | 2066.99820 | -0.00054 |
| 20 | 20 | 21 | 21 | 2067.00810 | 0.00089 |
| 20 | 19 | 21 | 20 | 2067.01766 | 0.00312 |
| 18 | 19 | 19 | 20 | 2067.08773 | 0.00475 |
| 18 | 18 | 19 | 19 | 2067.08773 | -0.00484 |
| 18 | 17 | 19 | 18 | 2067.10607 | 0.00483 |
| 16 | 17 | 17 | 18 | 2067.17044 | 0.00366 |
| 16 | 16 | 17 | 17 | 2067.17769 | -0.00002 |
| 16 | 15 | 17 | 16 | 2067.19314 | 0.00514 |
| 14 | 15 | 15 | 16 | 2067.25434 | 0.00427 |
| 14 | 14 | 15 | 15 | 2067.26460 | 0.00198 |
| 14 | 13 | 15 | 14 | 2067.27911 | 0.00424 |
| 12 | 13 | 13 | 14 | 2067.33575 | 0.00295 |
| 12 | 12 | 13 | 13 | 2067.34739 | 0.00008 |
| 12 | 11 | 13 | 12 | 2067.36854 | 0.00660 |
| 10 | 11 | 11 | 12 | 2067.41614 | 0.00124 |
| 10 | 10 | 11 | 11 | 2067.43110 | -0.00068 |
| 10 | 9 | 11 | 10 | 2067.44855 | -0.00071 |
| 8 | 9 | 9 | 10 | 2067.49325 | -0.00305 |
| 8 | 8 | 9 | 9 | 2067.51365 | -0.00238 |
| 8 | 7 | 9 | 8 | 2067.53095 | -0.00594 |
| 6 | 7 | 7 | 8 | 2067.57040 | -0.00654 |
| 6 | 5 | 7 | 6 | 2067.61471 | -0.01015 |
| 4 | 5 | 5 | 6 | 2067.64483 | -0.01196 |
| 4 | 4 | 5 | 5 | 2067.67311 | -0.01075 |
| 4 | 3 | 5 | 4 | 2067.69462 | -0.01851 |
| 2 | 3 | 3 | 4 | 2067.73710 | 0.00120 |
| 2 | 2 | 3 | 3 | 2067.77169 | 0.00425 |
| 2 | 1 | 3 | 2 | 2067.78410 | -0.01750 |

Table 4.4: Observed line positions of $C_8$ in the *R*-branch of the $\nu_5$ band in $cm^{-1}$ assigned according to Fit 1. Residuals refering to the fit without centrifugal distortion constants.

| $N'$ | $J'$ | $N''$ | $J''$ | $\nu_{obs}$ | $\nu_{obs} - \nu_{calc}$ |
|---|---|---|---|---|---|
| 2 | 1 | 1 | 0 | 2067.93466 | 0.00042 |
| 2 | 2 | 1 | 1 | 2067.97057 | -0.00485 |
| 2 | 3 | 1 | 2 | 2067.99190 | -0.01720 |
| 4 | 3 | 3 | 2 | 2068.01590 | -0.00638 |
| 4 | 4 | 3 | 3 | 2068.06198 | 0.00376 |
| 4 | 5 | 3 | 4 | 2068.09970 | 0.01268 |
| 6 | 5 | 5 | 4 | 2068.11404 | 0.00430 |
| 6 | 6 | 5 | 5 | 2068.13879 | -0.00201 |
| 6 | 7 | 5 | 6 | 2068.16821 | 0.00299 |
| 8 | 7 | 7 | 6 | 2068.21320 | 0.01672 |
| 8 | 8 | 7 | 7 | 2068.23155 | 0.00839 |
| 8 | 9 | 7 | 8 | 2068.25417 | 0.01041 |
| 10 | 9 | 9 | 8 | 2068.29511 | 0.01268 |
| 10 | 10 | 9 | 9 | 2068.30776 | 0.00247 |
| 10 | 11 | 9 | 10 | 2068.32657 | 0.00391 |
| 12 | 11 | 11 | 10 | 2068.37373 | 0.00614 |
| 12 | 12 | 11 | 11 | 2068.38266 | -0.00455 |
| 12 | 13 | 11 | 12 | 2068.40550 | 0.00365 |
| 14 | 13 | 13 | 12 | 2068.46036 | 0.00836 |
| 14 | 14 | 13 | 13 | 2068.47193 | 0.00303 |
| 14 | 15 | 13 | 14 | 2068.48778 | 0.00650 |
| 16 | 15 | 15 | 14 | 2068.53941 | 0.00368 |
| 16 | 16 | 15 | 15 | 2068.54616 | -0.00421 |
| 16 | 17 | 15 | 16 | 2068.56745 | 0.00657 |
| 18 | 17 | 17 | 16 | 2068.61945 | 0.00060 |
| 18 | 18 | 17 | 17 | 2068.63243 | 0.00081 |
| 18 | 19 | 17 | 18 | 2068.64417 | 0.00359 |
| 20 | 19 | 19 | 18 | 2068.69729 | -0.00413 |
| 20 | 19 | 19 | 18 | 2068.70464 | -0.00800 |
| 20 | 21 | 19 | 20 | 2068.72059 | 0.00028 |
| 22 | 21 | 21 | 20 | 2068.77610 | -0.00741 |
| 22 | 23 | 21 | 22 | 2068.79260 | -0.00744 |
| 24 | 23 | 23 | 22 | 2068.85686 | -0.00831 |
| 24 | 24 | 23 | 23 | 2068.87086 | -0.00317 |
| 24 | 25 | 23 | 24 | 2068.87086 | -0.00886 |
| 26 | 25 | 25 | 24 | 2068.93651 | -0.00992 |
| 26 | 26 | 25 | 25 | 2068.93651 | -0.01787 |
| 26 | 27 | 25 | 26 | 2068.93651 | -0.02280 |
| 28 | 27 | 27 | 26 | 2069.02582 | -0.00151 |
| 28 | 28 | 27 | 27 | 2069.02582 | -0.00870 |
| 28 | 29 | 27 | 28 | 2069.02582 | -0.01298 |

# 5

# Measurements on Linear $C_7$ – Floppy or not?

The first infrared detection of linear $C_7$ in the gas phase was reported by the Saykally group in Berkeley in 1990 [35]. They identified the linear $C_7$ chain via the analysis of the $\nu_4$ antisymmetric stretching mode at about 2138 $cm^{-1}$. One year later, the same group published data of two hot bands arising from the lowest bending mode $\nu_{11}$ in the same frequency region [36]. However, their analysis of the latter data gave somewhat surprising results. An unusually large and negative distortion constant $D$ for the ground state was derived, presumably arising from Coriolis interactions between the ground state and excited levels of the $\nu_{11}$ mode. Furthermore, the rotational constant obtained for the lowest bending mode differs by roughly 9 % from the ground state value, which the autors explained with a large-amplitude bending motion of an extremely floppy carbon chain. Thereupon, the authors derived the theory of alternating rigidity described in section 2.1.2.

The floppiness of the $C_7$ chain was more or less commonly accepted until in 2002 P. Botschwina published high-level coupled cluster calculations on $C_7$ [9]. These *ab initio* calculations showed no evidence of floppiness for the $C_7$ chain. Neither the negative large $D$ constant nor the dramatical change in the rotational constant due to the excitation of the first bending level could be confirmed.

The large discrepancy of theory and experiment showed that further measurements were strongly in demand. In the course of this thesis, new measurements on the $\nu_4$ fundamental and associated hot bands of $C_7$ have been performed.

## 5.1 IR Spectra

The measured data were calibrated with known line positions of $N_2O$ as recommended in reference [32]. An overview of all measured lines in the range of 2134.9 to 2139.3 $cm^{-1}$ is given in Figure 5.1. It shows the main part of the

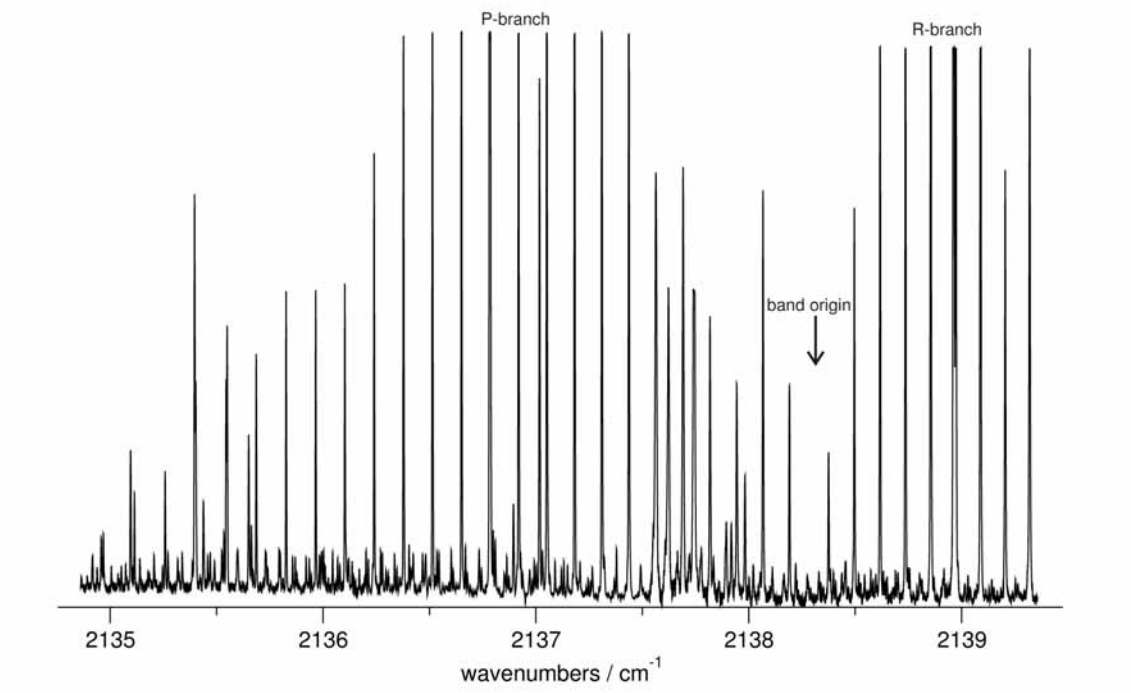


Figure 5.1: Spectrum of the $\nu_4$ fundamental of $C_7$ and associated hotbands: survey of the *P*-branch and beginning of the *R*-branch of the $\nu_4$ mode. The transitions with the highest intensities belong to the fundamental. In between the regular 4 $B$ spacing of the fundamental, several more lines are observable arising from at least three hot bands.

*P*-branch and the beginning of the *R*-branch of the $\nu_4$ fundamental antisymmetric stretching mode of $C_7$. Between the fundamental lines, a plethora of weaker lines is observable. The major part of these lines originates from associated hot bands. Furthermore, some partly strong features of unknown origin occur in this frequency region as well as two transitions of the 2 $\nu_2$ + $\nu_3$ combination band of $C_3$ interfering with $C_7$ lines.

## 5.2 The $\nu_4$ fundamental

The analyis of the $\nu_4$ fundamental proved to be plain sailing. Transitions arising from the fundamental mode are identified quite easily due to their intensity and the prominent 4 $B$ spacing between adjacent lines (see section 2.2.1). Due to the well resolved *P*- and *R*-branch with a clearly visible band origin with 6 $B$ spacing, the assignment of the observed lines was straightforward and is in agreement with the assignment by Heath *et al.* [36]. Within the scope of this work, 34 lines of this band have been re-measured and 7 new lines in the *R*-branch with $J = 50$–62

have been observed. A fit to the expression

$$E = \left(v + \frac{1}{2}\right)\nu + B_v[J(J+1)] - D_v[J(J+1)]^2 \ldots \tag{5.1}$$

was performed in a least squares analysis using the Pickett programme [73]. Furthermore, previously published line positions of ref. [36] were included which could not be observed in this study due to the range covered by the diode lasers used. The latter line positions were given an uncertainty of 0.002 cm$^{-1}$. For frequencies measured in the course of this thesis, the calibration accuracy allows for an uncertainty of 0.001 cm$^{-1}$ in most cases.

Observed frequencies and their deviations from the calculated values are given in Table 5.1. The quality of the fit is expressed by the RMS value of 1.005. The derived parameters are given in Table 5.2. In contrast to the results of Heath *et al.*, no quartic or even sextic centrifugal distortion parameters were needed to fit the data, and including those constants did not improve the fit significantly. If $D$ values are used in the fit, they are positive and one order of magnitude smaller than those given by Heath *et al.* [36]. Both the values for the band origin and the rotational constants are in agreement. The accuracies for the $B$ constants of this work are better due to fewer parameters fitted. For comparison, *ab initio* values for the $B$ constants are reported here which were derived using equation (2.9) and calculated results from reference [9].

## 5.3 Hot bands

The classification of the hot band transitions turned out to be quite complicated. Due to the sheer number of lines a clear *P*- and *R*-branch pattern was not obvious for either of the bands. The final assignment is shown in Figure 5.2. It was guided by the search for patterns with $2\,B$ or $4\,B$ spacing. Three groups of transitions with a suitable $2\,B$ spacing have been found showing a more or less distinctive staggering of adjacent lines. These transitions were likely to arise from the lowest and the second lowest bending mode ($\nu_{11}$ and $\nu_8$). One would expect that lines arising from the lowest bending could be identified as second strongest features. However, as becomes evident in Fig. 5.2, two observed hot bands display nearly the same intensity in this region, while the transitions of a third hot band exhibit significantly lower intensities. Thus, intensity considerations were not helpful at first glance.

Still, the lines of two groups occur in a clear $2\,B$ distance with a slight staggering and could, therefore, be assigned to the $\nu_4 + \nu_{11} - \nu_{11}$ and $\nu_4 + \nu_8 - \nu_8$ bands. A major part of the remaining features in the spectrum given in Fig. 5.1 was supposed to arise from the twofold excited bending mode $\nu_{11}$, since the lines of this band show barely a staggering. It was identified as ($\nu_4 + 2\nu_{11} - 2\nu_{11}$, $\ell = 2$) band. As can be taken from the energy level scheme in Fig. 2.6, a hot band arising from the transition ($\nu_4 + 2\nu_{11} - 2\nu_{11}$, $\ell = 0$) should also be observable, then. This band would be characterised by a $4\,B$ spacing due to spin statistics (see section 2.2.1). No such band could be found in the spectra which will be discussed later.

Table 5.1: Observed frequencies for the $\nu_4$ antisymmetric stretching fundamental of $C_7$. Lines marked with an asterisk are taken from reference [36]. All values given in $cm^{-1}$.

| J | *R(J)* | obs-calc ($\times 10^{-3}$) | *P(J)* | obs-calc ($\times 10^{-3}$) |
|---|---|---|---|---|
| 0 | 2138.37556 | 0.11 | | |
| 2 | 2138.49671 | -0.14 | 2138.19113 | -0.50 |
| 4 | 2138.61723 | -0.11 | 2138.06703 | 0.90 |
| 6 | 2138.73632 | -0.58 | 2137.94447 | 1.15 |
| 8 | 2138.85473 | -0.81 | 2137.81819 | 0.40 |
| 10 | 2138.97209 | -1.17 | 2137.69226 | 0.92 |
| 12 | 2139.08896 | -1.09 | 2137.56550 | 1.52 |
| 14 | 2139.20476 | -1.17 | 2137.43730 | 1.60 |
| 16 | 2139.31945 | -1.43 | 2137.30766 | 1.16 |
| 18 | 2139.43580* | 0.90 | 2137.17824 | 1.85 |
| 20 | 2139.54690* | -1.10 | 2137.04666 | 1.30 |
| 22 | 2139.66020* | 0.02 | 2136.91365 | 0.24 |
| 24 | 2139.77180* | 0.38 | 2136.77859 | -1.96 |
| 26 | (2139.88225) | calc. | 2136.64610 | -0.67 |
| 28 | 2139.99220* | 1.09 | 2136.51192 | -0.15 |
| 30 | 2140.09890* | -0.66 | 2136.37800 | 1.54 |
| 32 | 2140.21100* | 3.92 | 2136.24018 | 0.25 |
| 34 | 2140.31370* | 0.04 | 2136.10247 | -0.01 |
| 36 | 2140.42160* | 2.30 | 2135.96361 | -0.50 |
| 38 | 2140.52780* | 3.79 | 2135.82460 | -0.23 |
| 40 | 2140.63130* | 3.53 | 2135.68417 | -0.45 |
| 42 | 2140.73200* | 1.40 | 2135.54473 | 1.24 |
| 44 | 2140.83250* | 0.03 | 2135.40250 | 1.06 |
| 46 | 2140.93420* | 0.80 | 2135.25812 | -0.35 |
| 48 | 2141.03270* | -0.69 | 2135.11418 | -0.40 |
| 50 | 2141.13118 | -1.24 | 2134.96825 | -1.51 |
| 52 | 2141.22995 | -0.55 | 2134.82290* | -1.11 |
| 54 | 2141.32713 | -0.50 | 2134.67760* | 0.26 |
| 56 | 2141.42300 | -0.80 | 2134.52880* | -0.94 |
| 58 | 2141.51772 | -1.29 | 2134.38040* | -0.82 |
| 60 | 2141.61299 | -0.28 | 2134.23370* | 1.94 |
| 62 | 2141.70662 | 0.07 | 2134.08440* | 3.03 |
| 64 | | | 2133.92930* | 0.75 |

Table 5.2: Molecular parameters in units of cm$^{-1}$ for the $\nu_4$ antisymmetric stretching fundamental of $C_7$. Including centrifugal distortion constants did not improve the fit significantly. However, if they are used in the fit, both $D''$ and $D'$ are postive and of the order of 0.3 $\times$ 10$^{-8}$ cm$^{-1}$. *Ab initio* values for $B''$ and $B'$ derived from $\alpha$ values and $B_e$ calculated by Botschwina [9] using equation (2.9). For further comparison, Botschwina calculated $D_e$ to 0.0337 $\times$ 10$^{-8}$ cm$^{-1}$.

| Parameter | This work | Heath *et al.* [36] | *ab initio* |
|---|---|---|---|
| $\nu_4$ | 2138.31443(20) | 2138.3152(5) | 2203.8 |
| $B''$ | 0.0306259(29) | 0.030615(15) | 0.03065 |
| $D''$ [$\times 10^{-8}$] | | -2.4(9) | |
| $H''$ [$\times 10^{-12}$] | | -5.6(15) | |
| $B'$ | 0.0305106(30) | 0.030497(16) | 0.03054 |
| $D'$ [$\times 10^{-8}$] | | -2.6(10) | |
| $H'$ [$\times 10^{-12}$] | | -6.1(17) | |

### 5.3.1 The $\nu_4 + \nu_{11} - \nu_{11}$, $\ell = 1$ hot band

A total of 52 lines could be assigned to this band. Since the staggering of these lines is the most pronounced of all bands, this band must arise from the lowest bending mode $\nu_{11}$ according to equation 2.14. The $\nu_{11}$ mode is of $\pi_u$ symmetry which fixes the absolute $J$-assignment modulo two. The analysis was carried out using the expression

$$E = \left(v + \frac{1}{2}\right)\nu + B_v[J(J+1) - \ell^2] - D_v[J(J+1) - \ell^2]^2 \pm \frac{1}{2}q_v J(J+1). \quad (5.2)$$

The fitting routine LINX was provided by K.M.T. Yamada [101]. Although blurred by a couple of other lines, the band origin could be determined due to the significant shape of the beginning *R*-branch (see Figure 5.3).

All 52 lines are listed in Table 5.3 along with their residuals. Parameters resulting from the fit are given in Table 5.4. The standard deviation of the fit was 0.702 $\times$ 10$^{-3}$. Including centrifugal distortion constants did not improve the quality of the fit.

This band origin is shifted refered to the fundamental one by roughly 0.58 cm$^{-1}$. The derived $B''$ value of 0.0306759(38) cm$^{-1}$ differs only by 0.16 % from $B_0$ and only by 0.14 % from the calculated value for $B_{11}$. For comparison, the analysis on $C_4$ carried out by Moazzen–Ahmadi *et al.* yielded a change in the rotational constant of roughly 0.5 % for the lowest bending. A similar value, 0.4 %, was derived by the same authors in the comparable case of $C_5$. Finally, for $C_9$ van Orden *et al.* [88] derived 0.2 and 0.3 % for the $e$- and $f$-band, respectively.

For comparison, Table 5.4 also includes molecular constants by Heath *et al.* [36] derived from the analysis of 18 lines assigned to this band. These transitions are

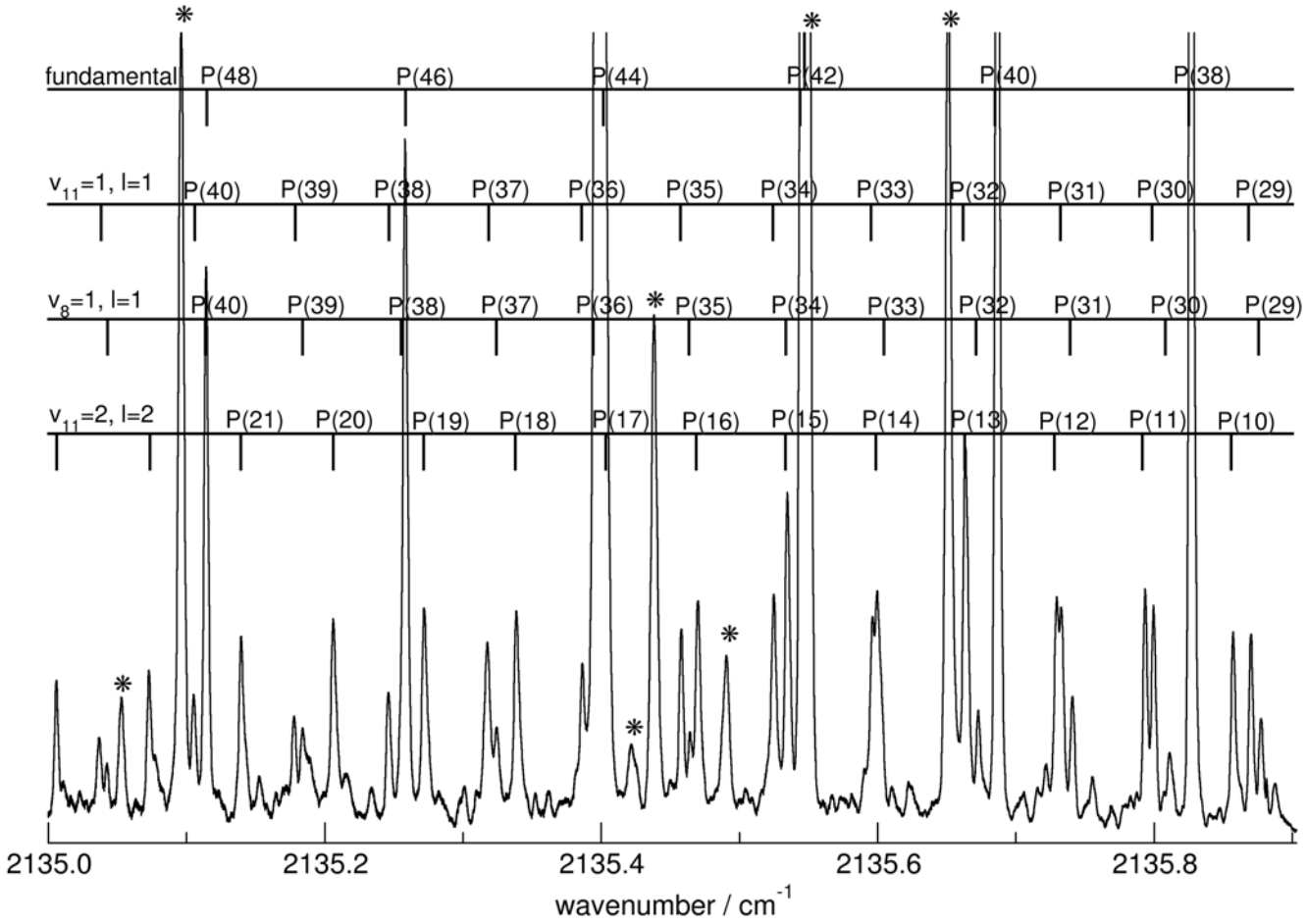


Figure 5.2: Detail of the spectrum of $C_7$: calculated positions and assignments of the $\nu_4$ fundamental and the three identified hot bands are given. Lines labeled with an asterisk could not be assigned yet. Note that in the course of the present analysis, only features with sufficient intensity have been regarded as absorption lines.

Table 5.3: Observed frequencies for the $\nu_4 + \nu_{11} - \nu_{11}$ hot band of $C_7$. Lines in paranthe-ses are calculated values since they are blended with fundamental or uniden-tified transitions ($b$). Due to the $\pi_u$ symmetry of the $\nu_{11}$ bending, lines with odd $J$ belong to the $e$-subband. All values given in $cm^{-1}$.

| J | *R(J)* | obs-calc ($\times 10^{-3}$) | *P(J)* | obs-calc ($\times 10^{-3}$) |
|---|---|---|---|---|
| 1 | 2137.86051 | -0.11 | | |
| 2 | 2137.91915 | -2.33 | (2137.61567) | $b$ |
| 3 | 2137.98229 | 0.64 | (2137.55405) | $b$ |
| 4 | (2138.04221) | $b$ | 2137.49353 | 1.78 |
| 5 | (2138.10178) | $b$ | (2137.42982) | $b$ |
| 6 | (2138.16203) | $b$ | 2137.36740 | 0.47 |
| 7 | 2138.22092 | -0.07 | (2137.30468) | $b$ |
| 8 | 2138.28061 | -0.34 | 2137.24164 | 0.44 |
| 9 | 2138.33951 | 0.22 | (2137.17864) | $b$ |
| 10 | 2138.39901 | 0.06 | 2137.11290 | -1.66 |
| 11 | 2138.45409 | -2.59 | 2137.05221 | 0.53 |
| 12 | 2138.51586 | -0.19 | 2136.98694 | -0.07 |
| 13 | 2138.57345 | 0.30 | 2136.92321 | -0.59 |
| 14 | 2138.63252 | 0.28 | 2136.85874 | 0.19 |
| 15 | 2138.68927 | 0.55 | 2136.79450 | -0.52 |
| 16 | 2138.74791 | 0.39 | 2136.72868 | -0.50 |
| 17 | 2138.80207 | -1.30 | 2136.66475 | -0.58 |
| 18 | (2138.86189) | $b$ | 2136.59915 | 0.25 |
| 19 | 2138.91608 | -1.03 | 2136.53213 | -2.59 |
| 20 | (2138.97535) | $b$ | 2136.46762 | -0.10 |
| 21 | 2139.03036 | 0.42 | 2136.40426 | 1.06 |
| 22 | (2139.08790) | $b$ | 2136.33626 | 0.64 |
| 23 | 2139.14198 | 0.12 | 2136.27033 | -0.45 |
| 24 | (2139.19954) | $b$ | 2136.20236 | -0.26 |
| 25 | 2139.25339 | 0.52 | 2136.13660 | -0.84 |
| 26 | (2139.31028) | $b$ | 2136.06950 | 0.79 |
| 27 | | | 2136.00302 | -0.16 |
| 28 | | | 2135.93331 | -0.58 |
| 29 | | | 2135.86773 | -0.29 |
| 30 | | | 2135.79732 | -0.84 |
| 31 | | | 2135.73273 | 0.79 |
| 32 | | | 2135.66131 | -0.21 |
| 33 | | | 2135.59627 | 1.31 |
| 34 | | | 2135.52481 | 0.84 |
| 35 | | | 2135.45795 | 0.89 |
| 36 | | | 2135.38635 | 0.84 |
| 37 | | | 2135.31755 | -0.70 |
| 38 | | | 2135.24602 | -0.12 |
| 39 | | | 2135.17773 | -0.80 |
| 40 | | | 2135.10510 | -0.77 |

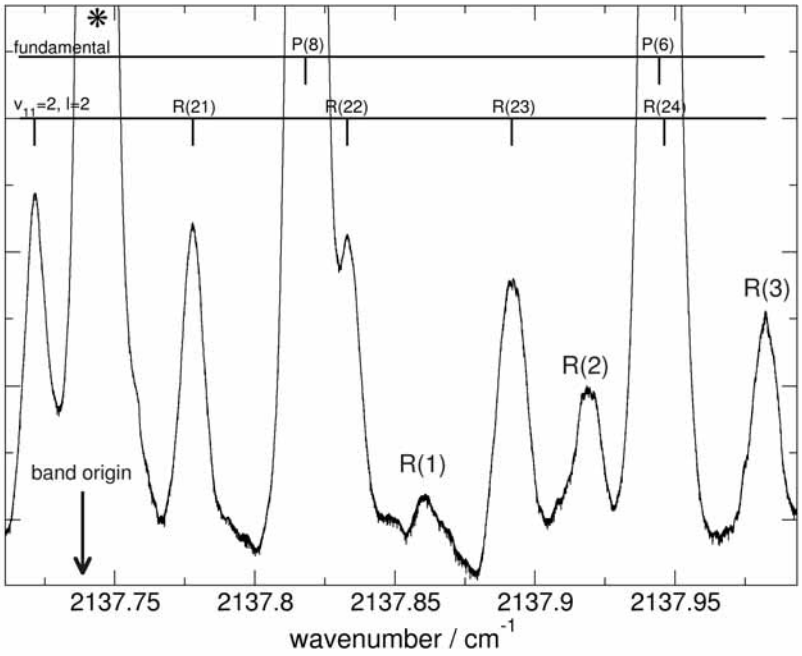


Figure 5.3: Part of the spectrum of $C_7$ showing the head of the *R*-branch of the $\nu_4 + \nu_{11} - \nu_{11}$ band: the observed spectrum indicates a typical pattern expected near the band origin.

Table 5.4: Molecular parameters in units of $cm^{-1}$ for the $\nu_4 + \nu_{11} - \nu_{11}$ hot band of $C_7$. *Ab initio* values for the rotational constants derived from values for $\alpha$ and $B_e$ calculated by Botschwina [9] using (2.9). The standard deviation of the fit was $0.702 \times 10^{-3}$. $D$ values proved to be not significant. Values derived by Heath *et al.* are given for comparison.

| Parameter | This work | Heath *et al.* [36] | *ab initio* |
|---|---|---|---|
| $\nu$ | 2137.73856(16) | 2136.0687(9) | |
| $B''$ | 0.0306759(38) | 0.033583(40) | 0.03072 |
| $q''$ [$\times$ $10^{-5}$] | 3.71(76) | | 2.68 |
| $B'$ | 0.0305622(41) | 0.033490(33) | 0.03061 |
| $q'$ [$\times$ $10^{-5}$] | 3.74(80) | | |
| $B''/B_0$ | 0.16 % | 9.3 % | 0.23 % |

part of the present data set as well, but though coinciding in position, the line assignments in both studies differ essentially. As a consequence, the rotational constants $B''$ deviate by almost 10 %, which will be discussed later.

### 5.3.2 The $\nu_4 + \nu_8 - \nu_8$, $\ell = 1$ hot band

A total of 49 lines lines were assigned to this band. It was identified as band arising from the second lowest bending mode $\nu_8$ following the argumentation above. Due to the $\pi_g$ symmetry of the $v_8 = 1$ level, the staggering expected for this band is opposite to the former one. Since the band origin could not be determined unambiguously, the absolute $J$-numbering was established following the approach used by Moazzen–Ahmadi *et al.* for the hot bands of $C_4$ and $C_5$ [62, 63].

Successive $J$-numberings led to an almost linear change in the rotational constant. Upon bending the chain, the rotational constant will increase compared to the vibrational ground state. With that in mind, the $J$-numbering was chosen to the effect that $B'' - B_0$ becomes minimal but positive.

Observed line positions and their residuals are given in Table 5.5. The fit was performed using equation 5.2 and led to the molecular constants listed in Table 5.6. The standard deviation of the fit was $0.768 \times 10^{-3}$. $D''$ and $D'$ proved to be not significant.

The spectra did not exhibit any features suited to be assigned as P(1) and R(0), which of course is no proof for the correct assignment but a strong support. Compared to the previously described hot band arising from the lowest bending mode, the rotational constant $B''$ is slightly smaller which corresponds to the trend in the $\alpha$-values calculated by Botschwina [9]. This may be regarded as another indication for the classification to be correct. $B''$ was obtained to be 0.0306697(36) $cm^{-1}$ which is roughly 0.14 % larger than $B_0$ and just 0.13 % smaller than the calculated value for $B_8$. The $B''$ value is in agreement with expectations since Moazzen–Ahmadi and co-workers obtained a change of approx. 0.4 % in the rotational constants for both $C_4$ and $C_5$ upon exciting the second lowest bending mode of each chain [64, 62]. Thus, judging from the $B''$ value, the final assignment appears to be quite reasonable.

The band origin is shifted by 0.56 $cm^{-1}$ compared to the fundamental. Thus, the $v_{11} = 1$ and $v_8 = 1$ hot bands have nearly the same band origin. A similar behaviour was observed for $C_4$ where the band shifts for the two hot bands are almost the same differing by just 0.035 $cm^{-1}$ [64]. In both cases, the hot band originating from the second lowest bending mode exhibits the smaller shift.

### 5.3.3 The $\nu_4 + 2\nu_{11} - 2\nu_{11}$, $\ell = 2$ hot band

The 57 observed lines given in Table 5.7 exhibit an almost constant $2\,B$ pattern, i.e. the staggering is, as mentioned before, only marginal compared to the two

Table 5.5: Observed frequencies for the $\nu_4 + \nu_8 - \nu_8$ hot band of $C_7$. Lines in parantheses are calculated values since they are blended with fundamental or unidentified transitions ($b$). Due to the $\pi_g$ symmetry of the $\nu_8$ bending, lines with even $J$ belong to the $e$-subband. All values given in $cm^{-1}$.

| J | *R(J)* | obs-calc ($\times 10^{-3}$) | *P(J)* | obs-calc ($\times 10^{-3}$) |
|---|---|---|---|---|
| 1 | (2137.87164) | $b$ | | |
| 2 | (2137.93215) | $b$ | (2137.62675) | $b$ |
| 3 | (2137.99273) | $b$ | (2137.56483) | $b$ |
| 4 | (2138.05266) | $b$ | 2137.50411 | 1.34 |
| 5 | 2138.11140 | -1.33 | (2137.44048) | $b$ |
| 6 | (2138.17223) | $b$ | 2137.37817 | 0.13 |
| 7 | 2138.23182 | -0.15 | (2137.31519) | $b$ |
| 8 | 2138.29112 | 0.37 | 2137.25306 | 0.69 |
| 9 | 2138.35025 | -0.03 | 2137.18901 | 0.23 |
| 10 | 2138.40960 | 1.13 | 2137.12490 | -0.87 |
| 11 | 2138.46711 | -0.55 | 2137.06205 | 0.42 |
| 12 | 2138.52556 | 0.31 | 2136.99916 | 0.93 |
| 13 | 2138.58426 | 0.15 | 2136.93370 | 0.15 |
| 14 | 2138.64156 | 0.46 | 2136.86803 | -1.73 |
| 15 | 2138.70088 | 1.25 | 2136.80521 | 0.67 |
| 16 | 2138.75606 | 0.04 | 2136.73968 | -0.68 |
| 17 | 2138.81371 | -0.50 | 2136.67350 | -1.10 |
| 18 | 2138.86972 | -0.28 | 2136.60873 | -1.28 |
| 19 | 2138.92734 | -0.53 | 2136.54253 | -1.20 |
| 20 | 2138.98205 | -1.00 | (2136.47870) | $b$ |
| 21 | 2139.04069 | 0.10 | 2136.41359 | 1.66 |
| 22 | (2139.09498) | $b$ | 2136.34711 | 0.58 |
| 23 | 2139.15180 | -0.59 | 2136.27910 | -0.10 |
| 24 | (2139.20609) | $b$ | 2136.21303 | -0.35 |
| 25 | 2139.26395 | 0.70 | 2136.14489 | -0.65 |
| 26 | (2139.31627) | $b$ | 2136.08011 | 0.81 |
| 27 | | | 2136.01199 | 1.04 |
| 28 | | | 2135.94402 | -0.26 |
| 29 | | | 2135.87438 | -1.05 |
| 30 | | | 2135.80837 | 0.04 |
| 31 | | | 2135.73900 | 0.03 |
| 32 | | | 2135.67064 | -0.81 |
| 33 | | | (2135.60163) | $b$ |
| 34 | | | 2135.53461 | 0.98 |
| 35 | | | 2135.46411 | 0.83 |
| 36 | | | (2135.39430) | $b$ |
| 37 | | | 2135.32441 | 0.38 |
| 38 | | | (2135.25453) | $b$ |
| 39 | | | 2135.18390 | 0.04 |
| 40 | | | (2135.11381) | $b$ |
| 41 | | | 2135.04231 | -0.44 |

Table 5.6: Molecular parameters in units of $cm^{-1}$ for the $\nu_4 + \nu_8 - \nu_8$ hot band of $C_7$. *Ab initio* values for the rotational constants derived from values for $\alpha$ and $B_e$ calculated by Botschwina [9] using (2.9). The standard deviation of the fit was $0.768 \times 10^{-3}$. $D$ values proved to be not significant.

| Parameter | This work | *ab initio* |
|---|---|---|
| $\nu$ | 2137.74932(18) | |
| $B''$ | 0.0306697(36) | 0.03071 |
| $q''$ [$\times 10^{-5}$] | 2.49(69) | 1.23 |
| $B'$ | 0.0305531(38) | 0.03060 |
| $q'$ [$\times 10^{-5}$] | 2.54(73) | |
| $B''/B_0$ | 0.14 % | 0.20 % |

cases portrayed before. Still the $J$-numbering could be fixed modulo two and the same proceeding described above was used to determine the correct assignment. However, in this case, the process was started by first performing fits similar to that of the fundamental mode separately for the $e$- and $f$-subbands each with $4\,B$ spacing without any staggering. With the chosen numbering, a fit of all transitions as hot band with ($v = 2$, $\ell = 2$) was performed and only the band origin $\nu$ and the rotational constants for lower and upper state, $B''$ and $B'$, were used in the final fit. The obtained parameters are given in Table 5.8. The standard deviation of the fit was $0.763 \times 10^{-3}$. Including centrifugal distortion constants yielded $D$ values of the order of $10^{-5}$ $cm^{-1}$ with uncertainties of more than 70 %. Because these values are far from being reasonable and, moreover, including them did not singificantly improve the fit, they were omitted from the fit. For comparison, molecular constants derived for the band assigned as $v_{11} = 2$, $\ell = 0$ by Heath *et al.* [36] are also given in table 5.8.

The lower state rotational constant was derived to be $B''$=0.0307988(37) $cm^{-1}$ which differs from the calculated value by less than 0.1 %. The shift of the band origin amounts 1.8 $cm^{-1}$ which is larger than expected. As can be taken from Table 5.9, the distance between the band origins of the fundamental and the hot bands arising from the $n^{\text{th}}$ bending level grows quite linearly with $n$ for $C_4$ and $C_5$ [22]. For $C_9$, the shift increases more than linearly [88], that is with a factor of roughly 2.6 instead of 2. Calculating the corresponding factor for $C_7$ one derives roughly 3.1.

## 5.4 Discussion

This analysis strongly supports the result derived by P. Botschwina stating that the $C_7$ chain is fairly rigid [9]. Neither a Coriolis interaction between the ground state and excited $\nu_{11}$ levels nor a large amplitude bending motion could be confirmed.

Table 5.7: Observed frequencies for the $\nu_4 + 2\nu_{11} - 2\nu_{11}$ hot band of $C_7$. Lines in parantheses are calculated values since they are blended with fundamental or unidentified transitions ($b$). All values given in $cm^{-1}$.

| J | *R(J)* | obs-calc ($\times 10^{-3}$) | *P(J)* | obs-calc ($\times 10^{-3}$) |
|---|---|---|---|---|
| 2 | 2136.66475 | -0.26 | | |
| 3 | 2136.72868 | 3.00 | 2136.29594 | -0.18 |
| 4 | (2136.78612) | $b$ | 2136.23401 | 0.18 |
| 5 | 2136.84663 | 0.30 | 2136.17063 | -0.67 |
| 6 | (2136.90631) | $b$ | (2136.10855) | $b$ |
| 7 | 2136.96578 | -0.27 | 2136.04505 | -0.51 |
| 8 | 2137.02675 | 1.19 | 2135.98217 | -0.17 |
| 9 | 2137.08402 | -0.82 | 2135.91820 | -0.69 |
| 10 | 2137.14456 | 0.67 | 2135.85479 | -0.42 |
| 11 | 2137.20365 | 0.94 | 2135.79084 | -0.45 |
| 12 | 2137.26211 | 0.81 | 2135.72727 | 0.12 |
| 13 | 2137.31938 | -0.27 | 2135.66131 | -1.46 |
| 14 | 2137.37817 | 0.39 | 2135.59966 | 1.50 |
| 15 | (2137.43567) | $b$ | 2135.53461 | 1.29 |
| 16 | 2137.49353 | 0.20 | 2135.46990 | 1.65 |
| 17 | 2137.55171 | 0.96 | (2135.40294) | $b$ |
| 18 | 2137.60842 | 0.47 | 2135.33852 | 1.11 |
| 19 | 2137.66565 | 0.73 | 2135.27184 | 0.20 |
| 20 | 2137.72142 | -0.23 | 2135.20606 | 0.42 |
| 21 | 2137.77788 | -0.27 | 2135.13941 | 0.00 |
| 22 | 2137.83304 | -1.38 | 2135.07278 | -0.17 |
| 23 | 2137.89173 | 1.27 | 2135.00581 | -0.45 |
| 24 | (2137.94627) | $b$ | 2134.93880 | -0.53 |
| 25 | 2138.00084 | -1.00 | | |
| 26 | (2138.05718) | $b$ | | |
| 27 | (2138.11230) | $b$ | | |
| 28 | 2138.16490 | -2.28 | | |
| 29 | 2138.22092 | -0.91 | | |
| 30 | 2138.27569 | -0.55 | | |
| 31 | 2138.32968 | -0.75 | | |
| 32 | 2138.38373 | -0.65 | | |
| 33 | 2138.43787 | 0.23 | | |
| 34 | (2138.49159) | $b$ | | |
| 35 | 2138.54529 | 0.44 | | |
| 36 | 2138.59747 | -0.41 | | |
| 37 | 2138.65101 | 0.34 | | |
| 38 | 2138.70088 | -2.36 | | |
| 39 | 2138.75606 | 0.49 | | |
| 40 | 2138.80728 | -0.39 | | |
| 41 | (2138.85954) | $b$ | | |
| 42 | 2138.91050 | -0.68 | | |
| 43 | (2138.96258) | $b$ | | |
| 44 | 2139.01527 | 1.51 | | |
| 45 | 2139.06502 | 0.44 | | |
| 46 | 2139.11568 | 0.27 | | |
| 47 | 2139.16596 | 0.07 | | |
| 48 | (2139.21614) | $b$ | | |
| 49 | (2139.26615) | $b$ | | |

Table 5.8: Molecular parameters in units of $cm^{-1}$ for the $\nu_4 + 2\nu_{11} - 2\nu_{11}$, $\ell = 2$ hot band of $C_7$. *Ab initio* values for the rotational constants derived from values for $\alpha$ and $B_e$ calculated by Botschwina [9] using (2.9). The standard deviation of the fit was $0.763 \times 10^{-3}$. Including centrifugal distortion constants did not significantly improve the quality of the fit. It was not possible to derive values for $q''$ and $q'$.

| Parameter | This work | Heath *et al.* ($\ell = 0$) [36] | *ab initio* |
|---|---|---|---|
| $\nu$ | 2136.48114(14) | 2133.8020(29) | |
| $B''$ | 0.0307988(37) | 0.03748(30) | 0.03078 |
| $B'$ | 0.0306830(35) | 0.03736(28) | 0.03073 |
| $B''/B_0$ | 0.56 % | 22.0 % | 0.42 % |

Table 5.9: Observed band shifts for hot bands with two quanta in the bend. The shifts for the hot bands arising from the first excited bending level are given for comparison. For $C_9$, only $\ell = 0$ was measured. In all cases, approximated values are given.

| molecule | hot band | Band shift [$cm^{-1}$] | Relative shift [% ] |
|---|---|---|---|
| $C_4$ | $\nu_3 + \nu_5 - \nu_5$ | 0.64 [22] | 0.04 |
| | $\nu_3 + 2\nu_5 - 2\nu_5$ | 1.30 [22] | 0.08 |
| $C_5$ | $\nu_3 + \nu_7 - \nu_7$ | 1.59 [22] | 0.07 |
| | $\nu_3 + 2\nu_7 - 2\nu_7$ | 3.21 [22] | 0.15 |
| $C_7$ | $\nu_4 + \nu_{11} - \nu_{11}$ | 0.58 | 0.027 |
| | $\nu_4 + 2\nu_{11} - 2\nu_{11}$ | 1.80 | 0.084 |
| $C_9$ | $\nu_6 + \nu_{15} - \nu_{15}$ | 0.10 [88] | 0.005 |
| | $\nu_6 + 2\nu_{15} - 2\nu_{15}$ | 0.26 [88] | 0.013 |

All derived constants discribing the fundamental and the hot bands are by no means unusual and lie well within the scope of expectations, except for the non-linear shift of the origin for the $\nu_4 + 2\nu_{11} - 2\nu_{11}$, $\ell = 2$ band. However, this shift is not large enough to evoke serious doubts concerning the assignment of the $\ell = 2$ band, especially considering the derived rotational constants.

As mentioned before, in none of the spectra any suitable features for the missing $\ell = 0$ band could be found. This could be caused by the following reasons: the corresponding levels are not occupied, the transition moment is too small, or lines of this band are not resolved for any reason. Concerning the occupation of the levels, there is no evidence for a reversed ordering of the $\ell = 0$ and $\ell = 2$ levels. A strange non-thermal occupation of energy levels in the jet may be excluded, too, due to the experiences with $C_9$ [88], where the ($v_{15} = 2$, $\ell = 0$) band was observed but $\ell = 2$ was not. However, for $C_4$ and $C_5$, Moazzen–Ahmadi *et al.* [22] were able to assign $\ell = 0$ as well as $\ell = 2$ transitions. Since their production method

using a hollow cathode discharge of acetylene differs from the present one, the situation may be not comparable. Further, there is no indication for a strange transition moment, as the $\ell = 0$ bands have been observed for the mentioned kin molecules. The most likely explanation for the missing band would be that the $\ell = 0$ transitions are blended by the strong fundamental ones occurring in almost the same 4 $B$ pattern. This could be possible if the band origin for the $\ell = 0$ band is by chance shifted by the right amount.

Heath *et al.* [36] assigned 9 lines to the *R*-branch of the $\nu_4 + 2\nu_{11} - 2\nu_{11}$, $\ell = 0$ band, which they identified via the required 4 $B$ spacing. They determined a band origin of 2133.8020(29) $cm^{-1}$ (see Table 5.8). Since their assignment of the first hot band arising from $v_{11} = 1$ must be doubted comparing the molecular constants given in Table 5.4, their results on the $\ell = 0$ band must be questioned, too. In fact, two of these 9 transitions also occured in spectra obtained in the course of this work, but they fit perfectly into the staggered 2 $B$ pattern of the ($v_{11} = 1$, $\ell = 1$) band. Due to the insufficient frequency coverage of the laser diodes below 2135 $cm^{-1}$, it was not possible to look for more of these questionable transitions.

It is beyond the scope of this work to judge why the prevelant interpretation of the hitherto existing experimental results led to crucially different results [36]. In principle, the line positions determined in both studies coincide within experimental errors. But in the present study significantly more hot band transitions could be observed which definitely simplified the analysis. Moreover, the hot band transition with the highest frequency measured by Heath *et al.* occurs below 2137 $cm^{-1}$, which is below the band origin for both the $\nu_4 + \nu_{11} - \nu_{11}$ and $\nu_4 + \nu_8 - \nu_8$ band determined in this work.

All in all, the presented assignments for the hot bands are the most likely in terms of reasonable molecular constants.

The derived $q$ values for the $\nu_4 + \nu_{11} - \nu_{11}$ and $\nu_4 + \nu_8 - \nu_8$ hot bands allow for the estimation of the band origins of the pure bendings by using the approximation (2.14). Assuming that the bonding character for $C_7$ is comparable to its kin molecules, $f_q$ was chosen to be 2.15(5)[13], since this value was already used for predictions for $C_5$ [62] and $C_9$ [88]. This assumption is justified given the new results concerning the rigidity of the $C_7$ chain. The band origins were derived to be $\nu_{11} = 54(11)$ $cm^{-1}$ and $\nu_8 = 81(23)$ $cm^{-1}$. Despite the rather large uncertainties, both results do not agree with the calculated values of 70 and 156 $cm^{-1}$ [9]. Of course, the calculated values heavily depend on a proper choice for $f_q$, which, in turn, requires accurate knowledge of the molecule itself. However, the more severe question concerns the quality of these predictions in terms of a laboratory or an astrophysical detection. The uncertainties for both band origins are presumably too large for selective laboratory measurements, because at present there is no source known allowing for a highly resolved 600 GHz scan around 1.6 THz to detect the lowest bending. Since the most significant contribution to the high uncertainties comes from the large inaccuracies of the $q$ values, the precision of the band origins may be improved by observing *P*-branch transitions with higher $J$ values to increase the accuracy for $q$.

[13] This value was derived from the analysis of $C_3S_2$ [43].

## 5.5 Summary

The presented results on the spectra of the $\nu_4$ fundamental and the associated hot bands give experimental evidence for the non-floppiness of $C_7$ and confirm theoretical predictions of a rather regular chain molecule, similar to the cases of $C_4$, $C_5$, and $C_9$. For the two energetically low-lying bending modes, $\nu_8$ and $\nu_{11}$, both rotational constants differ only by 0.2 %, from the ground state value, $B_0$=0.0306259(29) $cm^{-1}$, which is in very good agreement with the calculated values by P. Botschwina [9].

Furthermore, the present study marks the first investigation of the $\nu_4 + \nu_8 - \nu_8$, $\ell = 1$ band of $C_7$. Strictly speaking, it constitutes also the first reliable analysis of hot bands arising from the $\nu_{11}$ bending mode, stating that the hot band data of Heath *et al.* have been misassigned. In any case, experimental values for the band origins of the $\nu_8$ and $\nu_{11}$ fundamentals have been estimated for the first time.

# Appendix A

## Intensity Considerations

The following brief introduction into the field of absorption spectroscopy is guided predominantly by an article of L.A. Pugh and K. Narahari Rao [78] to illustrate the correlation between the number of absorbing molecules and the intensity of a resulting absorption line.

The absorption of radiation by a homogeneous gas sample is described by the Beer-Lambert law

$$I(\nu) = I_0 \cdot e^{-\kappa(\nu)\cdot x}. \tag{1}$$

Here, $I_0$ is the incident radiation intensity, $\kappa(\nu)$ accounts for the frequency dependent absorption coefficient and $x$ measures the number of absorbing molecules in the sightline. $I(\nu)$ is the intensity of a resulting absorption feature. The number $x$ can be expressed as

$$x = n \cdot l \tag{2}$$

where $n$ is the concentration of absorbing molecules in an area with length $l$ in the direction of propagation.

$\kappa(\nu)$ can be written as

$$\kappa(\nu) = S \cdot f(\nu - \nu_0). \tag{3}$$

The expression $f(\nu - \nu_0)$ represents the line shape, since absorption lines can have a Lorentzian or a Gaussian shape or a convolution of both shapes. $S$ denotes the line intensity or line strength. Usually, the line strength depends on the transition dipole moment, the temperature, and the partition function accounting for the occupation of energy levels. The dimension of $S$ is $\left[\frac{\text{cm}^{-1}}{\text{molecule}/\text{cm}^2}\right]$.

For the infrared transitions treated within the scope of this thesis, the line shape function can be presumed as a Doppler profile (Gaussian) due to the rather low pressures in the vacuum chamber

$$f(\nu - \nu_0) = \frac{1}{\Delta\nu_D}\sqrt{\frac{\ln 2}{\pi}} \cdot e^{-(\ln 2)\left(\frac{\nu-\nu_0}{\Delta\nu_D}\right)^2}. \tag{4}$$

In this representation, $\Delta\nu_D$ denotes the Doppler half-width, in particular, the half width at half maximum (HWHM), which can be calculated according to

$$\Delta\nu_D = 3.581 \cdot 10^{-7} \cdot \nu_0 \cdot \sqrt{\frac{T}{M}} \tag{5}$$

where $T$ is the gas temperature (in K), and $M$ the molecular weight (in amu).

At the center frequency $\nu_0$, equation 4 simplfies to

$$f(0) = \frac{1}{\Delta\nu_D}\sqrt{\frac{\ln 2}{\pi}}. \tag{6}$$

Thus, the absorption coefficient for $\nu_0$ becomes

$$\kappa(\nu_0) = S \cdot \frac{1}{\Delta\nu_D}\sqrt{\frac{\ln 2}{\pi}}. \tag{7}$$

For a certain transition occuring at the frequency $\nu_0$, the number of absorbing molecules per unit area along the direction of propagation $n$ is correlated to the transition's intensity $I(\nu_0)$ by

$$I(\nu_0) = I_0 \cdot e^{-S\cdot\frac{1}{\Delta\nu_D}\sqrt{\frac{\ln 2}{\pi}}\cdot n\cdot l}. \tag{8}$$

Resolving this equation for $n$ yields

$$n = -\frac{\ln\left(\frac{I(\nu_0)}{I_0}\right) \cdot \Delta\nu_D}{S \cdot \sqrt{\frac{\ln 2}{\pi}} \cdot l}. \tag{9}$$

This formula is valid for an absorption path of length $l$, which means $n_{min}$ is the minimum number of molecules for an experiment using an absorption cell of length $l$. However, in case of a multipass absorption, the very same molecules can be used for detection during each pass. Thus, the value $n$ calculated with equation (9) has to be divided by the number of passes $n_p$ to derive the minimum number of molecules for a multipass experiment.

All in all, one gets:

$$n = -\frac{\ln\left(\frac{I(\nu_0)}{I_0}\right) \cdot \Delta\nu_D}{S \cdot \sqrt{\frac{\ln 2}{\pi}} \cdot l \cdot n_p} \tag{10}$$

# Bibliography


[1] M. Algranati, H. Feldman, D. Kella, E. Malkin, E. Miklazky, R. Naaman, Z. Vager, J. Zajfman. The structure of $C_4$ as studied by the Coulomb explosion method. *J. Chem. Phys.* 90(8), 4617–4618, 1989

[2] D.W. Arnold, S.E. Bradforth, T.N. Kitsopoulos, D.M. Neumark. Vibrationally resolved spectra of $C_2$-$C_{11}$ by anion photoelectron spectroscopy. *J. Chem. Phys.* 95(12), 8753–8764, 1991

[3] P.S. Bechtold, M. Neeb. *B4: Struktur und elektronische Eigenschaften von Clustern*. Skript, Institut für Festkörperforschung Forschungszentrum Jülich GmbH, 1997 RWTH Aachen, 1994

[4] P.F. Bernath, K.W. Hinkle, J.J. Keady. Detection of $C_5$ in the Circumstellar Shell of IRC+10216. *Science* 244, 562–564, 1989

[5] P.F. Bernath. *Spectra of Atoms and Molecules*. Oxford University Press, 1995

[6] U. Berndt. *Infrarot-Spektroskopie an kleinen Kohlenstoff-Clustern*. Cuvellier Verlag Göttingen, PhD Thesis, Köln, 2000

[7] R.P.A. Bettens, E. Herbst. The abundance of very large hydrocarbons and carbon clusters in the diffuse interstellar medium. *Astrophys. J.* 468, 686–693, 1996

[8] P. Botschwina. The equilibrium structures of linear carbon clusters of type $C_{2n+1}$ (n=1-4). *Theor. Chem. Acc.* 104, 160–162, 2000

[9] P. Botschwina. A coupled cluster study of $C_7$: no evidence of floppiness. *Chem. Phys. Lett.* 354, 148–155, 2002

[10] P. Botschwina. Accurate equilibrium structures for small polyatomic molecules, radicals and carbenes. *Molecular Physics* 103(10), 1441–1460, 2005

[11] P. Botschwina. The equilibrium structures of linear carbon clusters of type $C_{2n+1}$ (n=1-4). *Theor. Chem. Acc.* 114, 360–162, 2005

[12] P. Botschwina, R. Oswald. On the vibrations of linear $C_{11}$: A coupled cluster study. *Chem. Phys.* 325, 485–491, 2006

[13] J. Cernicharo, J.R. Goicoechea, E. Caux. Far-infrared detection of $C_3$ in Sagittarius B2 and IRC+10216. *Astrophys. J.*, 534, L199–L202, 2000

[14] J. Cernicharo, J.R. Goicoechea, Y. Benilan. A new infrared band in interstellar and circumstellar clouds: $C_4$ or $C_4H$? *Astrophys. J.* 580, L157–L160, 2002

[15] The Cologne database for molecular spectroscopy, CDMS. http://www.cdms.de

[16] D. Crampton, A.P. Cowley, R.M. Humphreys. Spectroscopic observations of CRL 2688. *Astrophys. J.* 198, L135–L137, 1975

[17] A.E. Douglas. Origin of the diffuse interstellar lines. *Nature* Vol. 269, 130–132, 1977

[18] Q. Fan, G.V. Pfeiffer. Theoretical study of linear $C_n$ (n=6-10) and $HC_nH$ (n=2-10) Molecules. *Chemical Physics Letters* 162, 472–478, 1989

[19] P. Freivogel, M. Grutter,D. Forney, and J.P. Maier. Infrared bands of mass-selected carbon chains $C_n$ (n=8-12) and $C_n^-$ (n=5-10,12) in neon matrices. *Chem. Phys.* 216, 401–406, 1997

[20] G.W. Fuchs. *Charakterisierung einer Kohlenstoff-Cluster-Quelle*. Diplomarbeit, Köln, 1999

[21] G.W. Fuchs. *Carbon Chain Molecules - Production and Spectroscopic Detection*. Cuvellier Verlag Göttingen, PhD Thesis, Köln, 2003

[22] S. Gakwaya, Z. Abusara, N. Moazzen–Ahmadi. Vibrational hot bands of linear $C_4$ and $C_5$ arising from a bending vibration with two quanta in the lowest bend: the $\nu_3 + 2\,\nu_5 - 2\,\nu_5$ band $C_4$ and the $\nu_3 + 2\,\nu_7 - 2\,\nu_7$ band of $C_5$. *Chem. Phys. Lett.* 398, 564–571, 2004

[23] G.A. Galazutdinov, A. Petelewski, F.A. Musaev, C. Moutou, G. Lo Curto, J. Krelowski. The interstellar $C_3$ chain molecule in different interstellar environments. *Astron. Astrophys.* 395, 969–974, 2002

[24] T.F. Giesen. *Druckverschiebung und -verbreiterung an $H_2O$-Infrarot-Übergängen*. PhD Thesis, Köln, 1992

[25] T.F. Giesen, A. Van Orden, H.J. Hwang, R.S. Fellers, R.A. Provencal, R.J. Saykally. Infrared Laser Spectroscopy of the Linear $C_{13}$ Carbon Cluster. *Science* 265, 756–759, 1994

[26] T.F. Giesen, U. Berndt, K.M.T. Yamada, G. Fuchs, R. Schieder, G. Winnewisser, R.A. Provencal, F.N. Keutsch, A. Van Orden, R.J. Saykally. Detection of the Linear Carbon Cluster $C_{10}$: Rotationally Resolved Diode-Laser Spectroscopy. *ChemPhysChem* No. 4, 242–247, 2001

[27] T.F. Giesen, A.O. Van Orden, J.D. Cruzan, R.A. Provencal, R.J. Saykally, R. Gendriesch, F. Lewen, G. Winnewisser. Interstellar detection of CCC and high-precision laboratory measurements near 2 THz. *Astrophys. J.* 551, L181–L184, 2001

[28] J.R. Goicoechea, J. Cernicharo, H. Masso, M.L. Senent. A new unidentified far-infrared band in NGC 7027. *Astrophys. J.* 609, 225–230, 2004

[29] W. Gordy, R.L. Cook. *Microwave Molecular Spectra*. John Wiley and Sons Inc., 1984

[30] N.G. Gotts, G. von Helden, M.T. Bowers. Carbon cluster anions: structure and growth from $C_5^-$ to $C_{62}^-$. *Intern. Journal of Mass Spectrometry and Ion Processes* 149/150, 217–229, 1995

[31] W.R.M. Graham, K.I. Dismuke, W. Weltner Jr. The $C_4$ molecule. *Astrophys. J.* 204, 301–310, 1976

[32] G. Guelachvili, M. Birk, Ch.J. Bordé, L.R. Brown, B. Carli, A.R.H. Cole, K.M. Evenson, A. Fayt, D. Hausamann *et al.*. High resolution wavenumber standards for the infrared. *J. Mol. Spec.* 177(1), 164–179, 1996

[33] H. Handschuh, G. Ganteför, B. Kessler, P.S. Bechthold, W. Eberhardt. Stable Configurations of Carbon Clusters: Chains, Rings, and Fullerenes. *Phys. Rev. Lett.* 74(7), 1095–1098, 1990

[34] J.R. Heath, R.J. Saykally. The structure of the $C_4$ cluster radical. *J. Chem. Phys.* 94(4), 3271–3273, 1991

[35] J.R. Heath, R.A. Sheeks, A.L. Cooksy, R.J. Saykally. The $C_7$ cluster: structure and infrared frequencies. *Science* 249, 895–897, 1990

[36] J.R. Heath, R.J. Saykally. Infrared laser absorption spectroscopy of the $\nu_4(\sigma_u)$ fundamental and associated $\nu_{11}(\pi_u)$ hot band of $C_7$: Evidence for alternating rigidity in linear carbon clusters. *J. Chem. Phys.* 94 (3), 1724–1729, 1991

[37] J.R. Heath, A. Van Orden, E. Kuo, R.J. Saykally. The $\nu_5$ band of $C_7$. *Chem. Phys. Lett.* 182 (1), 17–20, 1991

[38] O. Heber, D. Kella, D. Zajfman, H. Feldman, D. Majer, Z. Vager, R. Naaman. Carbon cluster imaging at the Weizmann Institute Coulomb explosion system. *Nuclear Instruments and Methods in Physics Research* B79, 227–229, 1993

[39] D. Herriott, H. Kogelnik, R. Kompfner. Off-axis paths in spherical mirror interferometers. *Applied Optics* 3, 523–526, 1964

[40] G. Herzberg. *Molecular Spectra and Molecular Structure*. Volumes I-III, Van Nostrand Reinhold Company Inc., 1945

[41] G. Herziger. *Lasertechnik*. Lecture notes, RWTH Aachen, 1994

[42] K.W. Hinkle, J.J. Keady, P.F. Bernath. Detection of $C_3$ in the Circumstellar Shell of IRC+10216. *Science* 241, 1319–1322, 1988

[43] F. Holland, M. Winnewisser, C. Jarman, H.W. Kroto. The $\nu_3$ Band System of SCCCS: High-Resolution Fourier Transform and Diode Laser Measurements. *J. Mol. Spec.* 130, 344–370, 1988

[44] J. Hutter, H. P. Lüthi, F. Diederich. Structure and Vibrational Frequencies of the Carbon Molecules $C_2$-$C_{18}$ Calculated by Density Functional Theory. *J. Am. Chem. Soc.* 116, 750–756, 1994

[45] J. Hutter, H.P. Lüthi. The molecular structure of $C_6$: A theoretical investigation. *J. Chem. Phys.* 101(3), 2213–2216, 1994

[46] H.J. Hwang, A. Van Orden, K. Tanaka. E.W. Kuo, J.R. Heath, R.J. Saykally. Infrared laser spectroscopy of jet-cooled carbon clusters: Structure of triplet $C_6$. *Molecular Physics* 79 (4), 769–776, 1993

[47] see data sheet concerning J10D series InSb detectors by Judson Technologies on www.lasercomponents.com

[48] P. Jensen, C. McMichael Rohlfing, J. Almlöf. Calculation of the complete-active-space self-consistent-fiel potential-energy surface, the dipole moment surfaces, the rotation-vibration energies, and the vibrational transition moments for $C_3$ $\tilde{X}\ ^1\Sigma_g^+$. *J. Chem. Phys.* 97 (5), 3399–3411, 1992

[49] R.O. Jones. Density functional study of carbon clusters $C_{2n}$ ($2 \leq n \leq 16$). I. Structure and bonding in the neutral clusters. *J. Chem. Phys.* 110 (11), 5189–5199, 1998

[50] R.I. Kaiser. Experimental Investigation on the Formation of Carbon-Bearing Molecules in the Interstellar Medium via Neutral-Neutral Reactions. *Chem. Rev.* 102, 1309–1358, 2002

[51] K. Kawaguchi, K. Matsumura, H. Kanamori, E. Hirota. Diode laser spectroscopy of $C_3$: The $\nu_2 + \nu_3 - \nu_2$, $2\,\nu_2 + \nu_3 - 2\,\nu_2$, and $2\,\nu_2 + \nu_3$ bands. *J. Chem. Phys.* 91 (4), 1953–1957, 1989

[52] D. Kella, D. Zajfman, O. Heber, D. Majer, H. Feldman, Z. Vager, R. Naaman. Observation of Laser Excitation of Rhombic $C_4$ using the Coulomb Explosion Method. *Z. Phys. D* 26, 340–342, 1993

[53] W.H. Kohl. *Handbook of Materials and Techniques for Vacuum Devices*. Reinhold Publisher, New York, 1967

[54] H.W. Kroto, J.R. Heath, S.C. O'Brien, R.F. Curl, and R.E. Smalley. $C_{60}$: Buckminsterfullerene. *Nature* 318, 162–163, 1985

[55] see data sheets concerning SPECDILAS IR-XXXX on www.lasercomponents.com

[56] C. Liang and H.F. Schaefer III. *Chem. Phys. Lett.* 169, 150–160, 1990

[57] H. Linnartz, O. Vaizert, T. Motylewski, and J.P. Maier. The $^3\Sigma_u^- \leftarrow X^3\Sigma_g^-$ electronic spectrum of linear $C_4$ in the gas phase. *J. Chem. Phys.* 112, 9777–9779, 2000

[58] J.P. Maier, N.M. Lakin, G.A.H. Walker, D.A. Bohlenender. Detection of $C_3$ in interstellar clouds. *Astrophys. J.* 553, 267–273, 2001

[59] J.M.L. Martin, P.R. Taylor. Structure and Vibrations of Small Carbon Clusters from Coupled-Cluster Calculations. *J. Phys. Chem.* 100, 6047–6056, 1996

[60] K. Matsumura, H. Kanamori, K. Kawaguchi, E. Hirota. Infrared diode laser kinetic spectroscopy of the $\nu_3$ band of $C_3$. *J. Chem. Phys.* 89 (6), 3491–3494, 1988

[61] M.C. McCarthy, A.J. Apponi, C.A. Gottlieb, P. Thaddeus. Laboratory detection of five new linear silicon carbides: $SiC_3$, $SiC_5$, $SiC_6$, $SiC_7$, and $SiC_8$. *Astrophys. J.* 538, 766–772, 2000

[62] N. Moazzen-Ahmadi, J.J. Thong, A.R.W. McKellar. Diode laser spectroscopy of gas phase $C_5$: The $\nu_3$ fundamental and associated hot bands. *J. Chem. Phys.* 91 (4), 2140–2147, 1989

[63] N. Moazzen-Ahmadi, J.J. Thong, A.R.W. McKellar. Infrared diode laser spectroscopy of the $\nu_3$ fundamental and $\nu_3 + \nu_5 - \nu_5$ sequence bands of the $C_4$ radical in a hollow cathode discharge. *J. Chem. Phys.* 100 (6), 4033–4038, 1994

[64] N. Moazzen-Ahmadi, J.J. Thong. Infrared diode laser spectroscopy of $C_4$. The $\nu_3 + \nu_4 - \nu_4$ sequence band. *Chem. Phys. Lett.* 233, 471–476, 1995

[65] G. Monninger. PhD Thesis, University of Heidelberg, 1995

[66] T. Motylewski, O. Vaizert, T.F. Giesen, H. Linnartz, and J.P. Maier. The $^1\Pi_u \leftarrow X^1\Sigma_g^+$ electronic spectrum of linear $C_5$ in the gas phase. *J. Chem. Phys.* 111, 6161–6163, 1999

[67] P. Neubauer-Guenther, T.F. Giesen, U. Berndt, G. Fuchs, G. Winnewisser. The Cologne Carbon Cluster Experiment: ro-vibrational spectroscopy on $C_8$ and other small carbon clusters. *Spectrochim. Acta Part A* 59, 431–441, 2003

[68] F.J. Northrup, T. Sears, E. Rohlfing. A Semirigid Bender Analysis of an Extensive Set of Rotation-Vibration-Levels in $\tilde{X}\ ^1\Sigma_g^+$ $C_3$. *J. Mol. Spec.* 145, 74–88, 1991

[69] Y. Ohshima, Y. Endo, T. Ogata. Fourier transform microwave spectroscopy of triplet carbon monoxides, $C_2O$, $C_4O$, $C_6O$, and $C_8O$. *J. Chem. Phys.* 102(4), 1493–1500, 1995

[70] B.A. Paldus, R.N. Zare. Absorption Spectroscopies: From Early Beginnigs to Cavity-Ringdown Spectroscopy. In *Cavity Ringdown Spectroscopy*, ACS Symposium Series 720, 49–70, 1999

[71] D. Papoušek, M.R. Aliev. *Molecular vibrational/rotational spectra*. Czechoslovak Academy of Science, Academia/Prague, 1982

[72] V. Parasuk, J. Almlöf. The electronic and molecular structure of $C_6$: Complete active space self-consistent-field and multireference configuration interaction. *J. Chem. Phys.* 91(2), 1137–1141, 1989

[73] H.M. Pickett. The Fitting and Prediction of Vibration-Rotation Spectra with Spin Interactions. *J. Mol. Spec.* 148, 371–377 (1991)

[74] H.O. Pierson. *Handbook of Carbon, Graphite, Diamond and Fullerenes*. Ed: H.O. Pierson, Noyes Publications, Park Ridge, New Jersey, U.S.A., 1993

[75] K.S. Pitzer, E. Clementi. Large Molecules in Carbon Vapor. *J. Am. Chem. Soc.* 81, 4477–4485, 1959

[76] V. Pless, H.U. Suter, B. Engels. *Ab initio* study of the energy difference between the cyclic and linear forms of the $C_6$ molecule. *J. Chem. Phys.* 101 (5), 4042–4048, 1994

[77] J.D. Presilla-Marquez, J.A. Sheehy, J.D. Mills, P.G. Carrick, C.W. Larson. Vibrational spectra of cyclic $C_6$ in solid argon. *Chem. Phys. Lett.* 274, 439–444, 1997

[78] L.A. Pugh, K. Narahari Rao. Intensities from Infrared Spectra. In *Molecular Spectroscopy: Modern Research* Vol. II, Academic Press Inc., 165–227, 1976

[79] K. Raghavachari, J.S. Binkley. Structure, stability, and fragmentation of small carbon clusters. *J. Chem. Phys.* 87(4), 2191–2197, 1987

[80] E.A. Rohlfing, D.M. Cox, A. Kaldor. Production and characterization of supersonic carbon cluster beams. *J. Chem. Phys.* 81(7), 3322–3330, 1984

[81] E. Roueff, P. Felenbok, J.H. Black, C. Gry. Interstellar $C_3$ toward HD 210121. *A&A* 384, 629–637, 2002

[82] C.A. Schmuttenmaer, R.C. Cohen, N. Pugliano, J.R. Heath, A.L. Cooksy, K.L. Busarow, R.J. Saykally. Tunable Far-IR Laser Spectroscopy of Jet-Cooled Carbon Clusters: The $\nu_2$ Bending Vibration of $C_3$. *Science* 249, 897–899, 1990

[83] D. Strelnikov, R. Reusch, W. Krätschmer. Assignment of Carbon Chain Molecules in Cryogenic Matrices by Selective Laser-Induced Oxidation. *J. Phys. Chem. A* 109, 7708–7713, 2005

[84] P. Swings, A. McKellar, K.N. Rao. Spectra of the late N-type stars in the ultra-violet, violet and blue-green regions. *Mon. Not. R. Astr. Soc.* 113, 571–581, 1953

[85] J.B. Tatum, J.K.G. Watson. Rotational Line Strengths in $^3\Sigma^{\pm}$-$^3\Sigma_g^{\pm}$ Transitions with Intermediate Coupling. *Can. J. Phys.* 49, 2693–2703, 1971

[86] Z. Vager, H. Feldman, D. Kella, E. Malkin, E. Miklazky, J. Zajfman, R. Naaman. The structure of small carbon clusters. *Z. Phys. D* 19, 413–418, 1991

[87] M. Vala, T.M. Chandrasekhar, J. Szczepanski, R. Pillow. Structure and Infrared Spectroscopy of the $C_6$ and $C_8$ Carbon Clusters. *High Temp. Sci.* 27, 19–30, 1990

[88] A. Van Orden, H.J. Hwang, E.W. Kuo, R.J. Saykally. Infrared laser spectroscopy of jet-cooled carbon clusters: The bending dynamics of linear $C_9$. *J. Chem. Phys.* 98 (9), 6678–6683, 1993

[89] A. Van Orden, R.A. Provencal, F.N. Keutsch, R.J. Saykally. Infrared laser spectroscopy of jet-cooled carbon clusters: The $\nu_5$ band of linear $C_9$. *J. Chem. Phys.* 105 (15), 6111–6116, 1996

[90] A. Van Orden. *Direct Infrared Laser Absorption Spectroscopy of Jet-Cooled Carbon and Silicon-Carbon Clusters*. PhD Thesis, Berkeley, 1996

[91] A. Van Orden and R.J. Saykally. Small Carbon Clusters: Spectroscopy, Structure, and Energetics. *Chem. Rev.* 98, 2313–2357, 1998

[92] R.J. Van Zee, R.F. Ferrante, K.J. Zeringue, W. Weltner. ESR of the $C_6$ molecule. *J. Chem. Phys.* 86(9), 5212–5213, 1987

[93] R.J. Van Zee, R.F. Ferrante, K.J. Zeringue, W. Weltner, D.W. Ewing. Electron spin resonance of the $C_6$, $C_8$, and $C_{10}$ molecules. *J. Chem. Phys.* 88(6), 3465–3474, 1988

[94] G. von Helden, M.T. Hsu, N.G. Gotts, P.R. Kemper, M.T. Bowers. Do small fullerenes exist only on the computer? Experimental results on $C_{20}^{\pm}$ and $C_{24}^{\pm}$ *Chem. Phys. Lett.* 204, 15–22, 1993

[95] S.L. Wang, C.M.L. Rittby, W.R.M. Graham. Detection of cyclic carbon clusters. I. Isotopic study of the $\nu_4(e')$ mode of cyclic $C_6$ in solid Ar. *J. Chem. Phys.* 107(16), 6032–6037, 1997

[96] S.L. Wang, C.M.L. Rittby, W.R.M. Graham. Detection of cyclic carbon clusters. II. Isotopic study of the $\nu_{12}(e_u)$ mode of cyclic $C_8$ in solid Ar. *J. Chem. Phys.* 107(18), 7025–7033, 1997

[97] J.D. Watts, J. Gauss, J.F. Stanton, R.J. Bartlett. Linear and cyclic isomers of $C_4$. A theoretical study with coupled-cluster methods and large basis sets. *J. Chem. Phys.* 97(11), 8372–8381, 1992

[98] W. Weltner Jr., R.J. Van Zee. Carbon Molecules, Ions, and Clusters. *Chem. Rev.* 89, 1713–1747, 1989

[99] C. Xu, G.R. Burton, T.R. Taylor, D.M. Neumark. Photoelectron spectroscopy of $C_4^-$, $C_6^-$, and $C_8^-$. *J. Chem. Phys.* 107(9), 3428–3436, 1997

[100] K.M.T. Yamada, F.W. Birss, M.R. Aliev. Effective Hamiltonian for polyatomic linear molecules. *J. Mol. Spec.* 112, 347–356, 1985

[101] K.M.T. Yamada, private communication

[102] S. Yang, K.J. Taylor, M.J. Craycraft, J. Conceicao, C.L. Pettiette, O. Cheshnovsky, R.E. Smalley. UPS of 2-30-atom carbon clusters: chains and rings. *Chem. Phys. Lett.* 144, 431–436, 1988

[103] D. Zajfman, H. Feldman, O. Heber, D. Kella, D. Majer, Z. Vager, R. Naaman. Electron Photodetachment Cross Sections of Small Carbon Clusters: Evidence for Nonlininear Isomers. *Science* 258, 1129–1131, 1992

[104] D. Zajfman, D. Kella, O. Heber, D. Majer, H. Feldman, Z. Vager, R. Naaman. The Isomers of Small Carbon Clusters. *Z. Phys. D* 26, 343–345, 1993

# Danksagung

An dieser Stelle möchte ich all jenen danken, die mich im Verlauf dieser Arbeit unterstützt und dadurch zu ihrem Gelingen beigetragen haben.

Mein Dank gilt vor allem Herrn Priv. Doz. Dr. Thomas Giesen für die Betreuung dieser Arbeit. Die vielen fachlichen und die nicht gar so fachlichen Diskussionen, seine genialen Einfälle sowie sein Vertrauen in meine Arbeit waren und sind für mich von großem Wert. Das “Giesen’sche Timing” hat sich während dieser Arbeit vielfach bewährt.

Bei Herrn Prof. Jan Jolie möchte ich mich für die Übernahme des Zweitgutachtens bedanken. Herrn Prof. Dr. Axel Klein danke ich für seine Bereitschaft, den Vorsitz der Disputationsprüfung zu führen.

Herrn Dr. Koichi Yamada sei herzlich für die Einweisung in LINX und die fruchtbaren Diskussionen über mögliche Zuordnungen gedankt.

Herrn Prof. Dr. Gisbert Winnewisser möchte ich für sein Interesse an meiner Arbeit und sein Engagement für die Kölner Spektroskopiegruppe danken.

Bei Herrn Dr. Frank Lewen möchte ich mich für seine Unterstützung in allen Fragen der Technik und seinen unerschütterlichen Enthusiasmus bedanken. Herrn Prof. Dr. Stephan Schlemmer danke ich für die vielen wertvollen Diskussionen und sein Bestreben, das “Briefing” wieder zu einem solchen zu machen.

Herrn Dr. Holger Müller danke ich vielmals für seine Hilfe im Umgang mit dem Pickett-Programm sowie seine Beharrlichkeit in Sachen “Grundzustandskombinationsdifferenzen”.

Frau Dr. Sandra Brünken und Herrn Dr. Michael Caris danke ich für die schöne gemeinsame Promotionszeit. Bei Sandra möchte ich mich besonders für die Nachtschichten im Labor, die damit verbundene Frage nach dem Abendessen sowie die unzähligen Gespräche über alles und jeden bedanken.

Michael gebührt mein Dank für seine Unterstützung in Labor 320, die gemeinsame Dijon-Erfahrung und nicht zuletzt für den regen Austausch von Dellbrücker Neuigkeiten.

Ein großes Dankeschön geht an Dr. Ute Berndt für die Einweisung in das Spektrometer sowie Dr. Guido Fuchs für die Programmierung und die Hilfe beim Quellendesign. Herrn Jürgen Krieg danke ich für seine Unterstützung gerade in den letzten Monaten meiner Promotion.

Dem Team der Mechanikwerkstatt gilt mein besonderer Dank für die sorgfältige und prompte Anfertigung aller Bauteile. Danke für die Geduld, auch bei der x-ten Iteration der Cluster-Quelle (aka “Bumerang”) noch Verständnis für Änderungswünsche zu haben. Danke auch an Frank Bielau für seine schnelle Hilfe bei elektronischen Problemen.

Der ehemaligen und aktuellen Besatzung von Zimmer 316, vor allem Michael Caris, Doris Herberth und Gundolf Wieching, danke ich für die schöne Zeit und den Humor, der mir über so manches Problem experimenteller oder privater Natur hinweggeholfen hat.

Vielen Dank der gesamten Spektroskopiegruppe für das produktive und freundschaftliche Arbeitsklima, insbesondere Oliver Baum für den Nachschub an Scheibenwelt-Lektüre, Christian Endres für den Linux-Support und Monika Koerber für den Austausch von Soprani-Ansichten.
Nicht vergessen: *“Time is an illusion. Lunchtime doubly so.”* (Douglas Adams)

Ein herzliches Dankeschön an Oliver Baum, Sandra Brünken, Michael Caris, Thomas Giesen, Astrid Imig, Frank Lewen, Holger Müller, David Rabanus, Stephan Schlemmer und Kate Siegle für das Korrekturlesen von Teilen dieser Arbeit.

Meiner Familie, besonders René, kann ich gar nicht genug danken für die jahrelange Unterstützung und den Rückhalt, ohne den diese Arbeit niemals möglich gewesen wäre.

Mum, danke für alles!

# Erklärung

Ich versichere, dass ich die von mir vorgelegte Dissertation selbstständig angefertigt, die benutzten Quellen und Hilfsmittel vollständig angegeben und die Stellen der Arbeit - einschließlich Tabellen, Karten und Abbildungen-, die anderen Werken im Wortlaut oder dem Sinn nach entnommen sind, in jedem Einzelfall als Entlehnung kenntlich gemacht habe; dass diese Dissertation noch keiner anderen Fakultät oder Universität zur Prüfung vorgelegen hat; dass sie - abgesehen von unten angegebenen Teilpublikationen - noch nicht veröffentlicht worden ist sowie, dass ich eine solche Veröffentlichung vor Abschluss des Promotionsverfahrens nicht vornehmen werde.

Die Bestimmungen der Promotionsordnung sind mir bekannt. Die von mir vorgelegte Dissertation ist von Herrn Privatdozent Dr. T.F. Giesen betreut worden.

## Teilpublikationen

- "The Cologne Carbon Cluster Experiment: rovibrational spectroscopy on $C_8$ and other small carbon clusters", P. Neubauer-Guenther, T.F. Giesen, U. Berndt, G. Fuchs, G. Winnewisser, *Spectrochimica Acta Part A* 59, 431–441, 2003
- "Terahertz Rotational Spectroscopy", T.F. Giesen, S. Brünken, M. Caris, P. Neubauer-Guenther, U. Fuchs, G.W. Fuchs, F. Lewen, *Proceedings of the International Astronomical Union*, 87–96, 2005
- "Analysis of the $\nu_4$ stretching mode and associated hot bands of $C_7$: Experimental evidence for a non-floppy molecule", P. Neubauer-Guenther, T.F. Giesen, J. Krieg, S. Schlemmer, K.M.T. Yamada, submitted to JCP, 2006
- "Linear $C_8$ – A Case of Spin Uncoupling", P. Neubauer-Guenther, K.M.T. Yamada, T.F. Giesen, in prep.

# Lebenslauf

| | |
|---|---|
| Name: | Petra Neubauer-Guenther (geb. Neubauer) |
| Geburtsdatum: | 26. Juli 1974 |
| Geburtsort: | Köln |
| Saatsangehörigkeit: | deutsch |
| Familienstand: | verheiratet |

## Schulausbildung

| | |
|---|---|
| 1981–1985 | Katholische Grundschule Köln-Dellbrück |
| 1985–1994 | Dietrich-Bonhoeffer-Gymnasium in Bergisch Gladbach |
| 1994 | Abitur |

## Hochschulstudium

| | |
|---|---|
| 10/1994–02/1997 | Grundstudium der Physik an der Universität zu Köln |
| 02/1997 | Vordiplom in Physik |
| 02/1997–07/1999 | Hauptstudium der Physik |
| 07/1999–09/2000 | Diplomarbeit am I. Physikalischen Institut |
| 09/2000 | Diplom in Physik |
| 10/2000 | Beginn des Promotionsstudiums |

## Beschäftigung

| | |
|---|---|
| 07/1999–09/2000 | Studentische Hilfskraft am I. Physikalischen Institut |
| 10/2000–12/2001 | Wissenschaftliche Hilfskraft |
| seit 01/2002 | Wissenschaftliche Mitarbeiterin |